

## Thermoplastic polymers for neural implantable interfaces

Pak, A.

**DOI**

[10.4233/uuid:20acd275-d9b9-4b75-adc5-d152cf6564ae](https://doi.org/10.4233/uuid:20acd275-d9b9-4b75-adc5-d152cf6564ae)

**Publication date**

2024

**Document Version**

Final published version

**Citation (APA)**

Pak, A. (2024). *Thermoplastic polymers for neural implantable interfaces*. [Dissertation (TU Delft), Delft University of Technology]. <https://doi.org/10.4233/uuid:20acd275-d9b9-4b75-adc5-d152cf6564ae>

**Important note**

To cite this publication, please use the final published version (if applicable).  
Please check the document version above.

**Copyright**

Other than for strictly personal use, it is not permitted to download, forward or distribute the text or part of it, without the consent of the author(s) and/or copyright holder(s), unless the work is under an open content license such as Creative Commons.

**Takedown policy**

Please contact us and provide details if you believe this document breaches copyrights.  
We will remove access to the work immediately and investigate your claim.

# **Thermoplastic polymers for neural implantable interfaces**



# Thermoplastic polymers for neural implantable interfaces

**Dissertation**

for the purpose of obtaining the degree of doctor  
at Delft University of Technology  
by the authority of the Rector Magnificus Prof.dr.ir. T.H.J.J. van der Hagen  
Chair of the Board for Doctorates  
to be defended publicly on  
Thursday, 6th June 2024 at 12:30 o'clock  
by  
**Anna PAK**  
Master of Science in Nanobiophysics  
Technische Universität Dresden, Germany  
born in Karaganda, Kazakhstan.

This dissertation has been approved by the promotor.

Composition of the doctoral committee:

Rector Magnificus	chairperson
Prof. dr. ir. W.A. Serdijn	Delft University of Technology, promotor
Dr. V. Giagka	Delft University of Technology, copromotor

Independent members:

Prof. dr. ir. W. D. van Driel	Delft University of Technology
Prof. dr. J. Dankelman	Delft University of Technology
Prof. dr. ir. J. Vanfleteren	Ghent University, Belgium
Dr. G. Schiavone	University of South-Eastern Norway, Norway
Dr. D. A. Koutsouras	IMEC, the Netherlands



Grant number: Ecsel-783132-Position-II-2017-IA.

Keywords: flexible bioelectronics, microfabrication, polyurethane, liquid crystal polymer, polymers for neural interfaces, soft and conformal microelectrode arrays, chip embedding, long-term encapsulation.

Printed by: Unicorn Kopie und Druck GmbH

Cover designed by: A. Pak

Copyright © 2024 by A. Pak

ISBN: 978-94-6384-600-4

An electronic version of this dissertation is available at:

<http://repository.tudelft.nl>

I dedicate this dissertation to my grandmother, who turns 97 this June. Of Korean descent, she was deported in her young years and has endured a long and challenging life. She will be extremely proud of this milestone of mine, as she has always wished for a better life and education for her children and grandchildren.



# Contents

<b>1. Introduction</b> .....	<b>1</b>
1.1 Problem statement.....	1
1.2 Contribution of this work.....	3
1.3 Overview of the thesis.....	4
<b>2. Biocompatible polymers for neural implants</b> .....	<b>9</b>
2.1 Body response to the implant and material requirements.....	9
2.1.1 Foreign body reaction (FBR).....	9
2.1.2 Material biocompatibility and biostability considerations .....	11
2.2 Polymers used as substrate materials for neural implants .....	12
2.2.1 Polydimethylsiloxane (PDMS).....	12
2.2.2 Polyimide (PI).....	13
2.2.3 Parylene C (ParC).....	14
2.2.4 Thermoplastic Polyurethane (TPU) .....	15
2.2.5 Liquid Crystal Polymer (LCP).....	15
2.2.6 SU-8 (SU-8).....	16
2.3 Polymers used as encapsulation materials for neural implants ....	19
2.3.1 Thermoset polymers processing and polymer-polymer self- bonding techniques .....	20
2.3.2 Thermoplastic polymers processing and polymer-polymer merging .....	21
2.4 Passive polymer-based electrode arrays .....	24
2.5 Assembly of electronic components.....	28
2.5.1 Chip-bonding techniques.....	28
2.5.2 Bumping technologies.....	31
2.5.3 Adhesive types .....	35



2.6 Active polymer-based implants.....	37
2.7 Conclusion .....	41
<b>3. Thin film encapsulation for LCP-based flexible bioelectronic implants .....</b>	<b>49</b>
3.1 Introduction.....	49
3.2 Materials and methods for lifetime estimation.....	51
3.2.1 Preparation of thin film encapsulation (TFE) layers .....	51
3.2.2 Pre-screening of the coatings.....	53
3.2.3 Sorption tests and WVTR calculation .....	54
3.2.4 Adhesion evaluation by adapted ASTM D1876 T-Peel test .....	55
3.2.5 Electrochemical impedance spectrometry (EIS) on IDC structures .....	55
3.3 Results.....	56
3.3.1 Pre-screening of the coatings by soaking and optical inspection .....	56
3.3.2 Barrier properties evaluation with sorption test.....	57
3.3.3 Adhesion evaluation with T-peel test .....	58
3.3.4 Coating performance evaluation with IDC structures .....	60
3.4 Discussion .....	62
3.4.1 Methods used for evaluation of the proposed TFE coatings.....	62
3.4.2 Performance of LCP and TFE coatings.....	63
3.4.3 General Remarks .....	65
3.4.4 Choosing an appropriate coating for each application .....	66
3.5 Conclusion.....	66
<b>4. Thermoplastic polyurethane (TPU) as a base material for flexible neural interfaces .....</b>	<b>71</b>
4.1 Introduction.....	71
4.2 Methods.....	73

4.2.1 Fabrication process.....	73
4.2.2 Accelerated ageing .....	75
4.2.3 Electrode fabrication.....	76
4.2.4 Electrochemical characterization .....	76
4.2.5 In-vivo implantation and statistical analysis .....	77
4.2.6 Dummy and active implant prototypes .....	78
4.3 Results.....	79
4.3.1 Fusion of polyurethane layers and conformal cover of gold tracks .....	79
4.3.2 Electrode characterization .....	80
4.3.3 Biocompatibility and biostability of bioelectronic foils.....	83
4.3.3.1 Biocompatibility.....	83
4.3.3.2 Biostability .....	85
4.3.4 Active neural interface prototypes.....	85
4.4 Discussion .....	88
4.5 Conclusion.....	89
<b>5. Integration of ASIC into TPU-based flexible neural interfaces ...</b>	<b>96</b>
5.1 Introduction .....	96
5.2 Fabrication process.....	96
5.3 RFID and daisy chain chips and substrate layouts.....	97
5.4 Bonding profiles and adhesives .....	98
5.5 Results and conclusion.....	100
<b>6. Conclusions.....</b>	<b>102</b>
6.1 Conclusions .....	102
6.2 Contributions.....	103
6.2 Recommendations.....	104
<b>7. Appendix A.....</b>	<b>109</b>

8. Appendix B.....	113
9. Appendix C.....	117
10. List of Figures.....	120
11. List of Tables.....	126
12. Summary .....	127
13. Samenvatting.....	130
14. Acknowledgments.....	133
15. List of publications.....	135
16. Biography.....	137

# 1

## Introduction

### 1.1 Problem statement

Neural interfaces are developed to establish communication between human-made devices and the nervous system through electrical stimulation of and recording from neural tissues. These devices have the potential to improve the quality of life for individuals suffering from various neurological diseases and disorders [1]–[3]. A typical neural interface system consists of a microelectrode array, which picks up neuronal activity in the form of electrical signals or transmits electrical signals to the neural tissue, and electronic circuitry, which acquires, digitises, and processes these signals and/or stimulates (artificially induces or blocks) neuronal activity. The electronic components are typically silicon chips with integrated circuits and additional passive components that must be protected from the harsh body environment. Conventional methods of protecting the neural implant's electronics by enclosing them in metal (commonly titanium) or ceramic housings have the advantage of being sufficiently hermetic to guarantee decades of operation. At the same time, they face the problem of rigidity and large size. These factors make it challenging to place the electronics in close proximity to delicate neural tissue, which is the target for stimulation and/or recording. Therefore, the electronics must be placed at a certain distance from the target region and connected to the microelectrode array with special leads. This increases the risk of failure, restricts mobility, occasionally results in infection, and can cause discomfort for the patient [4], [5]. There is an emerging need to miniaturise the packaging to overcome these challenges so that the electronics can be placed closer to the target tissue.

Polymers are attractive materials for the packaging of neural implants due to their insulating properties, flexibility, and high mechanical matching to the neural tissue. Polymers are large molecules consisting of repeated units called monomers. In comparison with the metal and ceramic housings,

polymers allow for miniaturisation of the packaging due to the possibility of conformal coating. Properly executed conformal coating with carefully chosen polymers, ensuring sufficient adhesion, cleanliness and barrier properties has the prerequisites to protect the electronics from the surrounding body moisture (more details in Section 2.3). The mechanical properties and fabrication process capabilities of polymers allow to conformally coat electronic components and conductive tracks within the implant. A schematic representation of a conformally-coated neural interface with electrodes, conductive tracks and flip-chip bonded electronics is depicted in Fig. 1.1. Some polymers, such as polyimide (PI), parylene C (ParC), and polydimethylsiloxane (PDMS) also demonstrate neural-tissue biocompatibility [6]-[9]. Fabrication processes employing these biocompatible polymers are typically performed in a layer-by-layer fashion<sup>1</sup> using spin coating or chemical vapour deposition. Because of this layer-by-layer deposition, there is an interface between the two polymer layers (shown with an arrow in Fig. 1.1), which increases the chances of water ingress [10]–[14]. This water ingress happens because polymers are permeable to water vapour, and in case of any void and contamination at the interfaces, water vapour will condense to a liquid state, which might lead to delamination[15] In neural interfaces, patterned metal layers and chips are included between the two polymer layers, and this water ingress may lead to short circuits and corrosion, and, therefore, a further failure of the device.

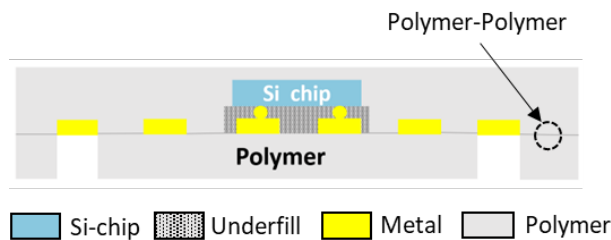


Fig. 1.1. Schematic cross-section illustration of an active implant prototype with its major components and indicated polymer-polymer interface.

<sup>1</sup> In the context of this work a layer-by-layer technique refers to thin polymer film layers, not atomic layers

## 1.2 Contribution of this work

The nature of the polymers used for neural implants can be divided into two types: thermosets and thermoplastics. The main difference between these two types is in their response to heat.

Thermoset polymers undergo an irreversible chemical structure change upon heat, which results in the formation of a strong 3D network of covalent bonds between the polymer chains during the reaction, called cross-links. Once such a bond is formed, it is impossible to reshape or remould it by applying heat. Moreover, if a certain temperature limit is exceeded, the polymer will start to degrade. See Fig. 1.2.

In contrast, thermoplastic polymers have no cross-links between the polymer chains and are interconnected by weak molecular forces. Thermoplastic polymers have covalent interactions between monomer molecules and secondary weak Van-der-Waal interactions between the polymer chains, the latter of which break when heated. Due to weak intermolecular forces, thermoplastic polymers can be reshaped and remoulded without undergoing permanent chemical structural changes. See Fig. 1.3.

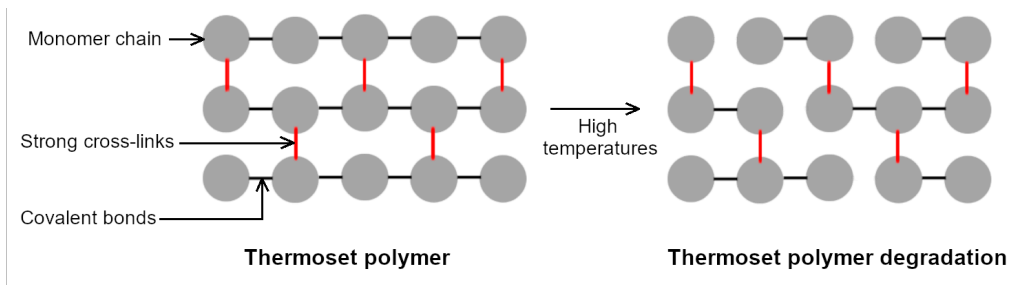


Fig. 1.2. Schematic illustration of the change in the intermolecular structure of a thermoset polymer happening at high temperatures (adapted from [16]).

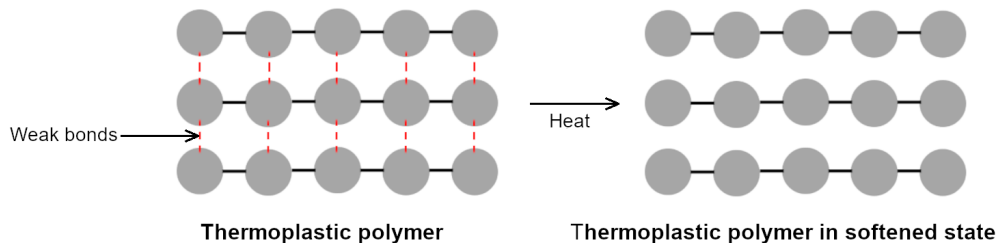


Fig. 1.3. Schematic illustration of the change in the intermolecular structure of a thermoplastic polymer happening at high temperatures (adapted from [16]).

Different classes of polymers, such as silicone elastomers, parylenes, polyimides, liquid crystal polymers, and polyurethanes, are commonly used for biomedical applications. Particular types of these polymers commonly used for implantable neural interfaces are PDMS (Nusil Med1-4213 can be considered for human implantation over 29 days [17]), Parylene C (SCS ParC is ISO 10993 classified [18]), PI (Du Pont PI-2611, non-ISO 10993 certified [19]), LCP (Dyconex ISO 10993-5 in-vitro cytotoxicity tested [20]), TPU (DSM Bionate, used for chronic implantation [21]). The PDMS and PI mentioned above are thermoset polymers, while ParC, LCP and TPU are thermoplastic polymers.

In this work, the thermoplastic behaviour of TPU and LCP polymers is deployed to create a continuous encapsulation layer capable of hosting metal tracks and/or active electronic components. The proposed process involves merging of two, individually deposited, layers of LCP or TPU upon heating, which is not possible to achieve with other polymers currently used for neural interfaces. This approach aims to create inherently more robust encapsulation for the implant by mitigating the potential issues related to water ingress and condensation at the polymer-polymer interface. Furthermore, this work introduces a novel platform technology for the conformal coating of the gold tracks and embedding of a thin application-specific integrated circuit (ASIC), where, for the first time, TPU is used as a substrate for the neural interfaces. This platform technology opens new possibilities for the development of soft (with the elasticity very close to soft human tissue) high-density and small-feature-size active neural interfaces.

### 1.3 Overview of the thesis

This thesis demonstrates the potential and benefits of using thermoplastic polymers for neural interfaces, specifically focusing on thermoplastic polyurethane and liquid crystal polymer. The outline of the thesis is organised as follows.

**Chapter 2** gives a literature overview of polymers used for neural implants. It describes the reactions that happen upon implantation within the body in proximity to the device, as well as basic requirements for implantation, such as biocompatibility and biostability (Section 2.1). The chapter focuses on the main properties and advantages of different polymers commonly used as substrates and coating materials for neural implants (Section 2.2 and Section 2.3). The main characteristics of the described polymers are summarized in a comparison table. This chapter also gives different examples of using the described polymers for passive and active neural implants, together with their processing steps (Sections 2.4 and 2.5). Furthermore, this chapter provides a literature overview of different assembly techniques employed in the integration of electronic components with a focus on Application-Specific Integrated Circuits (ASICs). A review of different bonding techniques, bumping technologies, and adhesive types is made in this chapter (Section 2.6).

**Chapter 3** describes thin-film encapsulation materials for LCP-based flexible substrates using a  $\text{HfO}_2$ -based atomic-layer-deposition (ALD) multilayer, a hybrid ParC-ALD multilayer, and an LCP coating layer, of which the latter serves as a reference (Section 3.2). Results of the encapsulation performance of these coatings using different test methodologies, such as T-peel, water-vapour-transmission-rate (WVTR) and long-term electrochemical-impedance-spectrometry (EIS) tests, are presented in this chapter (Section 3.3).

**Chapter 4** describes the step-by-step fabrication of a polyurethane-based electrode array with gold interconnects (Section 4.1) and assesses its integrity in the conditions mimicking the human body environment. The assessment is made by soaking tests at body ( $37^\circ\text{C}$ ) and elevated temperatures ( $67^\circ\text{C}$ ) (Section 4.2). This chapter also demonstrates the electrochemical characterisation of the electrode array, including impedance spectroscopy, cyclic voltammetry and voltage-transient measurements (Section 4.3). The mechanical and in-vivo characterisations are presented in Appendix B and Sections 4.3, respectively.

**Chapter 5** demonstrates ASIC integration into the, previously described in Chapter 4, polyurethane-based electrode array. Flip-chip bonding technology was employed to integrate less than  $100\ \mu\text{m}$  thin chips into the polymer



array and connect them to the gold metallization tracks using an anisotropic conductive adhesive.

**Chapter 6** presents the conclusions of this thesis, highlights its scientific contributions and gives some suggestions for future work.

## References

- [1] C. N. Heck *et al.*, "Two-year seizure reduction in adults with medically intractable partial onset epilepsy treated with responsive neurostimulation: Final results of the RNS System Pivotal trial," *Epilepsia*, vol. 55, no. 3, pp. 432–441, Feb. 2014, doi: 10.1111/epi.12534.
- [2] F. B. Wagner *et al.*, "Targeted neurotechnology restores walking in humans with spinal cord injury," *Nature*, vol. 563, pp. 65–71, Nov. 2018, doi: 10.1038/s41586-018-0649-2.
- [3] N. C. Swann *et al.*, "Adaptive deep brain stimulation for Parkinson's disease using motor cortex sensing," *J Neural Eng*, vol. 15, no. 4, pp. 1–10, May 2018, doi: 10.1088/1741-2552/aabc9b.
- [4] D. Klug *et al.*, "Systemic infection related to endocarditis on pacemaker leads: Clinical presentation and management," *Circulation*, vol. 95, no. 8, pp. 2098–2107, Apr. 1997, doi: 10.1161/01.CIR.95.8.2098.
- [5] W. G. De Voogt, "Pacemaker leads: Performance and progress," *American Journal of Cardiology*, vol. 83, no. 5, pp. 187–191, Mar. 1999, doi: 10.1016/S0002-9149(98)01022-4.
- [6] J. S. Ordonez, C. Boehler, M. Schuettler, and T. Stieglitz, "Improved polyimide thin-film electrodes for neural implants," *2012 Annual International Conference of the IEEE Engineering in Medicine and Biology Society*, pp. 5134–5137, Sep. 2012, doi: 10.1109/EMBC.2012.6347149.
- [7] Ivan R. Mineev *et al.*, "Electronic dura mater for long-term multimodal neural interfaces," *Science*, vol. 347, no. 6218, pp. 154–159, Jan. 2015, doi: 10.1126/science.1260960.
- [8] D. C. Rodger *et al.*, "Flexible parylene-based multielectrode array technology for high-density neural stimulation and recording," *Sens Actuators B Chem*, vol. 132, no. 2, pp. 449–460, Jun. 2008, doi: 10.1016/j.snb.2007.10.069.

- [9] A. Carnicer-Lombarte *et al.*, "Mechanical matching of implant to host minimises foreign body reaction," *Bioarxiv*, pp. 1–41, Nov. 2019, doi: 10.1101/829648.
- [10] J. Ortigoza-Diaz *et al.*, "Techniques and considerations in the microfabrication of parylene c microelectromechanical systems," *Micromachines (Basel)*, vol. 9, no. 9, pp. 1–25, Jul. 2018, doi: 10.3390/mi9090422.
- [11] M. Tintelott and A. Schander, "Understanding Electrical Failure of Polyimide-Based Flexible Neural Implants : The Role of Thin Film Adhesion," *Polymers (Basel)*, vol. 14, no. 18, pp. 1–11, Sep. 2022, doi: 10.3390/polym14183702.
- [12] R. P. Von Metzen and T. Stieglitz, "The effects of annealing on mechanical , chemical , and physical properties and structural stability of Parylene C," *Biomed Microdevices*, vol. 15, pp. 727–735, Mar. 2013, doi: 10.1007/s10544-013-9758-8.
- [13] K. Koh, J. Chin, J. Chia, and C. Chiang, "Quantitative Studies on PDMS-PDMS Interface Bonding with Piranha Solution and its Swelling Effect," *Micromachines (Basel)*, vol. 3, no. 2, pp. 427–441, May 2012, doi: 10.3390/mi3020427.
- [14] M. A. Eddings, M. A. Johnson, and B. K. Gale, "Determining the optimal PDMS-PDMS bonding technique for microfluidic devices," *Journal of Micromechanics and Microengineering*, vol. 18, no. 6, pp. 1–4, Apr. 2008, doi: 10.1088/0960-1317/18/6/067001.
- [15] A. Vanhoestenberghes and N. Donaldson, "Corrosion of silicon integrated circuits and lifetime predictions in implantable electronic devices," *J Neural Eng*, vol. 10, no. 3, May 2013, doi: 10.1088/1741-2560/10/3/031002.
- [16] "Difference Between Thermoplastic and Thermosetting Plastic," <https://pediaa.com/difference-between-thermoplastic-and-thermosetting-plastic/>.
- [17] Avantor Sciences, "Nusil MED 4213 [Data Sheet]," 2020. Accessed: Jul. 17, 2023. [Online]. Available: <https://www.avantorsciences.com/nusil/en/product/MED-4211/low-viscosity-silicone-elastomer>

- [18] Speciality Coating Systems, "SCS Parylene Properties [Data sheet]," 2018. Accessed: Jul. 17, 2023. [Online]. Available: <https://scscoatings.com/technical-library/>
- [19] HD Microsystems, "Polyimide PI 2611 Data Sheet [Data sheet]," 2003. Accessed: Jul. 17, 2023. [Online]. Available: <https://rndmate.com>
- [20] Micro Systems Technologies, "Liquid Crystal Polymer (LCP) [Data Sheet]," 2020. Accessed: Jul. 17, 2023. [Online]. Available: <https://www.mst.com/technologies/interconnect-organic/lcp>
- [21] DSM Biomedical, "Bionate ® Thermoplastic Polycarbonate Polyurethane (PCU) [Data sheet]," 2020. Accessed: Jul. 17, 2023. [Online]. Available: [www.dsm.com/medical](http://www.dsm.com/medical)

# 2

## Biocompatible polymers for neural implants

### 2.1 Body response to the implant and material requirements

#### 2.1.1. Foreign body reaction (FBR)

Various polymers are available on the market or currently under investigation for use as substrates in neural implant applications. These polymers have to be wisely chosen since the introduction of any new material into the body will prompt a corresponding response and the internal body environment will try to either "digest" or put a "barrier" on the implanted device. This response is known as a foreign body reaction and is shown step by step in Fig. 2.1. In the first seconds of implantation, proteins derived from the extravasated blood (such as albumin and fibrinogen) and surrounding wound fluid adsorb to the surface of the implant. Within the next few minutes, neutrophils (a type of white blood cells that act as the immune system's first line of defence) adhere to the recently formed protein layer, leading to further attraction of monocytes (the largest type of white blood cells). The monocytes start to differentiate into macrophages, which in turn start proliferating within the lesion. Within the next few days, the process of cell population and covering of the implant continues fusing the macrophages into larger cells (foreign body giant cells), forming the isolation layer, and trying to phagocyte the implant. At this stage, implants made of biodegradable materials should already have performed or be in the process of performing their therapeutic function and are being degraded. Otherwise, if the implant is not biodegradable, the fibrotic (chronic foreign body reaction) process begins. During this process, macrophages recruit fibroblasts, which in turn start to deposit extracellular matrix proteins. This

process leads to the encapsulation of the implant with the fibrotic tissue. More details of the whole process are described in [1].

In the end, the foreign body reaction will partially help with the fixation of the implant but will also create a certain barrier that will have to be overcome by any sensing or actuating elements used for neural interaction, e.g. when stimulating or acquiring signals from the target cells. The FBR response depends on different factors, like the mechanical and chemical properties of the material from which this implant is made, size, and cleanliness. Therefore, to get a mild foreign body reaction and proper implant functioning, the materials should fulfil certain criteria before being implanted inside the human body.

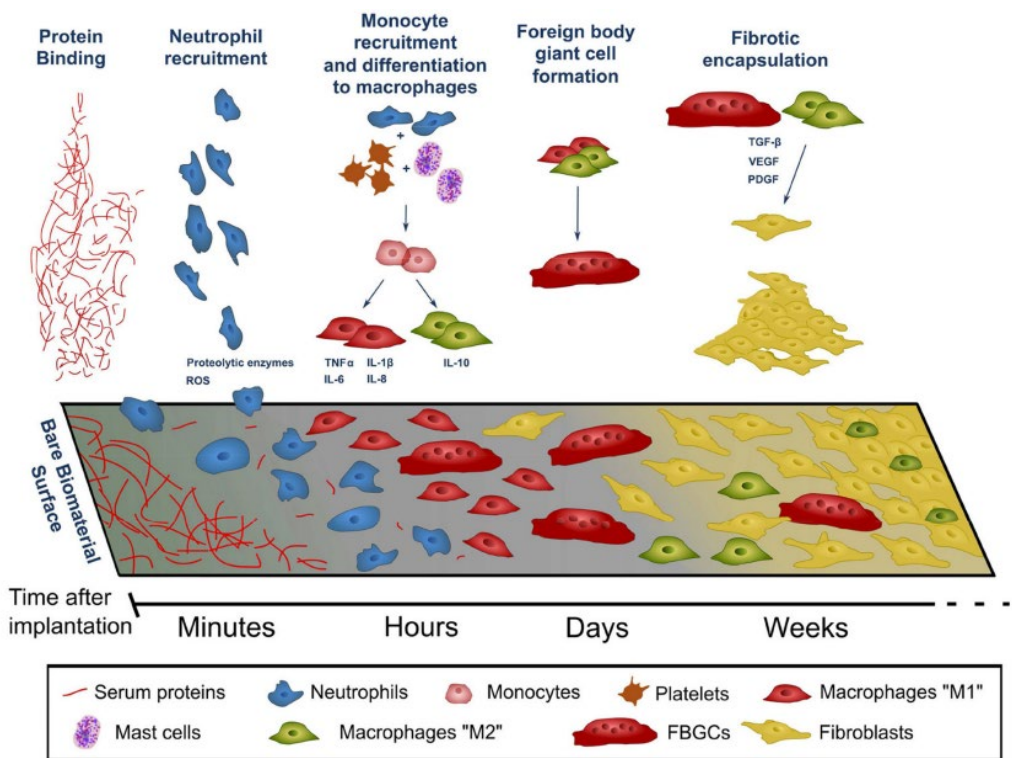


Fig. 2.1. The phases of the Foreign Body Reaction to the implant. Reproduced from [1].

### 2.1.2 Material biocompatibility and biostability considerations

USP class VI is a set of tests from the U.S. Pharmacopeia (USP) organisation [2]. USP class VI is usually considered a minimum requirement for the material to be used in medical applications. Particularly, USP publishes test instructions for plastics and polymers used in surgical equipment or medical devices. The USP class VI tests include: systemic injection, intracutaneous, and implantation tests. Systemic injection (systemic toxicity) test measures toxicity and irritation caused by the sample applied to the skin, administered orally, and inhaled. Intracutaneous test measures toxicity and localized irritation caused by the sample brought in contact with tissue that the device will be in contact with. Implantation test measures toxicity, infection, and irritation caused by the sample's intramuscular implantation into a test animal over several days.

A later introduced standard that consists of more extensive tests and is commonly used for the evaluation of *the biocompatibility* of medical devices nowadays is ISO 10993 [3]. Biocompatibility is usually defined as "the ability of the material to perform with an appropriate host tissue response in a specific application" [4]. According to the ISO 10993 standard, the device that is planned to be implanted and stay within the body for more than 24 hours while being in contact with the tissue or bone will have to be checked for cytotoxicity, sensitisation, irritation or intracutaneous reactivity, acute systemic toxicity, subacute toxicity, genotoxicity, implantation and hemocompatibility. While the ISO 10993 standard describes the surface biocompatibility of the device, the structural biocompatibility, i.e., mechanical match between the implant and the tissue, depends on the size, shape, and softness (Young's Modulus) of the implant. The smaller size, smoother edges, and better elastic modulus matching between the tissue and the substrate material (Fig. 2.2) of the implant will all result in better biointegration and longer functionality of the device [5], [6]. Testing of structural biocompatibility is first performed in animals during chronic in-vivo studies and only then possible in humans.

The other important criterion that must be met is ensuring the *biostability* of the implant, meaning that the implant maintains its key performance characteristics over the course of its use. One of the examples of these characteristics would be absence of delamination and corrosion of the materials. Biostability is usually first tested in accelerated ageing conditions, commonly in saline, under elevated temperatures and applied bias. Then the test is repeated in animals.

Material	Spinal cord & gray matter	Muscle	PDMS	TPU	ParC	PI	LCP	Bone
Young's modulus (MPa)	0.003 [7]	0.007 [7]	0.360-0.870 [8]	≈30 at 10°C ≈12 at 80°C [9]	2800 [8]	3100 [8]	1600 [10]	14800 [11]

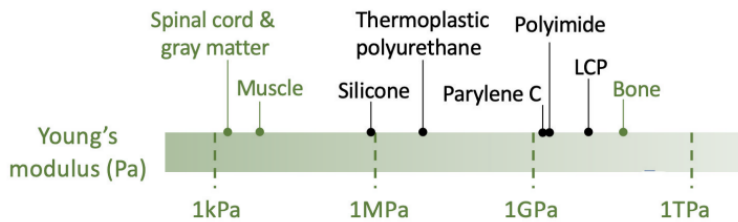


Fig. 2.2. Graphical and tabular representation of the elastic modulus of various biological tissues and materials used as substrates for neural implants.

## 2.2 Polymers used as substrate materials for neural implants

This section will discuss various materials commonly used as substrates for neural implants, focusing mainly on their biocompatibility and chemical structure. A comparison table of the mechanical, electrical and thermal properties of the given materials is presented in Table 2.1, at the end of the section.

### 2.2.1 Polydimethylsiloxane (PDMS)

PDMS silicone elastomer is one of the most commonly used polymers when it comes to medical devices. The first published record of implanted silicone

elastomer dates to 1946, when Dr. Lahey implanted the PDMS tube for duct repair in biliary surgery [12]. Silicones are widely used in medical applications for life-saving devices, such as, bladder implants, hydrocephalus shunts or pacemaker leads. The success of PDMS-based medical devices is in their mechanical matching to the soft host tissue, therefore, high biocompatibility. Medical-grade PDMS elastomers satisfy the ISO 10993 biocompatibility standards and exhibit durability in long-term used implants [13].

The mechanical success of PDMS can be explained by its chemical structure (Fig. 2.3), consisting of  $(\text{CH}_3)_2\text{SiO}$  repeating units. Si-O-Si backbone flexibility and linearity of the chemical structure allow for easy movement and bending, providing PDMS with high elasticity without getting cracks. Exposed  $\text{CH}_3$  methyl groups provide PDMS with low surface energy, repelling polar substances like water and making it hydrophobic. Stable Si-O gives PDMS thermal stability and high biocompatibility, not reacting with biological molecules.

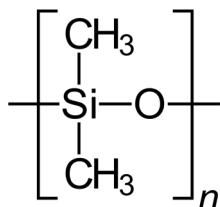


Fig. 2.3. PDMS chemical structure [10].

## 2.2.2 Polyimide (PI)

Polyimides (PIs) are known for their mechanical strength, high thermal stability, high glass transition temperature and inertness to solvent. Biphenyltetracarboxylic dianhydride p-phenylenediamine (BPDA-PPD), a particular type of PI that is often used in biomedical implant research. . The BPDA-PPD (chemical structure shown in Fig. 2.4) aromatic rings provide the material with stiffness, while the imide group (-CONHCO-) contributes to its high thermal and mechanical stability.

Although this type of PI, commercially known as PI-2611 (Du Pont, HD Microsystems), is not certified according to ISO 10993, devices using this



material were approved as safe. One of the examples is the Argus II Retinal Prosthesis System, a commercially available device used in blind patients with retinitis pigmentosa to provide them with artificial vision, which uses a 13- $\mu\text{m}$  thick PI substrate [14]. Another example is the NeuroOne cortical and subdural brain implant manufactured with 80  $\mu\text{m}$  polyimide film. The Neuralink prototype for a high-density brain-machine interface also uses 4-6  $\mu\text{m}$  thick PI [15].

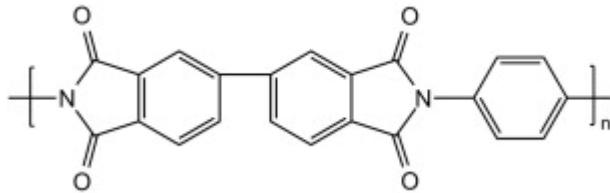


Fig. 2.4. Chemical structure of PI 2611 [10].

### 2.2.3 Parylene C (ParC)

Chlorinated poly-para-xylylene polymer (ParC) is widely used as a substrate material due to its combination of dielectric properties, biocompatibility, and low permeability to moisture [16], [17]. Moreover, parylene C is a chemically and biologically inert material [18].

Parylene C is a semicrystalline polymer consisting of crystalline and amorphous parts. Crystalline parts, in the form of aromatic rings (Fig. 2.5) provide the polymer with rigidity and mechanical and chemical stability. While amorphous parts give it flexibility and thermoplasticity, allowing it to be thermoformed [19] when heated between the glass transition temperature ( $\sim 90\text{ }^\circ\text{C}$ ) and melting point ( $290\text{ }^\circ\text{C}$ ). Thermoforming has to be conducted in a vacuum chamber, since ParC undergoes thermal oxidative degradation at temperatures above  $125\text{ }^\circ\text{C}$ , in the presence of oxygen. At these temperatures, the amorphous parts start rearranging, making the polymer soft and possible to reshape. Cooling down to a temperature below the glass-transition temperature brings it to the state where the shape is retained.

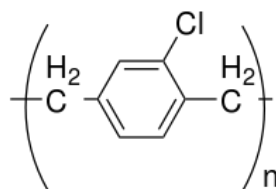


Fig. 2.5. ParC chemical structure [10].

## 2.2.4 Thermoplastic Polyurethane (TPU)

TPU is a soft, transparent, translucent thermoplastic polymer, which is available in a medical-grade form (USP Class VI) [20]. In fact, thermoplastic polyurethanes (TPUs) have a long use history in medical devices as insulators for pacemaker leads, vascular and intravenous catheters [21], [22] and vascular grafts [23]. Moreover, the material was recently modified to become bioresorbable [24].

The elastic modulus of TPU lies within the same range as the elastic modulus of PDMS, which are the softest biocompatible polymers used for neural implants (Fig. 2.2). TPU is a thermoplastic polymer consisting of hard (urethane C<sub>3</sub>H<sub>7</sub>N<sub>2</sub>O<sub>2</sub>) and soft segments (ether). Soft ether segments allow TPU to melt and reform under temperature.

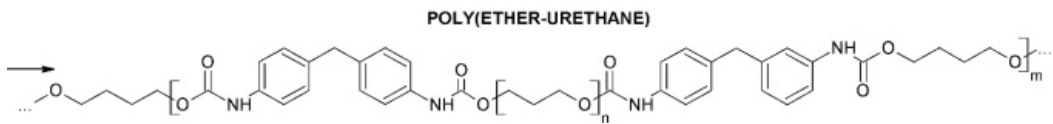


Fig. 2.6. Chemical structure of PU (Ether) [25].

## 2.2.5 Liquid Crystal Polymer (LCP)

LCP is biocompatible (according to ISO 10993-5 in-vitro cytotoxicity tests) and generally considered safe for use within the body [26], [27], demonstrating promising results in in-vitro soak and long-term biostability assessments in rodents [28]. The advantage of LCP is the same as TPU: it is thermoplastic, which means that it can be merged with itself. Equally important advantages include strength, flexibility and superior moisture absorption properties compared to other polymers [29].

LCP consists of interchanging rigid and flexible monomer units (Fig. 2.7). Rigid units provide LCP with mechanical stability and high-temperature endurance, while flexible monomer units provide processing capabilities.

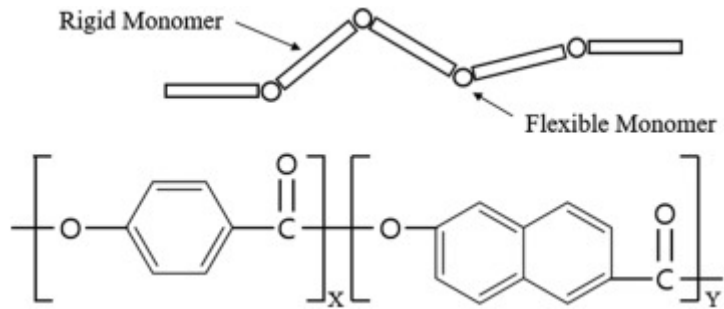


Fig. 2.7. Chemical structure of LCP [30].

### 2.2.6 SU-8

SU-8 is a negative photoresist (PR) built of four bisphenol A units connected to each other with eight monomer phenyl rings (Fig. 2.8). To obtain SU-8 resin, the monomers are dissolved in the organic solvent solution that acts as a photoacid generator (PAG). To create a SU-8 thin film substrate, the solution is usually spin-coated on top of a silicon wafer (an extra sacrificial layer can be added on the wafer for easier release), after that the layout design is transferred to the photoresist via standard lithography using a photomask. The next step is the ultraviolet (UV) exposure at 350-400 nm wavelength, during which the PAG is decomposed, and the acid is generated, followed by an acid-catalysed, post-exposure baking step to allow monomers to polymerise.

The advantage of using SU-8 as a neural device's substrate material is fine resolution, chemical inertness, and thermal stability. Nevertheless, no study or proof concludes that SU-8 satisfies all the biocompatibility requirements according to ISO 10993.

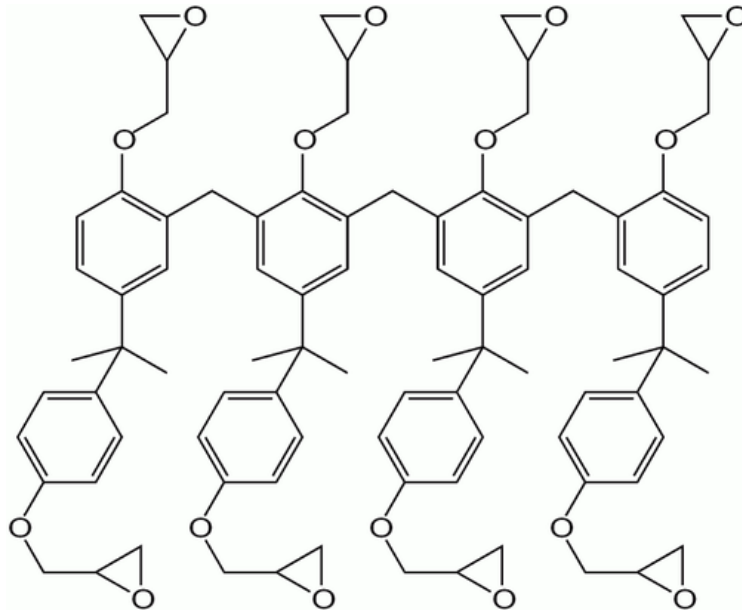


Fig. 2.8. SU-8 chemical structure [10].

Material	SU-8	PI	LCP	ParC	TPU	PDMS
Young's modulus [MPa]	2000-7500 [77]	3100 [8]	10000-40000 [8]	2800 [8]	~ 30 MPa @ 10 °C [9] ~ 12 MPa @ 80 °C [9]	360-870 [8]
Processing temp. limits [°C]	Tg=200-210°C [10] Tdec=300-315°C [10]	Tg=325-410°C [31] Td=510-620 °C [31]	Tmelt=280 °C [10]	Tglass=90°C [31] Toxd=125°C [31] Tmelt=290°C [31]	Tsoft=155-175 °C [32]	Tglass=150°C [8] Tmelt=226-232°C [8] Td=350°C [11]
Density [g/cm <sup>3</sup> ]	1.075-1.238 [10]	1.10-1.11 [10]	1.4 [10]	1.289 [10]	1.17 [32]	1.08 [10]
Gas permeability [(cm <sup>3</sup> mm)/(m <sup>2</sup> day atm)]	not available	N <sub>2</sub> =2.3 [31] CO <sub>2</sub> =17.3 [31] O <sub>2</sub> =9.6 [31] H <sub>2</sub> =96.3 [31]	O <sub>2</sub> =0.9 [33] H <sub>2</sub> =78 [33]	N <sub>2</sub> =0.4 [34] CO <sub>2</sub> =2.8 [34] O <sub>2</sub> =3.3 [34] H <sub>2</sub> =43.3 [34]	N <sub>2</sub> =31.5 [35] CO <sub>2</sub> =1.18 [35] O <sub>2</sub> =78.7 [35]	N <sub>2</sub> =1.8-2.6·10 <sup>4</sup> [31] CO <sub>2</sub> =2.1-2.5·10 <sup>5</sup> [31] O <sub>2</sub> =3.9-5.3·10 <sup>4</sup> [31] H <sub>2</sub> =4.3-5.8·10 <sup>4</sup> [31]
Dielectric coefficient	3.2 (at 10MHz) [10]	3.5 (at 1kHz) [10]	3 (at 1MHz) [10]	3.1 (at 1kHz) [10]	3.8-4.4 (at 1 MHz) [35]	2.6-3.8 (at 50 Hz) [10]
Electrical resistivity [Ω cm]	7.8×10 <sup>14</sup> [10]	>10 <sup>16</sup> [10]	10 <sup>13</sup> [10]	>10 <sup>16</sup> [10]	10 <sup>13</sup> [35]	10 <sup>15</sup> [10]
Thermal conductivity [W/(cm K)]	0.02-0.003 [10]	0.29 [10]	not available	8.2 [10]	11 [35]	15-25 [10]
Possible layer thickness [μm]	1-300 [10]	1-15 [10]	25-3000 [10]	1-100 [10]	10-100*	10-100 [10]
WVTR (requirement 10 <sup>-6</sup> -10 <sup>-3</sup> ) [g/m <sup>2</sup> /day]	not available	4.3 [36]	0.2 [37]	8.2*	181*	3.4*
Moisture absorption [%]	0.55-0.65% [10]	0.8-1.4% [10]	0.03% [10]	0.06% [10]	0.6-0.8 [34]	<1% [10]
Elongation (%)	4.8-6.5% [10]	30% [10], 5-7 [8]	3.4% [10]	200% [10]	500% (thermoset) [8]	600% [10]
Biocompatibility	not certified	not certified	USP class VI [10]	USP class VI [10]	medical grade	USP class VI [10]
Precursor	N/A [10]	BPDA/PPD [10]	N/A [10]	DPX-C [10]	N/A	N/A [10]

Table 2.1. Comparison of the material properties of polymers used for fabrication of neural implants. Values adapted from the references, besides the measurements marked with \*, which were performed at Fraunhofer labs. Tg – glass transition temperature, Tm – melting temperature, Td - thermal degradation temperature, Toxd – thermal oxidative degradation temperature.

### 2.3. Polymers used as encapsulation materials for neural implants

As mentioned in Chapter 1, the most common method of protecting active neural-implant electronics is either in titanium or ceramic housings with the “feedthroughs” interconnecting electronics inside the housings with the electrodes. The advantage of this method is that it is hermetic, meaning that it is an airtight seal that does not allow gas and moisture to penetrate. However, the drawback of this interconnection is that the number of these feedthroughs still remains an unsolved technological challenge when it comes to scalability. Moreover, hermetic housing is bulky and rigid; therefore, it does not allow the electronics to be in close proximity to the stimulated/recorded regions and, in case of metal packaging, it also does not allow electromagnetic signals to pass through. Using polymer materials for implant encapsulation offers several advantages, such as the minimal foreign body reaction of the neural tissue, good electrical insulation properties, mechanical flexibility and the possibility of integrating metal tracks and electronic components in one piece. However, the main challenge of using polymers as encapsulation materials is their permeability to water vapour. In case of any void, loss of adhesion or contamination between the polymer and any other underlying interface of the implant, the water vapour will go through the polymer and condense into a liquid [38]. An example of a polymer-polymer interface with possible contamination or void is shown in Fig. 2.9 (a),(b). In the long term, such contamination or void would lead to delamination, corrosion of the underlying metals, a short between the metal tracks and further failure of the implant. Therefore, a well-established cleaning process and good adhesion at these interfaces are crucial for the long-term, uninterrupted functioning of the implant. Various fabrication techniques for improving polymer-polymer interface adhesion are described in the next chapter.



Fig. 2.9. Water ingress mechanisms: (a) contamination or (b) void formation due to loss of adhesion happening at the polymer-polymer interface.

### 2.3.1 Thermoset polymer processing and polymer-polymer self-bonding techniques.

PDMS is a thermoset polymer, generally consisting of two parts: a pre-polymer base and a cross-linking agent, commonly mixed in a 10:1 ratio, respectively. Once they are homogeneously mixed, forming a low-viscosity liquid, the polymerisation process starts. At this time, the mixture is flowable and can be spin-coated or moulded into a certain shape and size. Once the mixture spreads evenly and takes the desired shape, an elevated temperature (60-80 °C) is usually applied to speed up the polymerisation process. During this process, a stable cross-linked PDMS polymer chain is formed. Once it is formed, it is very stable and difficult to break. Therefore, when using PDMS as an encapsulation material on top of the PDMS polymerised substrate, good adhesion between the PDMS layers is required. The top PDMS layer is usually either spin-coated or just poured on top of the substrate layer. Different techniques, such as partial curing, oxygen plasma treatment, corona discharge and application of adhesion promoters, are used to enhance adhesion between the layers. Fig. 2.10 (a,b) shows PDMS-PDMS interfaces treated with a corona discharge and chemical solutions aimed at improving adhesion. In both pictures, we can explicitly see the interface between the two layers.

PI is another thermoset polymer, usually produced as follows: spin-coating of the polyamic acid (PAA) to obtain the desired film thickness, pre-curing to partly evaporate the solvent (~125 °C), imidization (125-300 °C) and annealing (~350 °C). Polyimide is compatible with standard lithography processing, allowing for achieving high-resolution electrodes on top of its surface [15]. The most common way of microfabrication of PI neural meshes is by spin-coating the first substrate layer, creating electrodes, and spin-coating the top

encapsulation layer. Since good adhesion between the layers is required for long-term stable operation in neural implants, different techniques to improve PI-PI adhesion, such as oxygen plasma, partial curing, alkaline KOH and NaOH, and amine solution treatments are commonly used. Fig. 2.10 (c),(d) shows PI-PI interfaces treated with plasma. We can explicitly see the interface between the PI-PI layers, and even sometimes, one of the layers delaminates due to poor adhesion of the layers.

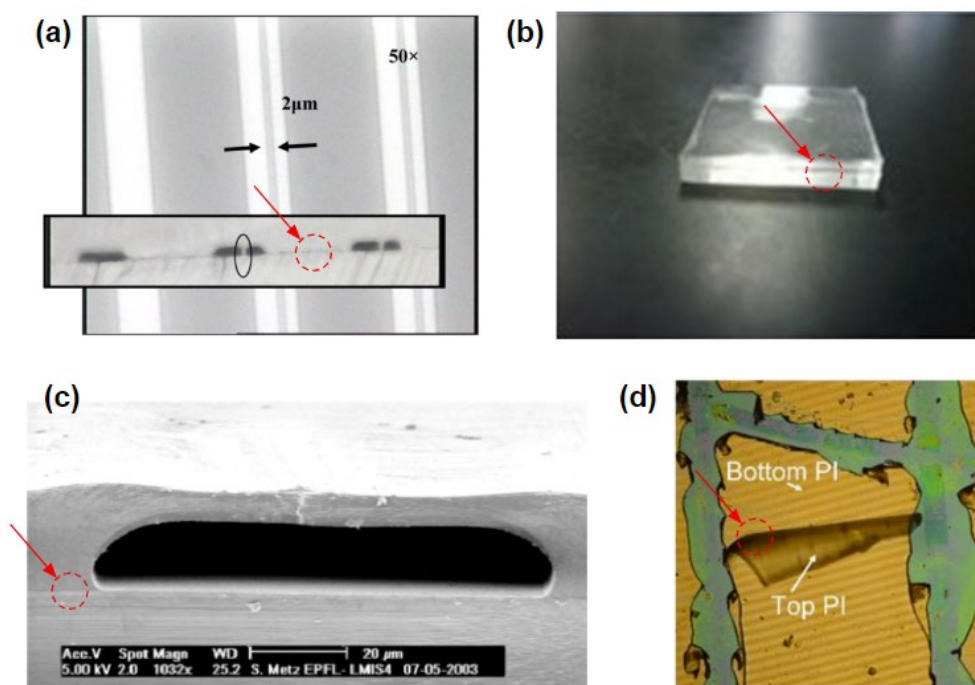


Fig. 2.10. Polymer-polymer interface of thermoset polymers treated with different techniques aimed to improve adhesion: PDMS-PDMS interface after (a) corona discharge [39] and (b) piranha solution [40] treatment, and (c), (d) PI-PI interfaces after plasma treatment [41],[42]. In the red dotted circles, the PDMS-PDMS (a,b) and PI-PI interfaces (c,d) are highlighted.

### 2.3.2 Thermoplastic polymer processing and polymer-polymer merging.

ParC synthesis happens at about 0.1 torr pressure and starts with the heating of solid raw material, called dimer (di-para-xylylene), in a vacuum chamber until it is sublimed. This dimeric gas is pyrolysed into monomers (para-



xylylene). The monomers are deposited, molecule by molecule, to form a conformal thin-film layer (poly(para-xylylene)). The thickness of such a layer can range from tens of nanometres and reach up to a few millimetres [34]. Initially used as coating material, allowing to conformally cover the substrate or electrical components from all sides and even sharp edges and microscale gaps [43], nowadays, it is used to develop ParC substrate-based devices. Although ParC has a thermoplastic nature [19], because of its low mechanical strength, limited thermal budget and lack of well-defined protocols for Parylene C substrate-based devices fabrication, it faces the problem of delamination (shown in Fig. 2.11), cracking and bubbling. As a result of film stress and difference in coefficients of expansion, Parylene C has poor adhesion to noble metals and to itself. A number of techniques, such as adhesion promoter, oxygen plasma treatment, nitrogen environment and thermal annealing are used in order to improve ParC adhesion.

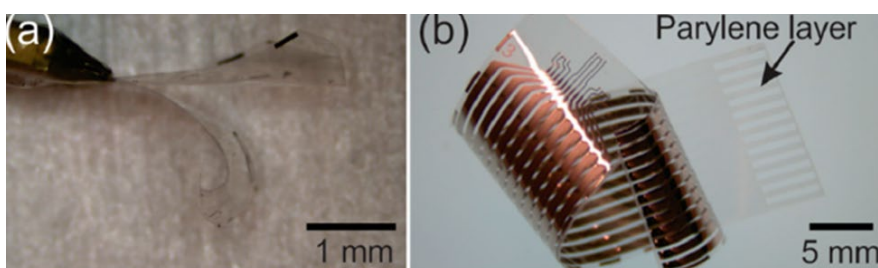


Fig. 2.11. ParC-ParC delamination after annealing [44].

TPU is a thermoplastic polymer that can be obtained in various forms, such as sheets, pellets, or tubes. To utilise TPU as a substrate and/or encapsulation material, the most convenient form would be sheets. The most common way to obtain thin homogeneous sheets of TPU is by blown film extrusion. The process starts with putting the material, either in the form of two components, polyol and isocyanate, or in the form of pellets into the barrier screw, where they will mix and be transported into the barrel. Then the beads or the mixture is heated till melting. When the melted material reaches the end of the barrel, it is extruded through the die. The circular die has a hole through which air is blown to inflate the polymer into a tube. The speed of inflation and extrusion will define the thickness and width of the polymer sheet. The inflated tube is then cooled down and moved upward with the

rollers to create a film, which is eventually wound into rolls. Usually, the film thickness ranges from 20 to 1000  $\mu\text{m}$ . Polytetrafluoroethylene (PTFE) rollers will be selected if a matt film surface is required [45].

The most common way of using TPU in biomedical implants nowadays is as an insulation for pacemaker leads, intravenous catheters, or other types of tubings. These tubes are manufactured by extrusion in tubular form. A more detailed manufacturing process is described in [45].

TPU can be used as a coating and substrate material due to its thermoplasticity and ability to merge with itself, therefore getting rid of the polymer-polymer interface. This phenomenon is neither widely implemented in practice nor discussed in the literature, but one of the examples of thermally activated self-bonding is shown in Figure 2.12 (a).

LCP is an attractive coating material due to its thermoplasticity and the possibility of getting rid of the polymer-polymer interface (Figure 2.12 (b)), the possibility of thermoforming into different shapes, and low water permeability.

LCP can be sourced in the form of sheets with a predefined thickness ranging from 25 to 3000  $\mu\text{m}$ . A common way of LCP-based microelectrode-array fabrication is by using two types of LCP: high melting-temperature LCP (HT-LCP, 310  $^{\circ}\text{C}$ ) as a substrate and low melting-temperature LCP (LT-LCP, 280  $^{\circ}\text{C}$ ) as an encapsulation material bonded to each other by applying certain temperature and pressure. An example of an LCP-based electrode array with gold electroplated electrodes is shown in Fig. 2.12(b).

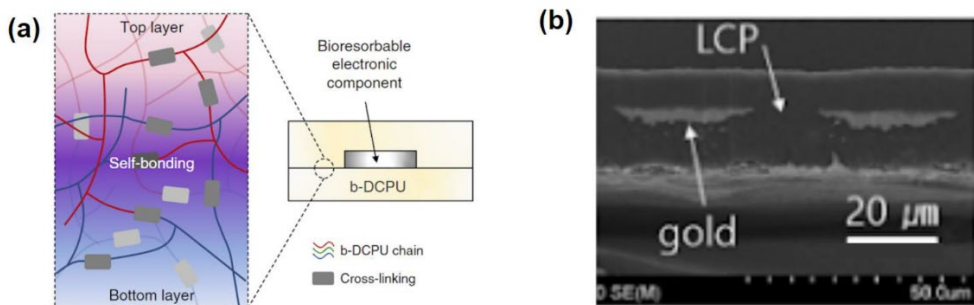


Fig. 2.12. Schematic illustration of the self-bonding and merging of bioresorbable dynamic covalent polyurethane (b-DCPU) layers induced by

heat without the use of any adhesives (a) [24]. A cross-sectional SEM image of the thinned LCP electrode array after thermocompression bonding (b) [30].

## 2.4 Passive polymer-based electrode arrays

This section describes various methods for fabricating passive electrode arrays using the polymers mentioned earlier. The focus here is on elucidating the way polymer materials are applied and integrated with the metal deposition. However, the processes of applying a release layer, removing the array from the wafer, connecting it to an external connector, and integrating it with an acquisition system are not discussed because they are not relevant to the current context.

In 2007, Rodger et al. developed a parylene-based, high-density electrode array (1024 electrodes, 75- $\mu\text{m}$ -diameter each) for retinal stimulation (Fig. 2.13(a)) [46]. The retinal electrode array was fabricated using a dual-metal-layer process. An eight micrometres-thick ParC substrate layer was first deposited on a silicon wafer, followed by a platinum or platinum-titanium lift-off process (comprising PR spinning, bake and development, metal deposition, and lift-off in solvent), forming a 16  $\mu\text{m}$  pitch and 2000-3000  $\text{\AA}$  thick metal layer. The second ( $\sim 1 \mu\text{m}$  thick) ParC layer is deposited on top to form the insulation between the existing and next metallisation layers. Another PR layer is spun, exposed and developed on top of the insulation layer. The vias are formed in this layer using an oxygen plasma reactive ion etching (RIE) process. A second optimised lift-off process is used to form the second metallisation layer, keeping the electrical continuity with the underlying metal layer. A final parylene top coating ( $\sim 7 \mu\text{m}$  in thickness) is applied, followed by the previously described via-opening step. An annealing process (2 days at 200  $^{\circ}\text{C}$  in a vacuum oven filled with nitrogen gas, helping to get rid of the voids) is applied to improve the parylene-parylene adhesion. The chronic biostability was evaluated by implanting the array in the right eye of two canines. A 6-month follow-up analysis demonstrated normal blood perfusion inside the vessels underneath the array.

In 2009, Rubehn et al. fabricated a 252-channel electrocorticogram (EcoG) electrode array for recording from the cortical surface of macaque monkeys (Fig. 2.13(b)) [47]. The array was made by spin coating a 5  $\mu\text{m}$  thick PI film on

a Si substrate, followed by standard MEMS processing and subsequent platinum sputtering of the electrode sites and connector paths. After activating the PI surface in oxygen plasma, a second 5 $\mu\text{m}$  thick PI layer was spin-coated on top. A plasma-etching step was used to open the electrodes and solder pads, to the latter of which eight Omnetics connectors were soldered. The resulting electrodes had a 1mm diameter and up to 2mm electrode pitch, while the connector paths had a 15 $\mu\text{m}$  width and 30 $\mu\text{m}$  pitch.

In 2010, Kim et al. developed an ultrathin conformal mesh consisting of 30 electrodes for neural recording from the visual cortex (Fig. 2.13(c)) [48]. An electrode mesh was prepared by spin-casting PI on a silicon wafer covered with a polymethyl methacrylate (PMMA) release layer. Electron-beam evaporation was used to create  $\sim 250\mu\text{m}$  wide chromium/gold (Cr/Au) (5/145 nanometre thick) interconnect lines and  $500\mu\text{m} \times 500\mu\text{m}$  contact electrodes, which were later covered with a spin coated 1.2 $\mu\text{m}$  thin PI layer and openings made by RIE. The device was released by dissolving the PMMA layer and transferring the ultrathin device to a bioresorbable silk-film substrate. In the final step, ACF was bonded to the electrode pads to electrically connect the array to the external data-acquisition system. Histology data from related types of devices implanted under the skin exhibited no inflammation after 4 weeks.

In 2015, Márton et al. developed a brain-surface microelectrode array (Fig. 2.13(d)) [49]. The process flow starts with  $\text{SiO}_2$ -layer growth on the Si wafer using wet oxidation, followed by 3.5 $\mu\text{m}$  thick PI layer spin-coating. A 500nm Al layer evaporated on top of the polymer was covered with a 1.8 $\mu\text{m}$  thick spin-coated PR layer. After the lithography step, the pattern is transferred to the aluminium (Al) layer by wet chemical etching of Al. After that, 15nm thick  $\text{TiO}_x$  and 270nm thick Pt layers were sputtered on the whole surface. Following this, a lift-off process removed the PR and Al layers while patterning the  $\text{TiO}_x$ /Pt layer, in the future serving as the conductive layer for the interconnects, electrodes and pads. In the next step, the SU-8 passivation layer (with a final thickness of 12  $\mu\text{m}$ ) was spin-coated and patterned using photolithography so that the electrode sites and pads got exposed. In-vivo recordings were tested in rat brains detecting action potentials of neurons from 8 electrodes for at least 15 weeks.

In 2015, Minev et al. designed an electronic dura mater implant (Fig. 2.13(e)), which integrates a spin-coated silicone substrate (100  $\mu\text{m}$  in thickness), mask-patterned thermally-evaporated stretchable Cr/Au interconnects (5/35 nm in thickness), electrodes coated with a spread and pressed platinum-silicone composite (300  $\mu\text{m}$  in diameter), a compliant fluidic microchannel (100  $\mu\text{m}$  by 50  $\mu\text{m}$  in cross-section), and a spin-coated PDMS passivation layer (20  $\mu\text{m}$  in thickness) [6]. The measured electrode impedance remained constant at 1 kHz upon five weeks of implantation in the rat's spinal cord subdural space.

In 2018, Tybrandt et al. fabricated an 80 $\mu\text{m}$  thick high-density stretchable electrode grid based on gold-coated titanium dioxide nanowires embedded in silicone (Fig. 2.13(f)) [50]. The grid consists of 32 electrodes with a 200 $\mu\text{m}$  pitch patterned by a wax-assisted vacuum-filtration process. The process includes wax printing on top of a polyvinylidene fluoride (PVDF) membrane attached to a paper, so that the pattern desired for the final electrodes is not covered with wax. Conductive nanowires are filtered through the part of the membrane not covered with the wax using vacuum-assisted filtration. During the filtration process, conductive nanowires are deposited on top of the membrane surface. The membrane is dried, and the nanowire pattern is transferred on top of a semi-cured PDMS film, by bringing them in contact and applying pressure. In the end, the membrane is soaked and peeled off from the PDMS surface, while the nanowire pattern stays on the PDMS substrate (more details explained in [51]). After masking the pads with polyethylene naphthalate, the second PDMS layer is spin-coated on top and cured at 80  $^{\circ}\text{C}$  for 16 hours. The grid is intended for chronic recording from the freely-moving-rat cortex surface; the average power of the recorded signals stayed similar after one, two and three months of implantation. 28 out of 32 electrodes showed excellent signal quality after three months of implantation.

In 2019, Jeong et al. fabricated a 25-channel (180 $\mu\text{m}$ -diameter and 500 $\mu\text{m}$ -pitch) LCP-based electrode array fitting the retina (Fig. 2.13(g)) [30]. The fabrication of the array started with the alignment of a 25 $\mu\text{m}$  thick high-melting-temperature LCP (HT-LCP, 310  $^{\circ}\text{C}$ ) on a silicon wafer, followed by

titanium/gold (Ti/Au) (50/100 nm in thickness) seed-layer deposition, PR spin coating and photolithography patterning. After that, 5 $\mu$ m gold was electroplated, and the PR and seed layer were removed. In the end, a 25 $\mu$ m thick low-melting-temperature LCP (LT-LCP, 280 °C) was applied under heat (285 °C) and pressure (1 MPa of load) for 40 mins on top of the stack. The electrodes and pads were opened via laser ablation. Some laser-opened gold electrodes were electrodeposited with an iridium oxide (IrO<sub>x</sub>) layer to improve the properties of the electrodes for stimulation. Interdigitated electrodes (IDE) fabricated using the described process were assessed in an accelerated soak condition in PBS at 87 °C and survived for 158 days.

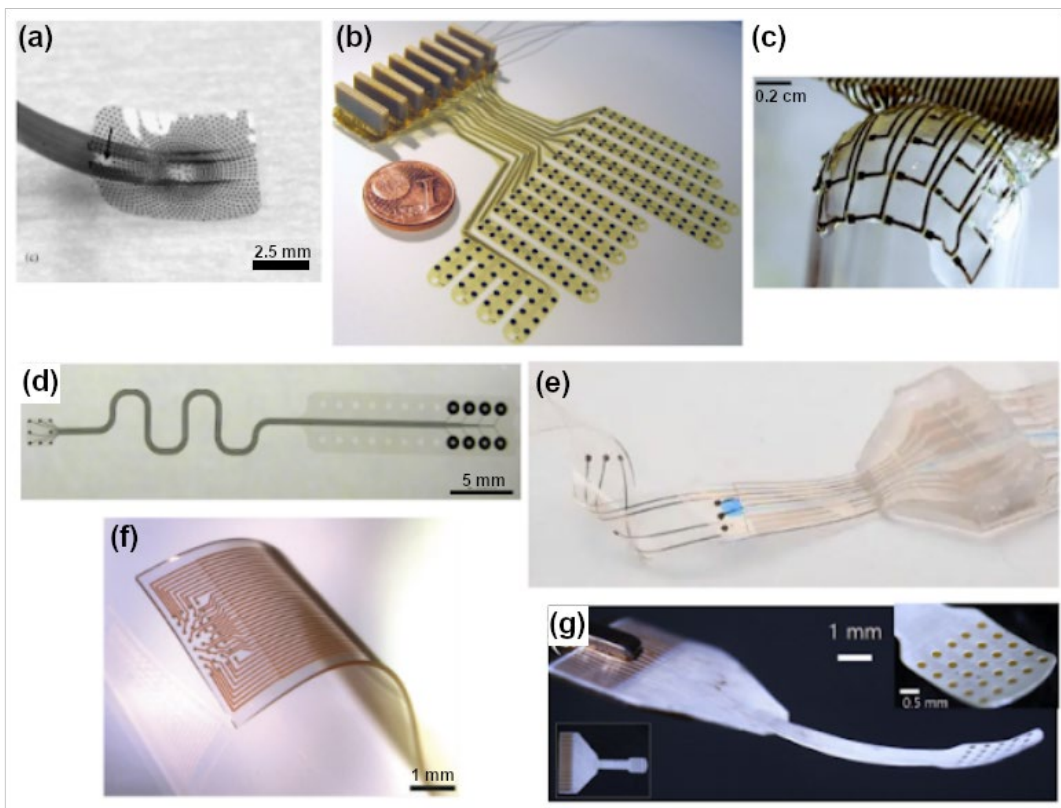


Fig. 2.13. Examples of passive electrode arrays on flexible thin-film substrates. Polymer materials and implantation times of the given examples are as follows: (a) Par C, 6 months [46], (b) PI, 4.5 months [47], (c) PI, 4 weeks [48], (d) SU-8, PI, 15 weeks [49], (e) PDMS, 5 weeks [6], (f) PDMS, 3 months [50], (g) LCP, 158 days at 87 °C PBS [30].

## 2.5 Assembly of electronic components

Several active implants with electronics implanted inside the body exist on the market. In most cases, these electronics are enclosed in rigid titanium cases, which are located at a distant region from the stimulation and recording side of the electrodes. This is not an optimal situation since the connection between an electrode mesh and the electronics is established using leads and cables, which often become the weakest and failing point of the implant and have a limited number of channels due to the feedthrough technology connecting the electronics with the electrode leads and cables. Due to the lack of active implantable electronics, passive electrodes have to be utilized at times. Passive electrode arrays are very restricted in use and are not suitable for long-term implants, since having a passive electrode array means a constantly opened wound that dramatically increases the chance of inflammation and is not convenient for the patient. Therefore, it is desirable to have the electronics implanted inside the body and in close proximity to the stimulating/recording electrodes. Below is a literature review of various techniques used for electronic components integration within the close proximity to the target stimulation/recording region. This review mainly focuses on integrated-circuit (IC) chip-bonding techniques, as well as their bumping technologies, and various adhesive types used to connect the chip to the substrate.

### 2.5.1 Chip-bonding techniques

Various techniques, such as *wire bonding*, *tape automated bonding*, and *flip-chip bonding*, are commonly used for chip integration. As the name suggests, *wire bonding* uses a wire to interconnect the chip to the substrate (Fig. 2.15(a)). Before the wire attachment, the chip must be glued to the substrate, usually using epoxy, silicone, or polyimide. There are three different mechanisms of wire attachment: thermo-compression, ultrasonic, and thermosonic bonding. Thermo-compression (TC) uses temperature and mechanical force, ultrasonic bonding (US) uses ultrasonic energy, and thermosonic (TS) is a combination of both ultrasonic and thermocompression bonding. Since thermocompression bonding uses only force and temperature, it usually requires higher temperatures for bonding (for example, 300 °C and about 1N force for a 80µm wire diameter [52]). During ultrasonic and thermosonic bonding, on the other hand, the ultrasonic

energy has a softening effect on the bump making it susceptible to plastic deformation, therefore requiring lower temperatures and bonding pressure, as well as adding more options for materials. The most common materials used for wire bonding are: Al, copper (Cu), silver (Ag), and Au. To improve the properties of the bonding, these metals are usually alloyed with some other metals. For example, Al is usually alloyed with Au or nickel (Ni) for a higher strength and fine pitch; Ag is usually alloyed with Au, Al and silicon carbide (SiC); Au is used as pure material or alloyed with Al, Cu, or palladium (Pd).

Depending on the bonding method, wire bonding can be divided into *ball-wedge* and *wedge-wedge* bonding. During ball-wedge bonding, the wire is fed through the capillary (visually depicted in Fig. 2.14). The process starts with the formation of the 'ball' at the end of the wire using an electrical spark produced by a high voltage (Fig. 2.14(a)1-2). Then the 'ball' is pressed to the bond pad through TC or TS bonding (Fig. 2.14(a)3). After the first bond is formed, the capillary moves towards the next pad on the substrate and bonds to it using the same bonding energy as the first bond (Fig. 2.14(a)4-6). In the end, the capillary is removed, while the wire is clamped to the substrate (Fig. 2.14(a)7). Ball-wedge wire bonding allows for interconnection with gold wires, usually of about 15/25 $\mu\text{m}$  diameter [53].

As for wedge-wedge bonding, the wire, fed through the bonding tool, is pressed to the bonding surface. Then, US and/or TC energy is applied to form the first 'wedge' bond (Fig. 2.14(b)1-2). After that, the tool is moved towards the substrate pad, and US and/or TC energy is again applied to form the second 'wedge' bond (Fig. 2.14(b)3-4). Ultimately, the bonding tool is raised, and the wire is broken off (Fig. 2.14(b)5).

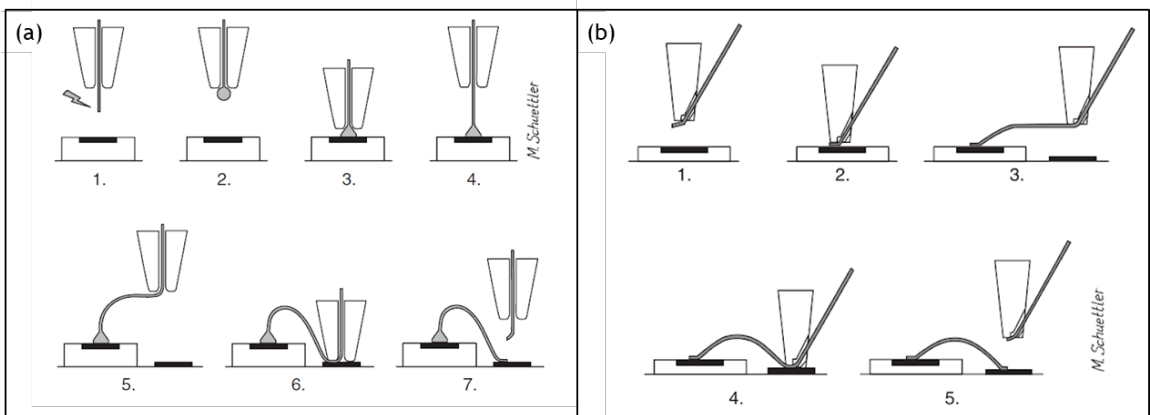
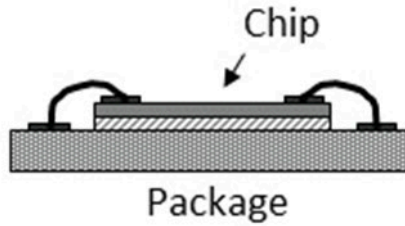
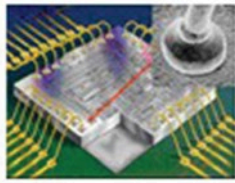




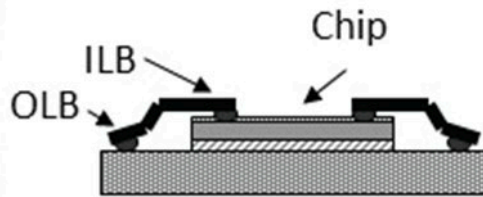
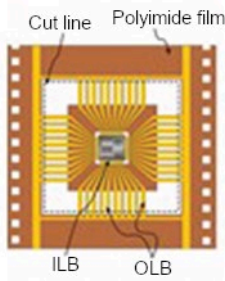
Fig. 2.14. Sketches of ball-wedge (a) and wedge-wedge (b) wire-bonding techniques. Adopted from [54].

During *tape automated bonding*, a bare chip is first attached to a polyimide tape with fine conductor lines. The conductor lines connecting the chip to the tape are called inner lead bonds (ILB), while the lines connecting the tape to the outer circuit are called outer lead bonds (OLB) (Fig.2.15(b)). The conductor lines are usually made of copper, either electrodeposited or attached to the PI tape using adhesives and structured to the required pattern using photolithography. Then this film is moved to the target location, and the leads are cut and soldered to the substrate (Fig. 2.15(b)). The joining of the chip to the substrate is made by means of thermocompression or thermosonic bonding. The bonding temperature depends on the material of the pads and bumps; for example, for a gold-tin (Au/Sn) intermetallic layer, the optimal temperature range lies between 420 and 470 °C [55]. After the chip is bonded, it might be covered with a glob of epoxy or plastic. The advantage of this method is that it is automated and might bond a high volume of chips per unit of time. It is commonly used for bank, SIM, or credit cards and mobile phones. Since the used materials are not biocompatible, this method cannot be used for implantation without full hermetic encapsulation.

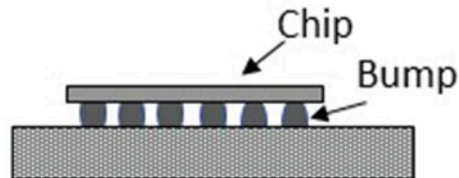
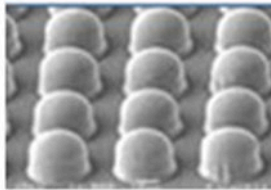
*Flip-chip bonding* is another standard method to interconnect the chip with the substrate. For this, the chip is flipped with the bumps facing down so that the bumps are aligned with the pads on the substrate. Subsequently, the contact between the chip and the substrate is established using underfill (Fig. 2.15 (c)). Soldering the chip bumps to the substrate by reflowing the solder is not always possible since it requires very high temperatures and lead or tin-based solder bumps. When soldering is not possible, interconnection using adhesives has to be implemented. The adhesive is placed on the pads, and the contact is established by thermocompression or thermosonic bonding. The adhesive acts as a glue and establishes either mechanical (in the case of non-conductive adhesives or films (NCA/NCF)) or both mechanical and electrical connections (in the case of anisotropic conductive adhesives or films (ACA/ACF)). Section 2.5.3 describes the different types of adhesives used for the flip-chip bonding process in more detail.



(a) Wire Bonding



(b) Tape Automated Bonding



(c) Flip-Chip Interconnection

Fig. 2.15. Various bonding techniques used for chip interconnection: (a) wire bonding, (b) tape automated bonding, (c) flip-chip interconnection. Reproduced from [56].

## 2.5.2 Bumping technologies

To obtain contact between the flipped chip and the substrate, the chip has to have bumps. The bumping process usually consists of two steps. The first step is under-bump metallization (UBM), which is creating a metal surface that serves as the adhesion as well as the barrier layer to prevent the direct reaction between the usually aluminium input/output pad of the IC (or the Cu or Al trace) and the solder or gold bump. The second step is the deposition of the bump. In some cases, the process is stopped after the first step or the

process consists of the second step only. The first step can be achieved by evaporation, sputtering, electroplating, and electroless techniques. Different existing bumping techniques, such as *stud bumping*, *electroplated bumping*, *solder bumping*, and *electroless nickel/gold (Ni/Au) bumping*, exist to obtain bumps on the ASIC and are described below. It is worth mentioning that every bumping process starts with cleaning the wafer passivation layer from organic residues and oxides to promote better adhesion of the subsequently deposited layer.

The *gold-stud bumping* process starts similarly to the ball-wedge wire-bonding process, where the gold wire fed through the capillary forms a 'ball' by an electrical spark produced by a high voltage (Fig. 2.16(a)). The 'ball' is bonded to the bond pad by applying, depending on the process, a combination of thermal heating, compression force and ultrasonic energy, to let the 'ball' adhere to the bond pad (Fig. 2.16 (b),(c)). After the 'ball' is bonded (Fig. 2.16(d)), the capillary is raised to complete the bonding (Fig. 2.16(e)). The bumps can be flattened by pressing them down right after they have been formed. This is done to obtain bumps of the same height; this method is called coining. The advantage of this method is that it doesn't require UBM, because the gold bumping is done directly on the aluminium pad.

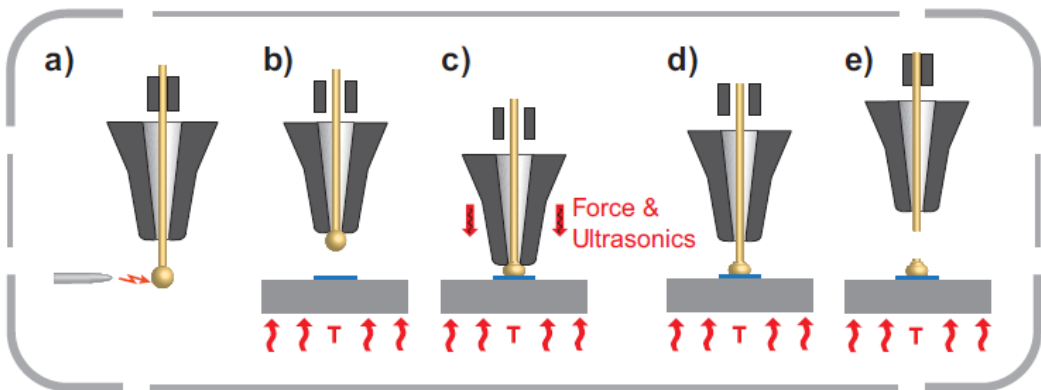


Fig. 2.16. Schematic illustration of the stud bumping process fabricated using thermosonic bonding. Reproduced from [57].

*Electroplated under-bump metallisation (UBM)* technology starts with the sputtering of under-bump layers (TiW/Cu, Cr/Cu, Ni/Au, Ti/Cu/Ni, Al/Cu/Ni, etc.) on top of Al (sometimes Cu) pads (Fig. 2.17(a)). Then photoresist is applied, structured and developed so that the area where copper "stud

bumps"/ "mini-bumps" are supposed to be formed is not covered with the photoresist (Fig. 2.17(b)). After that, a copper or gold layer is electroplated on top of the sputtered layer (Fig. 2.17(c)). The process can be finished with photoresist stripping and UBM-layer etching. In case a *solder bump* is required, the process continues, without the photoresist stripping and UBM-layer etching, such that the second photoresist layer can be applied, structured and developed using a different mask so that the area where we want to form the solder bump is not covered (Fig. 2.17(d)). Pb/Sn solder is electroplated on top of the "mini-bump", while the photoresist layers are stripped and UBM-layer etched (Fig. 2.17(e)). The solder is reflowed to form a spherical solder bump (Fig. 2.17(f)). The UBM layer seals the Al pad and prevents the potential diffusion of the metals to the IC package. It also provides a good bond to the Al pad, which usually oxidises almost immediately.

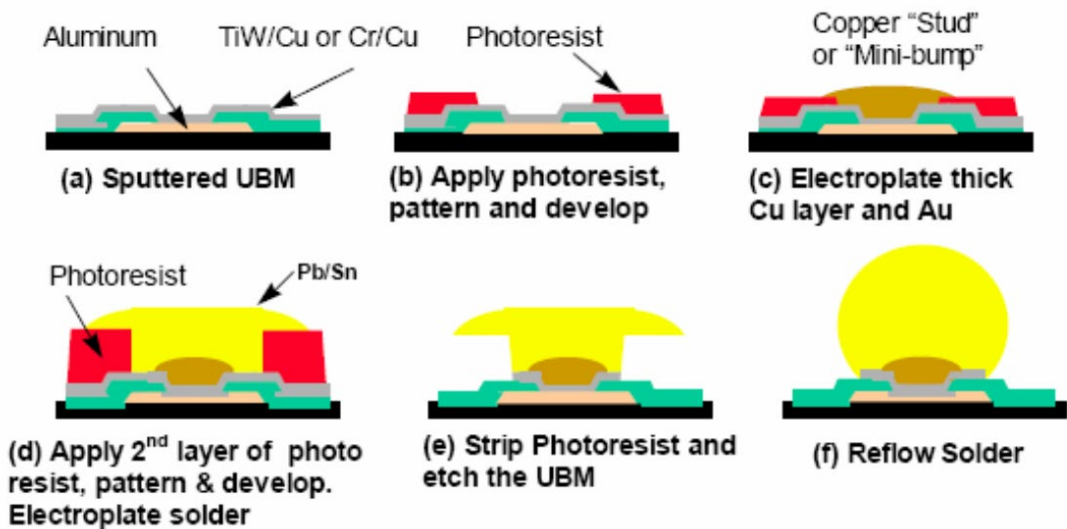


Fig. 2.17. Schematic illustration of the electroplated under-bump metallisation and solder-bump process. Reproduced from [58].

Similarly to solder bumping, a *copper pillar bumping* technology uses electroplating, in this case to create copper pillars on top of the seed (usually copper) layer. The diameter of the pillars is defined by the photoresist, while their height is defined by the electroplating process parameters. A nickel diffusion barrier between the pillar and the solder bump allows to limit the formation of copper-tin intermetallic layer growth and prevents voids

formation. Copper pillar bumping enables high-density designs, in comparison with standard solder bump technology.

*Electroless-Ni/Au bumping* (ENIG) is a low-cost solution, not requiring a lithography step. The process starts with covering the silicon surface to avoid nickel plating on top of it, followed by aluminium cleaning from contamination and removal of the aluminium oxide (Fig. 2.18(a)). After that, a pre-plating process called zincation is used to activate the surface (Fig. 2.18(b)) for further thick-Ni and thin-Au plating (Fig. 2.18(c),(d)). If a solder bump is required, the ENIG-deposited layer can be the foundation for the solder bump. If not, and the Ni/Au layer is sufficient, it serves as a stand-alone bump.

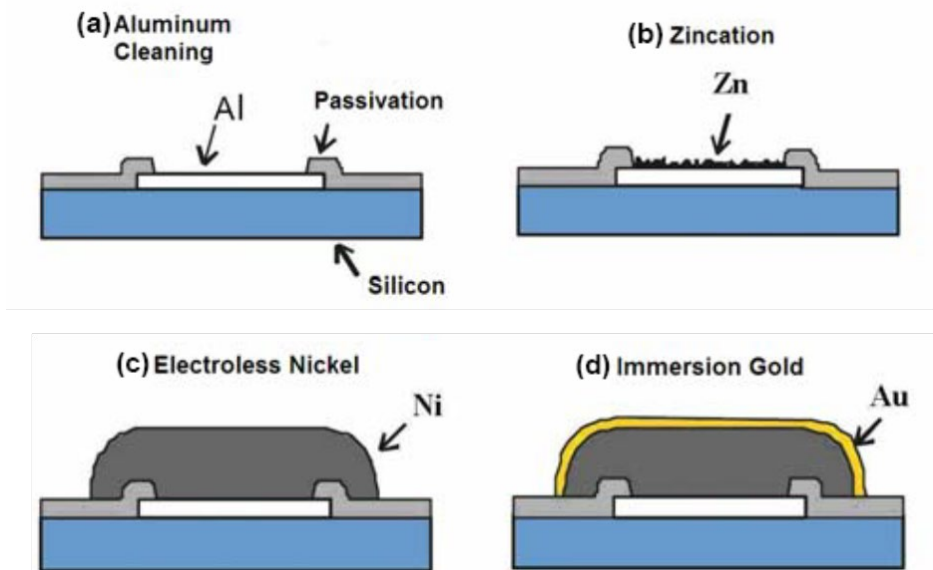


Fig. 2.18. Schematic illustration of the electroless-nickel-immersion-gold (ENIG) bumping process. Reproduced from [58].

When choosing the bump types, we need to understand the limitations of the various bumping technologies. The table below summarizes various parameters that have to be taken into account when choosing the bump type.


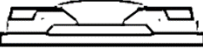
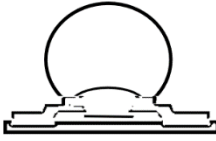
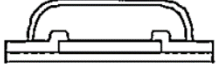
Bump type	stud bump	electroplated bump	solder bump	electroless Ni/Au
Bump schematic				
Bump material	Au	Ni, Au, Cu, CuSn or AuSn	PbSn	Ni base, Au finish
Bump height	20-80 $\mu\text{m}$	2-25 $\mu\text{m}$	15-150 $\mu\text{m}$	1-8 $\mu\text{m}$ Ni, 0.05-0.25 $\mu\text{m}$ Au

Table 2.2. Comparative table of the different types of bumps with their properties.

### 2.5.3 Adhesive types

Different types of adhesives are used to facilitate chip bonding, mechanically fixate the chip, and ensure the stability of the connection during the flip-chip bonding process. These adhesives usually require 140 °C to 180 °C processing temperatures and can be divided into two groups: conductive and non-conductive adhesives. Conductive adhesives include: isotropic conductive adhesives (ICAs), anisotropic conductive adhesives ACAs, anisotropic conductive films (ACFs). Non-conductive adhesives include: non-conductive adhesives NCAs and non-conductive films NCFs.

ICAs and ACAs are adhesives with conductive filler particles dispersed in a polymeric resin. Conductive fillers include metal-based fillers (which use 2-3 $\mu\text{m}$ -diameter Ag, Ni, Au or Cu particles) or carbon-based fillers [59], [60] (which use carbon nanotubes, graphene, etc.). Epoxy [61], silicone [62], polyurethane [63], polyvinyl acetate (PVA) [64] and polyvinyl chloride (PVC) [65] can serve as insulating polymeric resins. The performance of the adhesive will depend on these materials and their concentration, as well as the interaction between the filler particles and processing conditions of composite preparation. In ICAs, the volume fraction of the filler conductive particles is high enough to conduct current in all directions; therefore, they need to be applied locally on the bumps, to ensure that the spreading of the ICA doesn't happen, since it could lead to shorts (Fig. 2.19(a)). There are different ways to apply ICA to the bumps; the most common ones are using screen or stencil printing or a transfer method is used. The transfer method

is common for fine-precision flip-chip bonding. This method requires raised bumps, which are brought in contact with a flat layer of ICA (which can be prepared via screen printing); after the ICA is on the bumps, the chip is brought in contact with its corresponding tracks on the substrate and cured [66]. This method doesn't require the application of pressure. After curing, the space between the chip and the substrate is filled with an underfill material to improve the stability and reliability of the bond. As for the ACAs, the amount of conductive filler particles is below percolation threshold, so that they only conduct in the vertical direction, when the particles are brought mechanically together. This allows to establish connection between the bump and the corresponding conductive track, and isolate it from neighbouring electrodes (Fig. 2.19(b)). Usually, ACA is applied by dispensing a line/drop of adhesive on top of the substrate surface, covering at once the entire bond area. After that, to establish the contact, pressure, heat, and sometimes UV must be applied. ACFs work by a similar principle as ACAs, but ACFs are sourced in the form of films. First ACF should be attached to the cleaned substrate surface (for example by means of a film liner, which is removed after attaching the ACF to the substrate). Then, by applying thermocompression, the chip is being fixed to the substrate.

NCA and NCF are alternatives to ACAs and ACFs, which can be used for fine pitches (about 30  $\mu\text{m}$  or less). ACAs are not suitable for fine-pitch applications because, when the distance between the pads is very small, the conductive particles of ACA might accumulate so that they will create a short circuit. In the case of NCA and NCF, direct physical contact between the chip's bump and the substrate pad is established by applying high pressure and temperature (Fig. 2.19(c)), while the NCA serves just as a non-conductive glue to keep the chip on the substrate. NCA are most commonly thermosetting epoxy-based or acrylic-based.

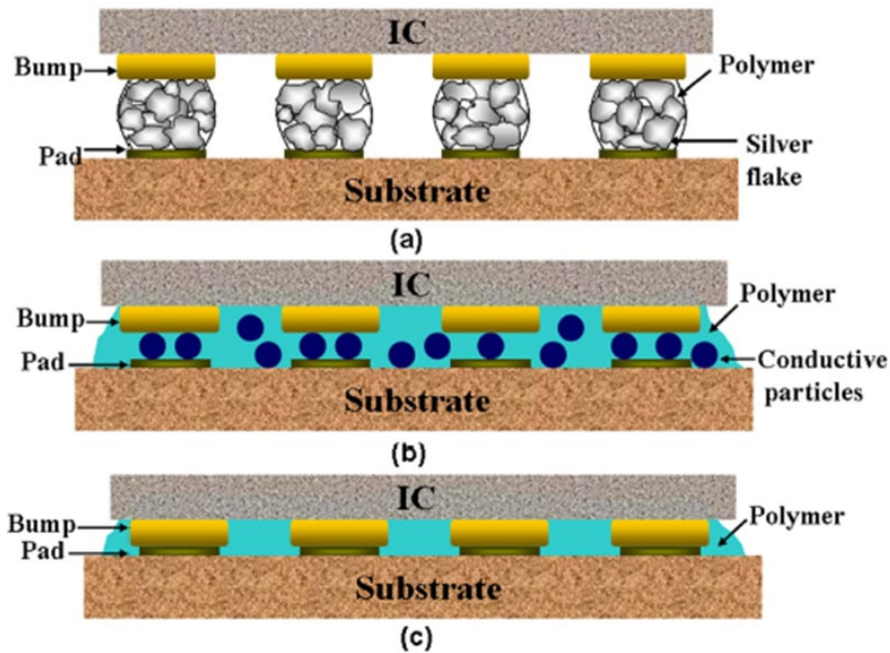


Fig. 2.19. Schematic illustration of different adhesive types: isotropic conductive adhesive (a), anisotropic conductive adhesive (b), and non-conductive adhesive (c). Reproduced from [67].

## 2.6 Active polymer-based implants

The literature review presented below outlines different approaches taken by scientists to integrate electronics into passive polymer-based neural implants and create a miniaturised, wirelessly communicating active implants.

In 2004, Stieglitz et al. [68] developed an inductively coupled epiretinal visual prosthesis (Fig. 2.20(a)). The prosthesis consists of a flexible PI substrate with 24 electrodes, interconnection gold paths, and connection pads for electronic components. The electronics and components include a receiver part consisting of an inductive coil, a diode for rectification of the signal and a capacitor for charge storage. All these components were fixed and electrically contacted to the substrate by hand. The receiver and stimulator chips for decoding the data and driving the electrodes were assembled with the "Microflex interconnection" technique [69]. This technique electrically and mechanically connects the PI substrate with the via holes to the chip.



Gold stud balls go through the via holes located in the middle of the connection pads of the PI substrate and connect it to the chip by applying temperature, force, and ultrasonic energy (described in [69]). The device was fully covered with ParC first and then with a PDMS layer. Results from chronic implantation in cats demonstrated biostability and successful local cortical activation.

In 2005, Okabe et al. [70] developed a technique for packaging a flexible antenna and a CMOS rectifier chip for small-size brain-implantable devices (Fig. 2.20(b)). The proposed device consists of a flexible antenna with a small inductance, a rectifier chip with the on-chip transformer matching the impedance between the antenna and the rectifier, and electrodes, all embedded in Parylene-C flexible film. The silicon chip (2.5x2.5x0.4 mm) was connected to the antenna by flip-chip bonding using anisotropic conductive paste (TAP0402E) containing 2 $\mu$ m diameter nickel particles. The bonding conditions, such as temperature, time and pressure, were as follows: 100 °C, 3 minutes, pressure not given. A 5 $\mu$ m thick parylene film served as the device's substrate and coating material.

In 2018, Park et al. [71] developed a fully-implantable optoelectronic system for wireless optogenetics (Fig. 2.20(c)). The system consists of an RF harvesting unit for receiving and rectifying the signal from a transmitter, multiplying the voltages and routing the resulting direct-current output to the LED. It also includes antennas and LEDs connected with the Ti/Au interconnects. The LED and the chips were placed to the pads on a PI substrate with a solder paste (SMD290SNL250T5, Chipquik), and then the substrate was cured in a vacuum oven for 10 minutes at 250 °C. The whole system is encapsulated in 3 $\mu$ m thick PI and 100 $\mu$ m thick PDMS on top. The developed devices are capable of optogenetic stimulation of peripheral nerves and the spinal cord.

In 2019, Neuralink [15] published a pre-print describing a brain-machine interface (BMI) with a high channel count and single-spike resolution for testing in rodents. The system consisted of ultra-fine polyimide-based gold-electrode probes with PEDOT:PSS and IrOx electrode sites treatments, electronics encapsulated in a titanium package and a USB-C connector for power and data transfer. The electronics included ASICs with 256 programmable amplifiers each, on-chip analogue-to-digital converters and

peripheral control circuitry to serialise the digitised outputs, all enclosed in a titanium package. The ASICs were flip-chip bonded to a PCB. Later the system was improved with a wireless Bluetooth communication link and a battery. The system wirelessly records and streams action potentials from 1024 channels from the somatosensory neurons of a pig (Fig. 2.20(d)). The motor-cortical brain-machine interface was presented to the public in their last demo release. The system is intended to predict and control the cursor's movement by the device implanted in the monkey cortex. Not many details regarding the electronics within the device were shared in their demo show and on the website.

In 2019, Yun et al. [72] developed a fully-implantable wirelessly-controlled neurostimulator (Fig. 2.20(e)). The array consists of a cortical surface array for making rats change their moving direction, a depth electrode array for providing rewards, a battery and ZigBee telemetry, all of which were encapsulated in LCP and assembled using customised flat cables and connectors. Electronic components, such as the stimulation-pulse generator, the power-receiving coil for wireless communication, the battery, and the power-management unit, were all mounted on an FR-4 PCB. The assembled board, together with a feedthrough board plugged into an onboard connector, were placed between two 500- $\mu\text{m}$  thick LCP films. The assembly process was followed by a 3D thermoforming process pressing on the perimeter of the LCP package at 295 °C for 10 min with a 2 kg/cm<sup>2</sup> load. The device was implanted in rats and induced them to turn right (or left).

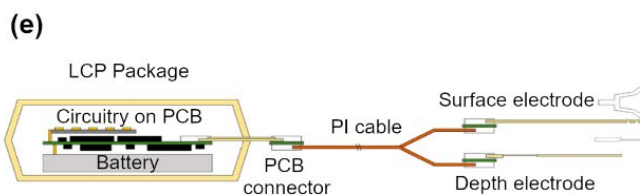
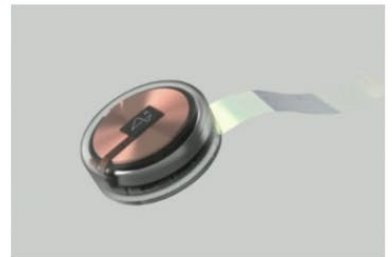
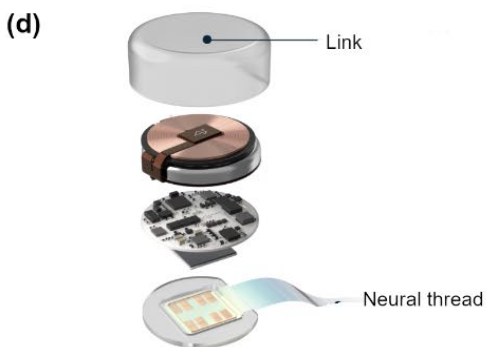
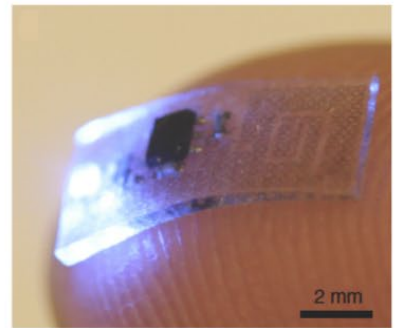
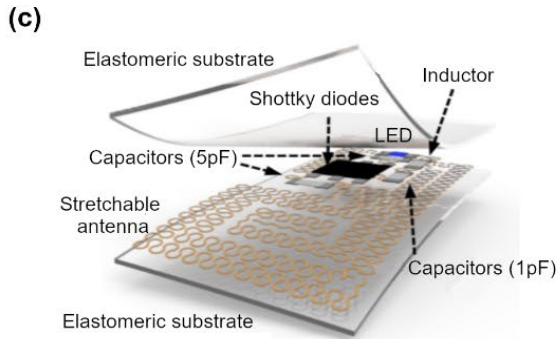
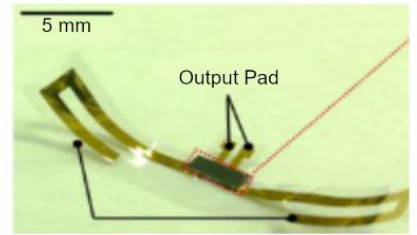
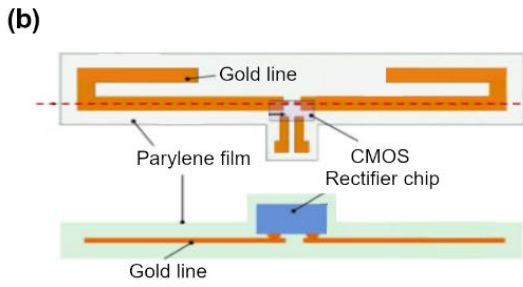
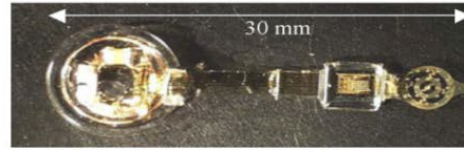
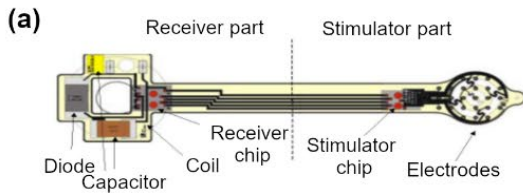


Fig. 2.20. Examples of active electrode arrays with the schematics on the left side and the photo illustration on the right: (a) PI-based epiretinal visual prosthesis [68], (b) ParC embedded flexible antenna with a rectifier chip for wireless power transmission [70], (c) PDMS-based optogenetic system for wireless optogenetics [71], (d) Neuralink's brain-machine interface for wireless recording and streaming of action potentials [73], (e) Wirelessly-controlled neural stimulator [72].

## 2.7 Conclusion

Most polymer-based passive electrode arrays made of ParC, polyimide, and PDMS are deposited in a layer-to-layer fashion using chemical vapour deposition (CVD) or spin coating (examples in Section 2.4). Because of this layer-to-layer deposition, these polymers face the problem of poor adhesion and delamination at the polymer-polymer interface (examples shown in Figures 2.10-2.11 of Section 2.3). Several strategies, such as plasma and corona-discharge pre-treatment [39], annealing [74], use of adhesion promoters [40], interlayers [75], and partial curing [76], are used to improve the self-adhesion of these polymers.

Nevertheless, the interface always remains and is considered a critical point of failure for the active implant's continuous, long-term stable performance inside the aqueous body environment [44]. As seen from Figures 2.12(a),(b), using thermoplastic polymers, such as LCP and TPU, and applying an optimally chosen temperature and force, the problem of polymer-polymer interface delamination or poor adhesion can be prevented due to the possibility of a complete merging of the polymer layers within each other. Therefore, in the next two chapters (Chapter 3 and Chapter 4), examples of using thermoplastic LCP- and TPU-based neural interfaces will be presented.

## References

- [1] A. Carnicer-Lombarte, S. T. Chen, G. G. Malliaras, and D. G. Barone, "Foreign Body Reaction to Implanted Biomaterials and Its Impact in Nerve Neuroprosthetics," *Frontiers in Bioengineering and Biotechnology*, vol. 9. Frontiers Media S.A., Apr. 15, 2021. doi: 10.3389/fbioe.2021.622524.

- [2] United States Pharmacopeial Convention, *The United States Pharmacopeia: USP 23; The National Formulary: NF 18*, vol. 3. United States pharmacopeial convention, 1995.
- [3] "ISO 10993-1:2018 Biological evaluation of medical devices – Part 1: Evaluation and testing within a risk management process," 2018.
- [4] D. W. Grainger, "The Williams Dictionary of Biomaterials." [Online]. Available: [www.elsevier.com](http://www.elsevier.com) or [www.elsevier.nl](http://www.elsevier.nl).
- [5] A. Carnicer-Lombarte *et al.*, "Mechanical matching of implant to host minimises foreign body reaction," *Bioarxiv*, pp. 1–41, Nov. 2019, doi: 10.1101/829648.
- [6] Ivan R. Minev *et al.*, "Electronic dura mater for long-term multimodal neural interfaces," *Science*, vol. 347, no. 6218, pp. 154–159, Jan. 2015, doi: 10.1126/science.1260960.
- [7] C. T. McKee, J. A. Last, P. Russell, and C. J. Murphy, "Indentation versus tensile measurements of young's modulus for soft biological tissues," *Tissue Eng Part B Rev*, vol. 17, no. 3, pp. 155–164, Jun. 2011, doi: 10.1089/ten.teb.2010.0520.
- [8] A. J. T. Teo, A. Mishra, I. Park, Y. J. Kim, W. T. Park, and Y. J. Yoon, "Polymeric Biomaterials for Medical Implants and Devices," *ACS Biomater Sci Eng*, vol. 2, no. 4, pp. 454–472, 2016, doi: 10.1021/acsbiomaterials.5b00429.
- [9] C. Kallmayer, J. Haberland, F. Schaller, F. Kayatz, T. Löher, and A. Schult, "Optimized Thermoforming Process for Conformable Electronics."
- [10] C. Hassler, T. Boretius, and T. Stieglitz, "Polymers for neural implants," *J Polym Sci B Polym Phys*, vol. 49, no. 1, pp. 18–33, 2011, doi: 10.1002/polb.22169.
- [11] J. Y. Rho, R. B. Ashman, and C. H. Turner, "YOUNG'S MODULUS OF TRABECULAR AND CORTICAL BONE MATERIAL: ULTRASONIC AND MICROTENSILE MEASUREMENTS\*," 1993.
- [12] H. E. Pearse, "RESULTS FROM USING VITALLIUM TUBES IN BILIARY SURGERY\* FROM THE DEPARTMENT OF SURGERY, SCHOOL OF MEDICINE AND DENTISTRY, UNIVERSITY OF."
- [13] A. Colas and J. Curtis, "Silicone Biomaterials: History and Chemistry & Medical Applications of Silicones." [Online]. Available: [www.books.elsevier.com/bioengineering](http://www.books.elsevier.com/bioengineering)
- [14] A. P. Finn, D. S. Grewal, and L. Vajzovic, "Argus II retinal prosthesis system: A review of patient selection criteria, surgical considerations, and post-

- operative outcomes," *Clinical Ophthalmology*, vol. 12. Dove Medical Press Ltd, pp. 1089–1097, Jun. 13, 2018. doi: 10.2147/OPHTH.S137525.
- [15] E. Musk, "An integrated brain-machine interface platform with thousands of channels," *J Med Internet Res*, vol. 21, no. 10, Oct. 2019, doi: 10.2196/16194.
- [16] H. Xu, A. W. Hirschberg, K. Scholten, T. W. Berger, D. Song, and E. Meng, "Acute in vivo testing of a conformal polymer microelectrode array for multi-region hippocampal recordings," *J Neural Eng*, vol. 15, no. 1, Feb. 2018, doi: 10.1088/1741-2552/aa9451.
- [17] IEEE Staff, *2017 19th International Conference on Solid State Sensors, Actuators and Microsystems (TRANSDUCERS)*. IEEE, 2017.
- [18] S. Kuppusami and R. H. Oskouei, "Parylene Coatings in Medical Devices and Implants : A Review," vol. 3, no. 2, pp. 9–14, 2015, doi: 10.13189/ujbe.2015.030201.
- [19] B. J. Kim, B. Chen, M. Gupta, and E. Meng, "Formation of three-dimensional Parylene C structures via thermoforming," *Journal of Micromechanics and Microengineering*, vol. 24, no. 6, Jun. 2014, doi: 10.1088/0960-1317/24/6/065003.
- [20] T. Hentschel and H. Münstedl, "Thermoplastic polyurethane - The material used for the Erlanger silver catheter," *Infection*, vol. 27, no. SUPPL. 1, pp. 43–45, 1999, doi: 10.1007/BF02561617.
- [21] P. Volkow *et al.*, "Polyurethane II catheter as long-indwelling intravenous catheter in patients with cancer," *Am J Infect Control*, vol. 31, no. 7, pp. 392–396, 2003, doi: 10.1067/mic.2003.39.
- [22] M. Wildgruber *et al.*, "Polyurethane versus silicone catheters for central venous port devices implanted at the forearm," *Eur J Cancer*, vol. 59, pp. 113–124, 2016, doi: 10.1016/j.ejca.2016.02.011.
- [23] J. P. Theron *et al.*, "Modification, crosslinking and reactive electrospinning of a thermoplastic medical polyurethane for vascular graft applications," *Acta Biomater*, vol. 6, no. 7, pp. 2434–2447, 2010, doi: 10.1016/j.actbio.2010.01.013.
- [24] Y. S. Choi *et al.*, "Stretchable, dynamic covalent polymers for soft, long-lived bioresorbable electronic stimulators designed to facilitate neuromuscular regeneration," *Nat Commun*, vol. 11, no. 1, pp. 1–14, Nov. 2020, doi: 10.1038/s41467-020-19660-6.
- [25] P. Kasprzyk and J. Datta, "Novel bio-based thermoplastic poly(ether-urethane)s. Correlations between the structure, processing and properties,"

- Polymer (Guildf)*, vol. 160, pp. 1–10, Jan. 2019, doi: 10.1016/j.polymer.2018.11.032.
- [26] J. Jeong, S. H. Bae, J. Seo, H. Chung, and S. J. Kim, "Long-term evaluation of a liquid crystal polymer (LCP) -based retinal prosthesis," *J. Neural Eng.*, vol. 13, no. 2, p. 25004, Feb. 2016, doi: 10.1088/1741-2560/13/2/025004.
- [27] K. Ramesh, A. Sivaramanarayanan, "An Overview of the Plastic Material Selection Process for Medical Devices," *Hcl*, no. February, p. 8, 2013, [Online]. Available: [https://www.hcltech.com/sites/default/files/an\\_overview\\_of\\_the\\_plastic\\_material\\_selection\\_process\\_for\\_medical\\_devices.pdf](https://www.hcltech.com/sites/default/files/an_overview_of_the_plastic_material_selection_process_for_medical_devices.pdf)
- [28] S. W. Lee, K. S. Min, J. Jeong, J. Kim, and S. J. Kim, "Monolithic encapsulation of implantable neuroprosthetic devices using liquid crystal polymers," *IEEE Trans Biomed Eng.*, vol. 58, no. 8, pp. 2255–2263, Aug. 2011, doi: 10.1109/TBME.2011.2136341.
- [29] G. T. Hwang *et al.*, "In vivo silicon-based flexible radio frequency integrated circuits monolithically encapsulated with biocompatible liquid crystal polymers," *ACS Nano*, vol. 7, no. 5, pp. 4545–4553, May 2013, doi: 10.1021/nn401246y.
- [30] J. Jeong, K. S. Min, and S. J. Kim, "Microfabrication process for long-term reliable neural electrode arrays using liquid crystal polymer (LCP)," *Microelectron Eng.*, vol. 216, p. 111096, Aug. 2019, doi: 10.1016/j.mee.2019.111096.
- [31] K. Scholten and E. Meng, "Materials for microfabricated implantable devices: A review," *Lab on a Chip*, vol. 15, no. 22. Royal Society of Chemistry, pp. 4256–4272, 2015. doi: 10.1039/c5lc00809c.
- [32] "Product Information Platilon ® U Highly Elastic Polyurethane Films."
- [33] "LCP-027\_VectraLCPDesignGuideTG\_AM\_0613 data sheet".
- [34] Speciality Coating Systems, "SCS Parylene Properties [Data sheet]," 2018. Accessed: Jul. 17, 2023. [Online]. Available: <https://scscoatings.com/technical-library/>
- [35] J. J. Licari, *Coating materials for electronic applications: polymers, processes, reliability, testing*. Noyes Publications, 2003.
- [36] D. Schaubroeck, R. Verplancke, M. Cauwe, D. Cuypers, and K. Baumans, "Polyimide-ALD-polyimide layers as hermetic encapsulant for implants," *XXXI Int Conf on Surf Mod Tech*, pp. 1–6, Jul. 2017.

- [37] A. Pak *et al.*, "Thin Film Encapsulation for LCP-Based Flexible Bioelectronic Implants : Comparison of Different Coating Materials Using Test Methodologies for Life-Time Estimation," 2022.
- [38] A. Vanhoestenbergh and N. Donaldson, "Corrosion of silicon integrated circuits and lifetime predictions in implantable electronic devices," *J Neural Eng*, vol. 10, no. 3, May 2013, doi: 10.1088/1741-2560/10/3/031002.
- [39] C. Yang, W. Wang, and Z. Li, "Optimization of Corona-triggered PDMS-PDMS Bonding Method," pp. 319–322, Jan. 2009, doi: 10.1109/NEMS.2009.5068586.
- [40] K. Koh, J. Chin, J. Chia, and C. Chiang, "Quantitative Studies on PDMS-PDMS Interface Bonding with Piranha Solution and its Swelling Effect," *Micromachines (Basel)*, vol. 3, no. 2, pp. 427–441, May 2012, doi: 10.3390/mi3020427.
- [41] S. Metz, R. Holzer, and P. Renaud, "Polyimide-based microfluidic devices," pp. 29–34, 2001, doi: 10.1039/b103896f.
- [42] M. Tintelott and A. Schander, "Understanding Electrical Failure of Polyimide-Based Flexible Neural Implants : The Role of Thin Film Adhesion," *Polymers (Basel)*, vol. 14, no. 18, pp. 1–11, Sep. 2022, doi: 10.3390/polym14183702.
- [43] A. Ramachandran, M. Junk, K. P. Koch, and K. P. Hoffmann, "A study of parylene C polymer deposition inside microscale gaps," *IEEE Transactions on Advanced Packaging*, vol. 30, no. 4, pp. 712–724, 2007, doi: 10.1109/TADVP.2007.901662.
- [44] J. Ortigoza-Diaz *et al.*, "Techniques and considerations in the microfabrication of parylene c microelectromechanical systems," *Micromachines (Basel)*, vol. 9, no. 9, pp. 1–25, Jul. 2018, doi: 10.3390/mi9090422.
- [45] "Processing of TPU by Extrusion and Special Processes Contents."
- [46] D. C. Rodger *et al.*, "Flexible parylene-based multielectrode array technology for high-density neural stimulation and recording," *Sens Actuators B Chem*, vol. 132, no. 2, pp. 449–460, Jun. 2008, doi: 10.1016/j.snb.2007.10.069.
- [47] B. Rubehn, C. Bosman, R. Oostenveld, P. Fries, and T. Stieglitz, "A MEMS-based flexible multichannel ECoG-electrode array," *J Neural Eng*, vol. 6, no. 3, 2009, doi: 10.1088/1741-2560/6/3/036003.
- [48] D. H. Kim *et al.*, "Dissolvable films of silk fibroin for ultrathin conformal bio-integrated electronics," *Nat Mater*, vol. 9, no. 6, pp. 511–517, 2010, doi: 10.1038/nmat2745.



- [49] G. Márton, G. Orbán, M. Kiss, R. Fiáth, A. Pongrácz, and I. Ulbert, "A multimodal, SU-8 - Platinum - Polyimide microelectrode array for chronic in vivo neurophysiology," *PLoS One*, vol. 10, no. 12, Dec. 2015, doi: 10.1371/journal.pone.0145307.
- [50] K. Tybrandt *et al.*, "High-Density Stretchable Electrode Grids for Chronic Neural Recording," *Advanced Materials*, vol. 30, no. 15, Apr. 2018, doi: 10.1002/adma.201706520.
- [51] K. Tybrandt and J. Vörös, "Fast and Efficient Fabrication of Intrinsically Stretchable Multilayer Circuit Boards by Wax Pattern Assisted Filtration," *Small*, vol. 12, no. 2, pp. 180–184, Jan. 2016, doi: 10.1002/sml.201502849.
- [52] M. R. Lim *et al.*, "The optimization of ultrasonic power and bonding time for thermosonic flip chip bonding," *AIP Conf Proc*, vol. 2045, no. 1, p. 20094, Dec. 2018, doi: 10.1063/1.5080907.
- [53] Y. B. Gianchandani, O. Tabata, and H. Zappe, *Comprehensive Microsystems*, vol. 1. ELSEVIER, 2007.
- [54] A. Inmann and D. Hodgins, *Implantable sensor systems for medical applications*. WOODHEAD PUBLISHING, 2013.
- [55] J. K. L. Lai, M. C. Loo, and K. Y. Cheng, "Effects of Bond Temperature and Pressure on Microstructures of Tape Automated Bonding (TAB) Inner Lead Bonds (ILB) with Thin Tape Metallization," *1995 Proceedings. 45th Electronic Components and Technology Conference*, pp. 819–826, 1995, doi: 10.1109/ECTC.1995.517782.
- [56] M. Datta, "Manufacturing processes for fabrication of flip-chip micro-bumps used in microelectronic packaging: An overview," *Journal of Micromanufacturing*, vol. 3, no. 1, pp. 69–83, Dec. 2019, doi: 10.1177/2516598419880124.
- [57] F. Wennergren, "Metal Filling of Through Silicon Vias (TSVs) using Wire Bonding Technology [Master Thesis]," KTH School of Information and Communication Technology, 2014.
- [58] M. K. Md Arshad, U. Hashim, and M. Isa, "Under bump metallurgy (UBM) - A technology review for flip chip packaging," *International Journal of Mechanical and Materials Engineering*, vol. 2, no. 1, pp. 48–54, Jan. 2007.
- [59] Z. Czech *et al.*, "Using of carbon nanotubes and nano carbon black for electrical conductivity adjustment of pressure-sensitive adhesives," *Int J Adhes Adhes*, vol. 36, pp. 20–24, Jul. 2012, doi: 10.1016/j.ijadhadh.2012.04.004.

- [60] "The Application of Nano Carbon Based Materials in Electrical Conductive Adhesives".
- [61] R. Aradhana, S. Mohanty, and S. K. Nayak, "A review on epoxy-based electrically conductive adhesives," *Int J Adhes Adhes*, vol. 99, Jun. 2020, doi: 10.1016/j.ijadhadh.2020.102596.
- [62] Z. Li, K. Hansen, Y. Yao, Y. Ma, K. S. Moon, and C. P. Wong, "The conduction development mechanism of silicone-based electrically conductive adhesives," *J Mater Chem C Mater*, vol. 1, no. 28, pp. 4368–4374, Jul. 2013, doi: 10.1039/c3tc30612g.
- [63] Z. Li *et al.*, "Highly conductive, flexible, polyurethane-based adhesives for flexible and printed electronics," *Adv Funct Mater*, vol. 23, no. 11, pp. 1459–1465, Mar. 2013, doi: 10.1002/adfm.201202249.
- [64] R. Taherian and Z. Samiei, "Investigation on electrical properties of polyvinyl acetate/graphite adhesive by joule heating and hall effect tests," *Mater Today Commun*, vol. 26, Mar. 2021, doi: 10.1016/j.mtcomm.2020.101680.
- [65] L. A. Miranda Yañez, R. Patiño-Herrera, R. Catarino-Centeno, E. E. Silva, L. A. Alcaraz Caracheo, and E. Pérez, "Improving the bond strength of a new polyvinyl chloride (PVC) -based adhesive," *Int J Adhes Adhes*, vol. 127, Oct. 2023, doi: 10.1016/j.ijadhadh.2023.103500.
- [66] Y. Li and C. P. Wong, "Recent advances of conductive adhesives as a lead-free alternative in electronic packaging: Materials, processing, reliability and applications," *Materials Science and Engineering R: Reports*, vol. 51, no. 1–3, pp. 1–35, Jan. 30, 2006. doi: 10.1016/j.mser.2006.01.001.
- [67] Zhang Rongwei, Agar C. Josh, and Wong C.P., "Recent Advances on Electrically Conductive Adhesives," no. c, pp. 696–704, Dec. 2010, doi: 10.1109/EPTC.2010.5702728.
- [68] T. Stieglitz, "Biomedical microimplants for sensory and motor neuroprostheses," *Proceedings - IEEE International Symposium on Circuits and Systems*, pp. 2189–2192, 2006, doi: 10.1109/iscas.2006.1693053.
- [69] J.-U. Meyer, T. Stieglitz, O. Scholz, W. Haberer, and H. Beutel, "High Density Interconnects and Flexible Hybrid Assemblies for Active Biomedical Implants," 2001.
- [70] K. Okabe, H. P. Jeewan, S. Yamagiwa, T. Kawano, M. Ishida, and I. Akita, "Co-design method and wafer-level packaging technique of thin-film flexible antenna and silicon CMOS rectifier chips for wireless-powered neural

interface systems," *Sensors (Switzerland)*, vol. 15, no. 12, pp. 31821–31832, 2015, doi: 10.3390/s151229885.

- [71] S. Il Park *et al.*, "Soft, stretchable, fully implantable miniaturized optoelectronic systems for wireless optogenetics," *Nat Biotechnol*, vol. 33, no. 12, pp. 1280–1286, Dec. 2015, doi: 10.1038/nbt.3415.
- [72] S. Yun *et al.*, "Remote-controlled fully implantable neural stimulator for freely moving small animal," *Electronics (Switzerland)*, vol. 8, no. 6, Jun. 2019, doi: 10.3390/electronics8060706.
- [73] E. Strickland, "Exclusive Q&A: Neuralink's Quest to Beat the Speed of Type," <https://spectrum.ieee.org/elon-musk-brain-neuralink>.
- [74] R. P. Von Metzen and T. Stieglitz, "The effects of annealing on mechanical , chemical , and physical properties and structural stability of Parylene C," *Biomed Microdevices*, vol. 15, pp. 727–735, Mar. 2013, doi: 10.1007/s10544-013-9758-8.
- [75] J. S. Ordonez, C. Boehler, M. Schuettler, and T. Stieglitz, "Improved polyimide thin-film electrodes for neural implants," *2012 Annual International Conference of the IEEE Engineering in Medicine and Biology Society*, pp. 5134–5137, Sep. 2012, doi: 10.1109/EMBC.2012.6347149.
- [76] M. A. Eddings, M. A. Johnson, and B. K. Gale, "Determining the optimal PDMS-PDMS bonding technique for microfluidic devices," *Journal of Micromechanics and Microengineering*, vol. 18, no. 6, pp. 1–4, Apr. 2008, doi: 10.1088/0960-1317/18/6/067001.
- [77] A. T. Al-Halhouli, I. Kampen, T. Krah, and S. Büttgenbach, "Nanoindentation testing of SU-8 photoresist mechanical properties," *Microelectron Eng*, vol. 85, no. 5–6, pp. 942–944, May 2008, doi: 10.1016/j.mee.2008.01.033.

# 3

## Thin film encapsulation for LCP-based flexible bioelectronic implants

### 3.1. Introduction

As mentioned in Chapter 2, flexible substrates such as PI, ParC, LCP, and silicone elastomers have been used in neural implants as substrates for electronic components and metal interconnects. Passive electrode arrays are usually tethered to an external unit that holds the electronics used for stimulation and/or recording [1]–[2]. This often renders the device suitable only for short-term studies. Moving towards fully-implantable, biocompatible, yet flexible, active implants (generic realisation example shown in Fig. 3.1.) requires a tailored packaging approach.

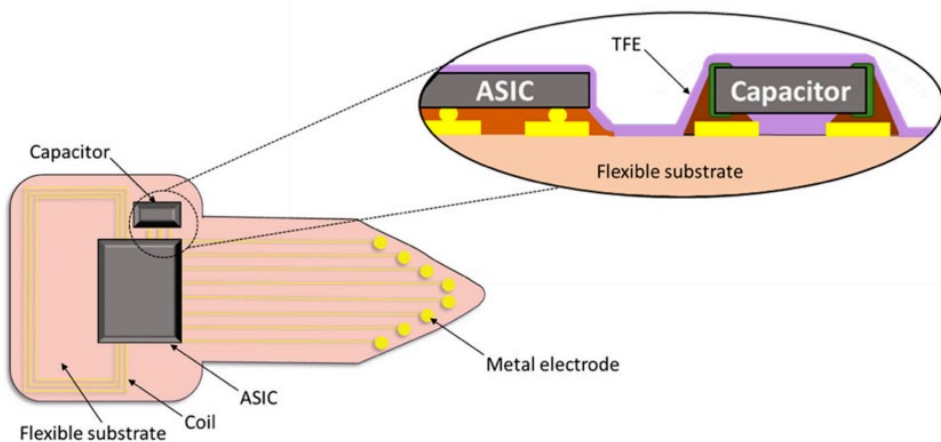


Fig. 3.1. Generic sketch of a wirelessly-powered, fully-implantable active device based on a polymer substrate: electronic components in the form of a capacitor and ASIC constituting the functional circuit; metal electrodes for

delivering or receiving signals to/from the tissue; coil for wireless communication and power transmission. All are implemented into a flexible biocompatible polymer covered with a thin film encapsulation (TFE) layer.

As described in Sections 2.2.5 and 2.3.3, LCP has gained attention as a new substrate material for implants due to the following advantages: low moisture permeability [1], thermoplasticity, high-temperature compatibility and mechanical stability. Monolithically fabricated LCP-based passive neural electrode arrays have been reported with lifetimes longer than 300 days at 75 °C [3] and up to 158 days at 87 °C [2], both in a phosphate-buffered saline (PBS) solution. The fabrication process of these electrode arrays is based on the fusion of LCP layers during lamination, preventing water ingress and water-vapour condensation in the LCP-LCP interface, which is a common cause of delamination and further failure for polymer-based and encapsulated devices [8]–[11]. Thermal lamination enables monolithic encapsulation of the embedded metallisation [4], [2], while injection moulding [5], [6], jet-deposited glob-top [7], multilayer stacking [8] or thermoforming of LCP lids [3] can be used for encasing the electronic components.

ALD is a chemical-vapour deposition technique that has been widely investigated in the last decade for coating medical devices [9], [10]. Particularly,  $\text{Al}_2\text{O}_3$ ,  $\text{HfO}_2$ , and  $\text{TiO}_2$  oxide layers demonstrated low moisture permeability and conformal coverage with a low density of pinholes [11].  $\text{Al}_2\text{O}_3$ -based ALD also exhibited excellent thermal and mechanical properties, while  $\text{HfO}_2$ -based ALD has high chemical stability in ionic media and anticorrosion properties [12], [13]. Moreover,  $\text{HfO}_2$ -based ALD encapsulation layers with silicone finish have exhibited a long lifetime of over 1028 days at 60 °C in PBS in accelerated ageing tests [14]. Using ALD layers in combination with organic Parylene-C layers, the latter offering conformal coating of sharp edges and gaps down to microns size and ability to serve as a buffer for the high-barrier inorganic ALD layers, could possibly prolong the lifetime of the implant. This is due to an expected increased time needed for water molecules to travel the in-plane direction of several conformal Parylene-C coatings until they reach the defect(s) of low moisture permeable ALD coating and repeat this process through the multilayer stack. [15], [16].

This chapter will describe the investigation and feasibility of using TFE materials with a silicone elastomer finish as a packaging solution for LCP-based implantable bioelectronics. Integration of TFE coatings and silicone finish is aimed to bringing the LCP-substrates one step closer to suitability for active implantable devices. This is necessitated by the limitation of LCP-LCP lamination technology to cover 3D components without destroying them, while the silicone finish intends to reduce the foreign body reaction. Toward this goal, and as a first step, pre-screening tests were carried out to evaluate the interface adhesion of the TFE materials to LCP sheets. This process was used to optimise the deposition parameters of the encapsulation material on LCP substrates. Thin coatings were deposited on LCP substrates and soaked at elevated temperatures in saline and analysed. LCP-on-LCP structures were also fabricated and used as a reference for these investigations. To further evaluate the adhesion of the TFE coatings, T-Peel tests were performed. Although strong adhesion between the layers can be one of the indicators for the long-term performance of the implants, water tightness will also protect the implant from moisture. Therefore, water-vapour transmission rates (WVTR) were calculated for the same coatings. Bending of the coated LCP substrates was performed to take into account the fragility of the thin films when applied to a flexible substrate. Finally, sensitive impedance measurements were performed on interdigitated comb (IDC) metal structures during a long-term accelerated ageing study to estimate the lifetime of the selected coating on LCP. Results show that thin-film encapsulation with a silicone finish can indeed be a viable solution for packaging LCP-based bioelectronics, achieving lifetimes comparable to other LCP-based packaging techniques.

## 3.2. Materials and methods for lifetime estimation

### 3.2.1. Preparation of thin film encapsulation (TFE) layers

For this work, a number of test structures on LCP substrates were prepared and evaluated using two different TFE variations, as described below. For Type 1, a 100nm HfO<sub>2</sub>-based ALD stack (referred to in this chapter as ALD ML or TFE1), consisting of multiple HfO<sub>2</sub>-based ALD layers, was deposited at Picosun Oy using the Picosun® R-200 Advanced ALD reactor, at a pressure of about 1 mbar (N<sub>2</sub> atm.). The PicoHot source system (PH-300) and

PicoSolution (both Picosun Oy) precursors were vaporised from stainless-steel precursor bottles at increased and room temperatures, respectively. Thermal ALD processes at 125 °C were applied to build the HfO<sub>2</sub>-based coating. For the ALD deposition, the LCP samples were placed on top of a Si pocket wafer since only a top coating was needed.

For Type 2, a 7µm stack consisting of Parylene C and Al<sub>2</sub>O<sub>3</sub> and TiO<sub>2</sub> ALD multilayers (referred to as ParC hybrid or TFE2), were deposited at Comelec using the C30H Parylene-ALD hybrid deposition system. More specifically, each TFE2 consists of 1–3 µm Parylene C/3x [Al<sub>2</sub>O<sub>3</sub>/ TiO<sub>2</sub>/Parylene C]/4–6 µm Parylene C. Both ALD and Parylene-C depositions are performed consecutively in the same vacuum vessel and without venting cycles. This eliminates any contamination between the polymer and metal-oxide layers usually present after handling substrates. The Parylene-C layers were deposited at room temperature. The system includes an O<sub>2</sub> plasma-treatment step followed by a silane adhesion-promoter processing step. The deposition of the oxide layers is performed at temperatures below 100 °C. Similarly as for TFE1, precursors were vaporised from stainless steel bottles at increased or room temperature. A more detailed description of the process is explained in [15]. For the silicone elastomer finish, a polydimethylsiloxane (PDMS) layer (MED2-4213, NuSil Carpinteria, Carpinteria, CA, USA) was deposited on top of TFE1 and TFE2. For silicone deposition, vacuum centrifugation followed by curing under high vacuum was used to ensure conformal void-free coating. This additional silicone layer has well-documented biocompatibility, and its Young's modulus is closer to that of soft tissue; hence it is the material of choice to directly interface with tissue. More importantly for this application, as we have previously shown, when used together with thin plasma-enhanced chemical vapour deposition (PECVD) or ALD films, silicone finish coating can offer additional protection to the active device by filling any defects or pores of the ceramic, thus extending the expected lifetime [14], [17]. TFE1-silicone and TFE2-silicone coated test structures were tailored to T-Peel tests, WVTR evaluation and impedance spectrometry. As a reference, LCP-on-LCP (LCP-laminate) samples were also fabricated and included in the investigations. All the material configurations used for different tests are schematically presented in Fig. 3.2 and explained in detail in the following sections.

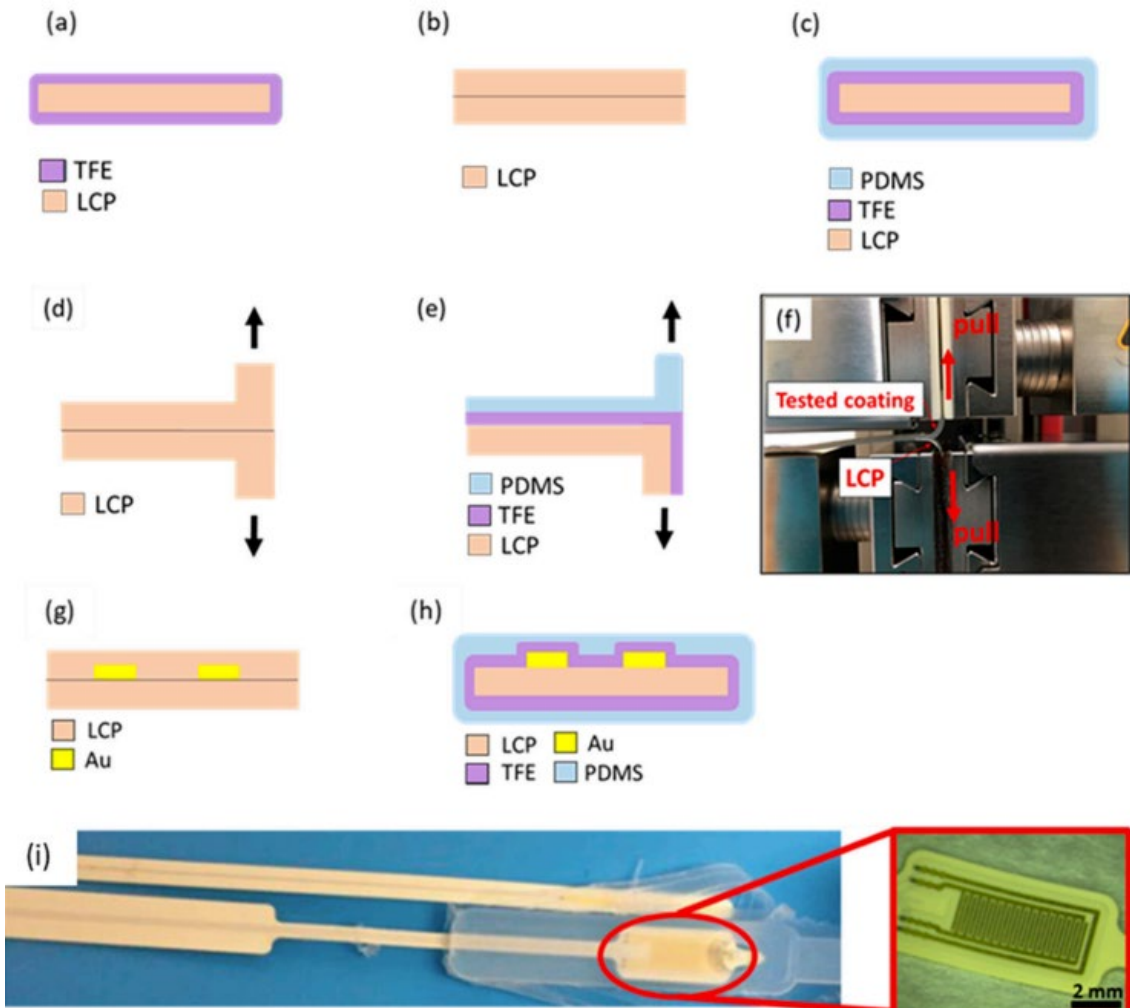


Fig. 3.2. Schematic cross-section illustration of the tested samples: (a) LCP-TFE1/2 samples used for the pre-screening test, (b) LCP-LCP laminate, and (c) LCP-TFE1/2 with silicone finish samples used for sorption tests, LCP-LCP (d) and LCP-TFE1/2 (e) with silicone finish samples used for adhesion T-Peel test. Adapted ASTM D1876 T-Peel test setup with the sample (f). Schematic representation of the IDC tested samples: LCP-Au-LCP (g) and LCP-Au-TFE1/2 with silicone finish (h). Exposed Au IDC test structure on LCP (i).

### 3.2.2. Pre-Screening of the coatings

For the pre-screening test, TFE1 and TFE2 were deposited on LCP substrates, as shown schematically in Fig. 3.2(a). Soaking of the samples was performed



in a water tank that was placed on a hot plate with a thermocouple. The temperature was set at 67 °C and 65 °C for TFE1 and TFE2, respectively. The water tank was sealed with parafilm and aluminium foil to limit evaporation. The samples were placed in glass vials with a top cover. Each sample was placed in a separate vial filled with PBS. Salinity and pH were checked regularly.

Pre-screening was based on optical inspection and cross-section microscopy analyses of the TFE coatings. Scanning electron microscopy (SEM) images of bare LCP and TFE1-covered LCP samples were taken to validate the coating's conformability. For a more detailed analysis, cross-sectioning of the LCP-ALD interface was performed on an FEI Tecnai Osiris (Scanning) Transmission Electron Microscope S/TEM, using the in-situ-focused ion beam (FIB) lift-out technique. Cross-sections of LCP-ALD interfaces were investigated before and after a 2-month ageing study in PBS at 65 °C. This was carried out to evaluate the stability of the coating together with its adhesion to the LCP substrate in an environment mimicking the physiological fluids in the body.

### 3.2.3. Sorption tests and WVTR calculation

WVTRs were calculated from analysing the sorption curves obtained using a sorption analyser (SA Q5000, TA Instruments, New Castle, DE, USA). The procedure was as follows: samples (Fig. 3.2(b),(c)) of approximately 5 × 5 mm<sup>2</sup> were cut and dried at 80 °C for at least 3 hours; the samples were mounted onto a quartz pan and exposed to a 60°C/60% relative humidity (RH) atmosphere; the weight gain was monitored over a period from 24 to 36 hours until saturation was reached. WVTR values were then estimated by multiplication of the permeance  $\Pi$  and the partial pressure of the water vapour  $\Delta p$ :

$$\text{WVTR} = \Pi \cdot \Delta p \quad (1)$$

where the permeance of a film with a membrane thickness  $d$  and permeability  $P$  is  $\Pi = P/d$ . Introducing the solubility  $S$  as the relation between the saturation concentration,  $C_{\text{sat}}$ , and  $\Delta p$  ( $S = C_{\text{sat}}/\Delta p$ ), and diffusion coefficient  $D$ , we obtain:

$$P = S \cdot D = C_{\text{sat}} \cdot D / \Delta p \quad (2)$$

Substituting Equation (2) into Equation (1) gives Equation (3) for calculation of the water-vapour transmission rate

$$WVTR = C_{sat} \cdot D/d \quad (3)$$

This relation contains some simplifications (e.g., a high upstream vapour pressure and a near-zero downstream vapour pressure are assumed), which is why it is used here for comparison rather than for the calculation of absolute values. Samples in a bent state were prepared by constraining the samples into a curved shape using a small pan, achieving a radius of curvature of about 5 mm, which was upheld during the whole measurement period of 24 to 36 hours.

#### 3.2.4. Adhesion evaluation by adapted ASTM D1876 T-Peel test

Adhesion testing was performed on the LCP laminate sample (Fig. 3.2(d)) and the LCP-TFE1-silicone and LCP-TFE2-silicone stacks (Fig. 3.2(e)). An adapted ASTM D1876 T-Peel test was performed as follows: a strip of one of the two bonded materials with a small unbonded area for clamping is prepared; the top and bottom are pulled apart at a constant speed (100 mm/min); the force required to peel the two materials is recorded; the test ends when the sample is completely peeled or one of the materials ruptures (Figure 2(f)). The samples were tested before and after soaking for 24 h at 60 °C in 0.9% saline solution. SEM and energy-dispersive X-ray spectroscopy (EDX) analyses (using a Zeiss Supra 55 VP, 25 kV, and a working distance of 8.5 mm) of the LCP-TFE2 and PDMS surfaces were performed for T-Peel tested samples before and after soaking to evaluate the adhesion of the coating. At least three samples were used for each of the tests and the average values are presented in the results.

#### 3.2.5. Electrochemical impedance spectrometry (EIS) on IDC structures

The long-term performance of the thin encapsulation layers was evaluated by EIS measurements of gold (Au) IDC structures. 3µm thick Au IDCs were electroplated on top of a structured palladium (Pd) seed layer deposited on LCP. For the IDC, 30 fingers were used with a gap of 100 µm, where the width of the Au metallisation was also 100 µm. The IDC dimensions were designed to be 2 mm by 5 mm. A more detailed fabrication procedure of Au IDCs on

LCP has been provided in [4]. After the thin coating deposition, the silicone finish was applied. More specifically, samples were further covered with a 0.5 mm thick low-viscosity silicone layer from both sides to fill in the possible defects or pores in the thin encapsulation layer. The IDC test structures are schematically shown in Fig. 3.2(g),(h). For EIS, all samples were connected to a Solatron Analytic Modulab XM® potentiostat and the impedance between the two metal combs was measured with the samples being immersed in a PBS solution at 60 °C. The recorded spectrum for all the EIS measurements was between 0.1 Hz and 100 kHz. For a bioelectronic implant, besides moisture, the materials and interfaces will also be subjected to electric fields generated by the voltages on the metal traces. Such electric fields could lead to earlier failure of the device. Given that DC voltage have been reported to accelerate failure [18], a group of samples was exposed to a continuous 14V DC voltage. For long-term EIS characterisation and accelerated ageing, a dedicated setup was realised according to [19]. Biweekly in-situ impedance measurements were recorded to monitor the performance of the TFE-silicone coatings over time. A sample was considered to have failed once the impedance magnitude at 0.1 Hz had deviated more than 10% from the original values measured at the beginning of the ageing study.

### 3.3. Results

#### 3.3.1 Pre-screening of the coatings by soaking and optical inspection

The coatings were initially evaluated for stability and absence of visible delamination from LCP immediately after deposition and then after soaking at accelerated temperatures for two months. The LCP coating on the LCP substrate was eliminated from the pre-screening tests due to pre-existing evidence of excellent performance [3], [2]. TFE1 was deposited on a rough LCP substrate; SEM images before and after TFE1 deposition are shown in Fig. 3.3(a),(b). After deposition, the sample was soaked for 2 months at 67 °C. TEM images of the cross-section of the nanolaminate ALD layers are presented in Fig. 3.3(c),(d). The HfO<sub>2</sub>-based ALD ML coating conformally covers the rough topography of the LCP substrate (Fig. 3.3(c)) and stayed intact after the soak (Fig. 3(d)). Similarly, a coating based on TFE2 was deposited on rough LCP

substrates; different parameters, such as ALD thicknesses, pre-treatment, adhesion promoters, number of dyads, and ParC interlayer thicknesses were varied; the samples were soaked for two months at 67 °C; if no visible signs of delamination were observed the process was selected for further tests.

### 3.3.2. Barrier-properties evaluation with sorption test

Sorption tests were used to calculate the water-vapour transmission rate of the coating materials. A low WVTR indicates better moisture protection. As shown in Table 1, the WVTR can be reduced by approximately one hundred times by the addition of TFE1-silicone or TFE2-silicone coatings to bare LCP. The WVTR of the TFE1-silicone increased after bending due to the fragility of the ceramic layers; however, it remained lower than for bare LCP. Bare LCP was assumed to have the same WVTR before and after bending. TFE2-silicone demonstrated better performance than TFE1-silicone after the bending.

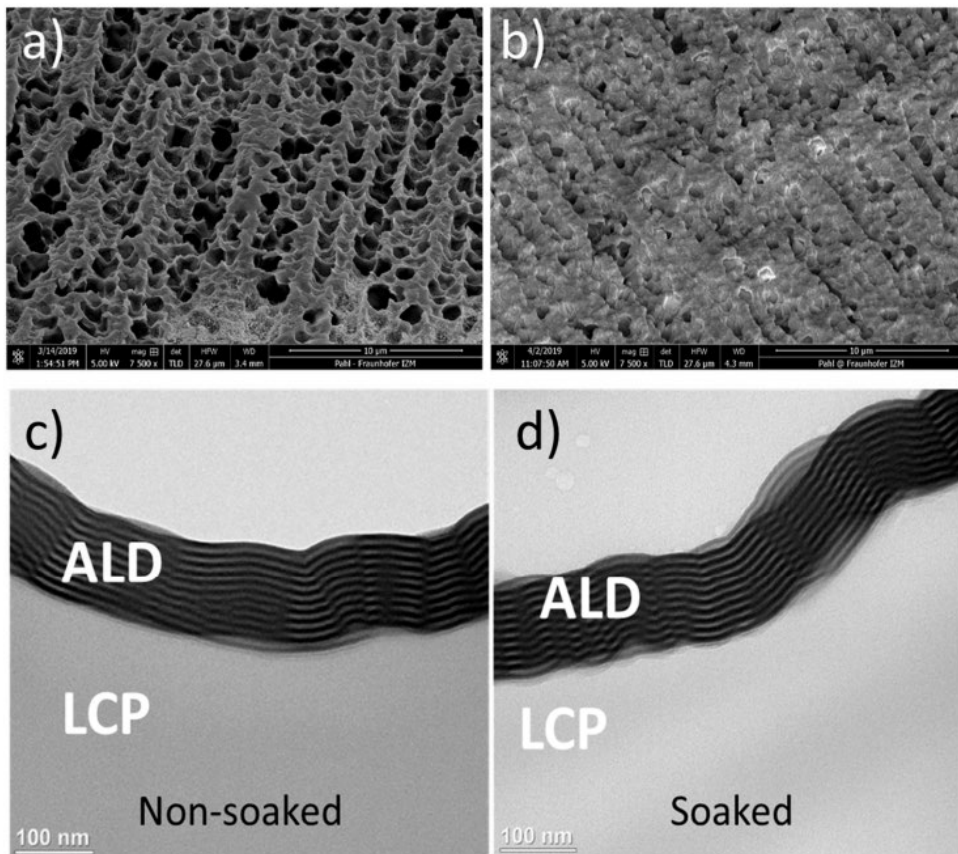


Fig. 3.3. SEM images of bare LCP (a) and LCP coated with a 100 nm thick HfO<sub>2</sub>-based ALD ML (TFE1) (b). Cross-sectional TEM images of 100 nm HfO<sub>2</sub>-based ALD ML on LCP: (c) before soak; (d) after two months soaking in PBS at 67 °C.

Materials stack	Thickness	WVTR	WVTR (After bending*)
LCP	100 μm	202.05 mg/mm <sup>2</sup> day	202.05 mg/mm <sup>2</sup> day
LCP-TFE1	(100±0.1) μm	2.87 mg/mm <sup>2</sup> day	68.61 mg/mm <sup>2</sup> day
LCP-TFE2	(100±7) μm	2.23 mg/mm <sup>2</sup> day	20.66 mg/mm <sup>2</sup> day

Table 3.1. WVTR of the coatings measured with a Sorption Analyser at 60 °C and 60 % relative humidity. \*5 × 5 mm<sup>2</sup> samples were bent to a radius of curvature of about 5 mm for a period from 24 to 36 h (until saturation was reached).

The values obtained for the WVTR and T-Peel tests are given to compare the coatings with each other rather than being absolute values. This is due to the assumptions mentioned in Section 3.2.3, as well as the fact that the WVTR values were derived from Equations (1)–(3) using the values obtained during the sorption test and not measured directly as during the standard MOCOS test. Nevertheless, the values obtained for pure LCP were still comparable to the values in the literature [20], despite the slightly different setup conditions (60 °C/60 % relative humidity instead of 37 °C/100 % relative humidity).

### 3.3.3 Adhesion evaluation with T-Peel test

Table 3.2 gives the average force needed to compromise the adhesion inside each material stack under test, both before and after soaking.

Materials stack	Peel force (Before soak)	Peel force (After soak*)
LCP-LCP	failed to peel	failed to peel
LCP-TFE1-silicone	8 N (btw. TFE1 and LCP)	8 N (btw. TFE1 and LCP)
LCP-TFE2-silicone	0.1 N (btw. TFE2 and silicone)	0.1 N (btw. TFE2 and silicone)

Table 3.2. Peel force required to compromise the adhesion inside each material stack under test. \*Samples were soaked for 24 h at 60 °C in 0.9% saline solution. "Failed to peel" means that the samples got torn during the tests, while the bonded materials' interface integrity was not disrupted.

Soaking for one day did not affect the adhesion properties of the investigated stacks. The LCP-on-LCP reference samples could not be peeled apart. For the LCP-TFE1- silicone, a force of 8 N was required to delaminate TFE1 from the LCP. The integrity of the LCP-TFE2-silicone stack was compromised much earlier, at 0.1 N, however, at a different interface, between TFE2 and silicone. The force required to peel TFE2 from LCP was, therefore not possible to record. In fact, Parylene C, which is the topmost layer of TFE2, has poor adhesion to silicone, and this was proven by the SEM-EDX spectroscopy analysis presented in Table 3.3 and Fig. 3.4, which revealed the presence of TFE2 in the form of chlorine, aluminium and titanium on LCP after the T-Peel test, for both soaked and non-soaked samples..

Before soak			After soak	
Element	On LCP	On PDMS	On LCP	On PDMS
C	80.41%	36.8%	80.13%	36.91%
O	0%	30.72%	0%	31.15%
Si	0.07%	32.48%	0.26%	31.94%
Cl	19.12%	0%	18.85%	0%
Al	0.23%	0%	0.34%	0%
Ti	0.17%	0%	0.11%	0%

Table 3.3. Elemental analysis of the LCP and silicone (PDMS) surfaces after T-Peel test using EDX

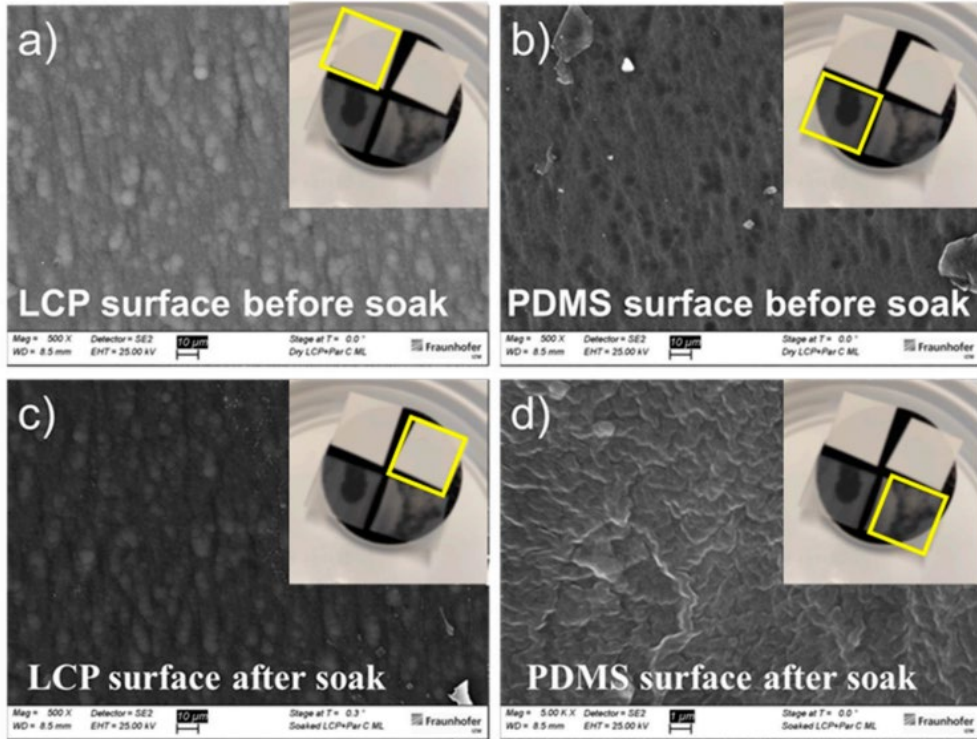


Fig. 3.4. SEM images of LCP (a,c) and PDMS (b,d) surfaces after T-Peel test before and after soaking.

### 3.3.4. Coating performance evaluation with IDC structures

Comb metal structures are highly sensitive in detecting slight changes related to water vapour condensation between the metallisation or any change in the dielectric properties of the insulating materials [21], [22]. Fig. 3.5 provides the lifetimes of all the samples in the long-term ageing study. The LCP-LCP samples were the first group of samples placed in the accelerated ageing study, later followed by the thin-film encapsulated samples. It has to be noted that due to the limited time of the project, the tests were stopped before samples failed. Only in one case, specifically for the TFE2-silicone coatings under 14V bias, the experiment has stopped as all samples reached the end of their lifetime.

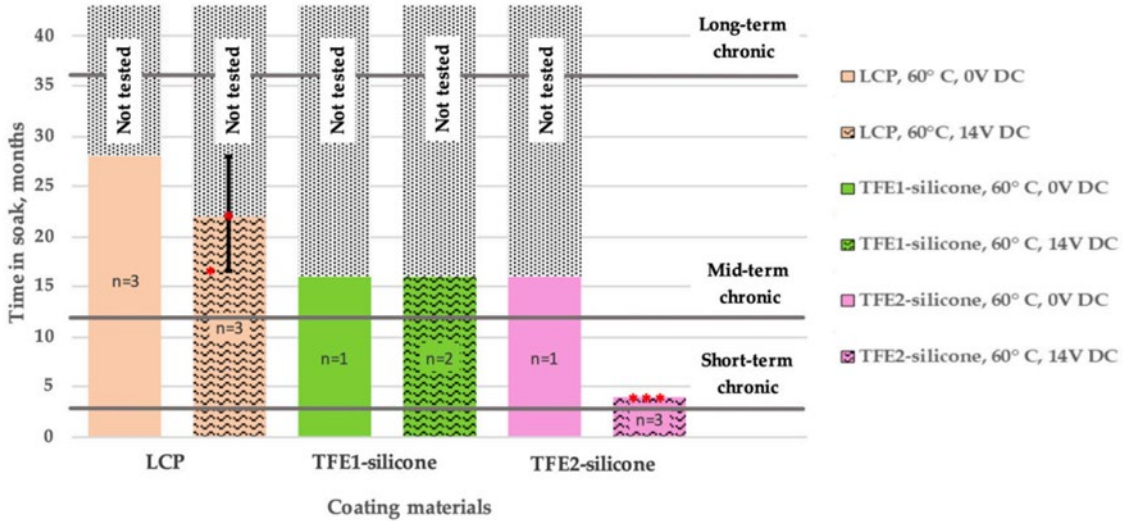


Fig. 3.5. The lifetime of different coatings on LCP substrates with Au IDCs in PBS at 60 °C. The end of a sample's lifetime was indicated by a >10% deviation of the impedance magnitude at 0.1 Hz, compared to the original value at the beginning of the ageing study. Red asterisks (\*) represent failed samples in the corresponding months.

The LCP-LCP samples all showed stable impedance spectra throughout the first year of the ageing study. Extending the study duration, however, led to two of the biased samples failing at Months 16 and 22, respectively. Failure analysis using X-ray microscopy showed a crack/corrosion in a metal trace leading to the IDC, possibly due to impurities in the gold metallisation. Light microscopy did not reveal any signs of corrosion in the interdigitated area, suggesting a hydrolytically stable LCP-LCP lamination between the comb structures. Thin-film-encapsulated IDC structures were in the test for 16 months. For the TFE1-silicone coated IDCs, both non-biased and biased samples showed stable impedances throughout the 16-month duration of soaking. The TFE2-silicone coated IDCs showed failure only when subjected to the 14V DC bias voltage. The failure occurred around Month 4 of the study when a significant impedance drop was recorded, suggesting a gross leakage path between the comb structures.



## 3.4 Discussion

### 3.4.1. Methods used for the evaluation of the proposed TFE coatings

Since there is no established method for the evaluation of the lifetime of TFE and polymer coatings for active neural implants, the presented values and methodologies have limitations that must be considered. These are summarised below. In the literature, predicted lifetimes are commonly calculated from empirical Arrhenius modelling of accelerated reactions, with an acceleration factor  $Q_{10} = 2$ , which states that a rise in temperature of 10 °C will cause approximately a doubling of the rate of chemical reaction [23]. This calculation has its limitations since it does not consider activation energies for the given processes due to practical reasons and can therefore lead to over- or under-estimation of expected lifetimes. Furthermore, it is likely that an increased temperature could cause new failure mechanisms in polymers, which would not happen at 37 °C. Due to the above, we have decided to use conservative approach and abstain from translating our results to expected lifetimes at body temperature. The PBS solution used for soaking the IDC structures cannot fully mimic the aggressive physiological body environment in terms of the expected hydrolytic, oxidative, and enzymatic reactions. This limitation of ageing in PBS is well known, and attempts to overcome it by using hydrogen peroxide instead have appeared in the literature. The use of hydrogen peroxide as a soaking medium aims to mimic the presence of reactive oxygen species comparable to an immune system attack [24].

Since, due to the flexibility and softness of the LCP substrate, it was not possible to use the ASTM D3359 tape test, which is commonly used for adhesion evaluation of the coatings and classifies the obtained values into categories, an adapted ASTM D1876 T-Peel test was used for determining the relative peel resistance. According to the conventional ASTM D3359 tape test, a coating which remains intact after applying a 7N force is classified as 5B and indicates strong adhesion. If we compare it to the relative peel resistance of 8 N, obtained during the LCP-TFE1 T-Peel test, it would also correspond to strong adhesion. Nevertheless, we have used the results obtained from our test to estimate the relative (among compared coatings)

performance of the adhesion to the substrate, and the forces reported here are not equivalent to the ASTM D3359 classification. Similarly, the values obtained for the WVTR are also used to compare the coatings to each other rather than being absolute values. This is due to the assumptions made and the adoption of the tests to our coatings as discussed in Sections 3.2.3 and 3.3.2.

### 3.4.2. Performance of LCP and TFE coatings

Considering the results presented in this chapter, each of the coating options comes with its own advantages and shortcomings. Below we summarise further findings regarding the chosen encapsulation materials that were found during our experiments.

#### *LCP-on-LCP*

Despite having lower barrier properties to moisture ingress, in comparison with the other two coatings, as shown in Table 3.1 and reported in previous literature [1], LCP encapsulated IDC structures can remain functional for up to 28 months at 60 °C in PBS solution with a 14V continuous DC bias. Although the acceleration factor from the constant 14V DC bias voltage cannot be easily derived, the long-lasting performance of the IDC impedance shows that the dielectric properties of the LCP material are outstanding. The stable dielectric properties can be attributed to the low water uptake of LCP, together with its high hydrothermal stability. Between the metal combs, the fusion of the two LCP films prevented any moisture appearance that could otherwise create a shunt leakage path, altering both the impedance magnitude and phase profiles of the EIS measurements. However, the limitation of the LCP-LCP lamination is that it cannot cover 3D components, such as discrete passive components, without additional processing steps since the lamination technology will either destroy the components or it will not allow for a conformal coverage of thick components. Therefore, LCP-LCP lamination can only be the optimal encapsulation solution for relatively thin metal traces but not for relatively thick discrete electronic components. For such systems, the other two TFE strategies mentioned below are recommended.

### *LCP-TFE1-silicone*

In comparison with the bare LCP, the ALD nanolaminates of TFE1 exhibited better barrier properties. See Table 3.1 with calculated WVTR values comparable with those available in the literature [25]. Further advantages of this method of encapsulation include a conformal cover of the substrate, shown by TEM imaging (Fig. 3.3(c),(d)) and improved adhesion to LCP, in comparison with the TFE2, as demonstrated by the results from the T-Peel tests (Table 3.2). However, the very thin ALD layers form a fragile stack, and the bending of the samples significantly increased the average WVTR of the TFE1-silicone coated sample from 2.87 to 68.61 mg/m<sup>2</sup> per day. This puts a significant barrier for the adoption of an encapsulation stack based on ALD with silicone finish on flexible/bendable substrates. Nevertheless, IDC samples coated with TFE1-silicone maintained their functionality for at least 16 months with the 14V DC bias.

### *LCP-TFE2-silicone*

The investigated TFE2-silicone exhibited the best barrier properties, which are very close to the ones exhibited by TFE1-silicone, but, crucially, the integrity of the moisture barrier was not as significantly compromised by bending (Table 3.1). This can be explained by the fact that the Parylene-C layers, which were part of the TFE2 stack, keep the intermediate thin ceramic layers together due to a strong interlayer adhesion. It prevented the fast water ingress, even after bending, by creating a tortuous pathway along the deposited layers, which has been more explained in detail in [15]. A higher moisture barrier will delay polar water molecules from reaching the critical LCP-Parylene-C interface. However, adhesion within the LCP-TFE2-silicone stack was lower compared to other investigated stacks, with the silicone adhesion to Parylene C being the lowest. This was proven by EDX analysis results (Table 3.3). Despite the low adhesion, based on the IDC results, the predicted lifetime of the TFE2-silicone coated samples is at least 16 months at 60 °C, and four months when continuously subjected to a 14V DC bias. For longer-term applications, the weak adhesion observed in this work will be problematic; local delamination is expected, which could introduce stresses in the coating stack and, as a result, reduce the barrier properties. Thus, further improvement at the interface between Parylene C and silicone is needed. This could be achieved by the addition of PECVD ceramic interlayers

[26], [27]. Alternatively, TFE2 could be modified to finish at one of the  $\text{Al}_2\text{O}_3$  and  $\text{TiO}_2$  ALD layers instead of Parylene C.

### 3.4.3. General Remarks

Fig. 3.5 indicates that, even if projected lifetimes are estimated using a conservative approach (not taking into account any acceleration factor), all coatings considered here seem to offer promising encapsulation solutions, at least for short-term (3 months) chronic applications, provided each coating is carefully chosen depending on the intended purpose. LCP coatings, as well as the ALD nanolaminates of TFE1 with a silicone finish, seem to be suitable also for mid-term chronic (~1 year) lifetimes, but TFE2-silicone should be optimised as suggested above. Longer chronic lifetimes (over three years) are significantly harder to achieve and were not the focus of this work. In fact, looking at the performance of the LCP-on-LCP cohort, which was tested over a longer time, we observe that the stability of the stack was compromised for longer test durations, at least in some of the samples that were under 14V DC bias. As the results reported in this thesis demonstrate the viability of using TFE for LCP-based electronics, further evaluations are still needed to realise a fully implantable bioelectronic device based on LCP material. To begin with, optimisation of the stacks and deposition conditions should still be performed. Longer lifetimes can probably be achieved if stronger interface adhesion is realised. For example, surface activation via oxygen plasma and reactive ion etching has been employed, as one of the methods to improve adhesion to LCP [2]. Additionally, adhesion promoters on the LCP substrate to create a long-lasting bond between the TFE and the LCP could be investigated. More detailed chemical and structural analysis between LCP and thin coatings should be performed to study the interface and possible fusion into LCP. The encapsulation of any final assembled LCP substrates with 3D components (ASICs and passive components) is an ongoing investigation. The pilot tests on bent samples of coated LCP suggest that bending of the IDC samples should be performed to evaluate the behaviour of the coating on metal structures. Cleaning and sterilisation procedures during and after manufacturing steps should be implemented in the final process. Finally, in-vivo characterisation of the encapsulation performance should be performed

and compared with the predicted lifetime of the coating calculated from the empirical Arrhenius modelling.

#### 3.4.4. Choosing an appropriate coating for each application

Encapsulation of implantable electronics using polymers and thin-film coatings is a promising solution to design miniaturised, soft, lightweight devices with high biocompatibility, transparency and flexibility. Although all polymers are permeable to water vapour if designed with the appropriately chosen materials and processing parameters, they can provide implants with decades-long lifetimes [28], [13], [17]. Considering the results presented in this chapter, each coating option has its own advantages and shortcomings. While choosing an appropriate coating for each application, the following should be considered: (1) The adhesion of the encapsulation stack to the underlying layer should remain strong for the lifetime of the device. To the best of our knowledge, there is no minimal peel force value that is sufficient for long-term medical implant packaging. (2) Coatings that act as good barriers will not prevent, but only delay water/moisture ingress that would weaken the critical interfacial bonds. They are nevertheless beneficial to extend the time to failure. (3) The coating should conformally cover the underlying substrate to avoid creating any cavities and voids. (4) The coating, together with the substrate material, should both remain stable in wet ionic environments. Ageing tests should be expanded to include applied bias and mechanical stress, both dependent on realistic estimates derived from the specific use case. In practice, conformal encapsulation stacks will rely on achieving a good balance among the aforementioned characteristics to achieve long implant lifetimes.

### 3.5. Conclusion

In recent years, numerous works have shown the potential of LCP in creating high-resolution flexible MEAs [2], [29], [30]. Targeting a fully implantable wireless device with on-board components (coils, interconnect metallisation, ASICs, and passive components), TFE was proposed as a promising small-form-factor packaging solution. ALD nanolaminate and Parylene-C-ALD hybrid multilayers have been investigated as two thin-film encapsulation materials, strengthened by a silicone finish for LCP-based electronic substrates. The encapsulation performance was evaluated using

three different methodologies. More specifically, the adhesion performance of the encapsulation layers on LCP foils was investigated before and after soaking at elevated temperatures, while the WVTR was calculated before and after bending of the samples. The lifetime performance of the two coating multilayers was evaluated using an accelerated ageing study on IDC structures with a DC bias voltage. It was found that TFE-silicone can be a viable technique in packaging LCP-based electronics for short-to-medium-term chronic applications, making this packaging solution a cheap and promising method in realising fully implantable wireless MEAs.

## References

- [1] T. Zhang, W. Johnson, B. Farrell, F. Miller, B. H. Rd, and M. S. Lawrence, "Advanced Packaging Using Liquid Crystalline Polymer (LCP) Substrates," Jan. 2002.
- [2] J. Jeong, K. S. Min, and S. J. Kim, "Microfabrication process for long-term reliable neural electrode arrays using liquid crystal polymer (LCP)," *Microelectron Eng*, vol. 216, p. 111096, Aug. 2019, doi: 10.1016/j.mee.2019.111096.
- [3] S. W. Lee, K. S. Min, J. Jeong, J. Kim, and S. J. Kim, "Monolithic encapsulation of implantable neuroprosthetic devices using liquid crystal polymers," *IEEE Trans Biomed Eng*, vol. 58, no. 8, pp. 2255–2263, Aug. 2011, doi: 10.1109/TBME.2011.2136341.
- [4] M. Wong *et al.*, "Flexible, high-resolution thin-film electrodes for human and animal neural research," *J Neural Eng*, vol. 18, no. 4, p. 45009, Jun. 2021, doi: 10.1088/1741-2552/ac02dc.
- [5] R. J. Ross, "LCP injection molded packages - Keys to JEDEC 1 performance," *Proceedings - Electronic Components and Technology Conference*, vol. 2, no. 510, pp. 1807–1811, Aug. 2004, doi: 10.1109/ectc.2004.1320364.
- [6] S. Long *et al.*, "Injection Molded Liquid Crystal Polymer Package for Chronic Active Implantable Devices with Application to an Optogenetic Stimulator," *IEEE Trans Biomed Eng*, vol. 67, no. 5, pp. 1357–1365, Aug. 2019, doi: 10.1109/TBME.2019.2936577.
- [7] F. F. Faheem, K. C. Gupta, and Y. C. Lee, "Flip-chip assembly and liquid crystal polymer encapsulation for variable MEMS capacitors," *IEEE Trans*

- Microw Theory Tech*, vol. 51, no. 12, pp. 2562–2567, Dec. 2003, doi: 10.1109/TMTT.2003.819778.
- [8] D. C. Thompson, M. M. Tentzeris, and J. Papapolymerou, "Packaging of MMICs in multilayer LCP substrates," *IEEE Microwave and Wireless Components Letters*, vol. 16, no. 7, pp. 410–412, Jul. 2006, doi: 10.1109/LMWC.2006.877130.
- [9] A. S. Jugessur, A. Textor, and C. Grierson, "Nanometer Scale Coating Using Atomic Layer Deposition Technique to Enhance Performance of Bio-Medical Devices," *IEEE International Conference on Nano/Molecular Medicine and Engineering, NANOMED*, pp. 146–149, Feb. 2019, doi: 10.1109/NANOMED.2018.8641639.
- [10] S. A. Skoog, J. W. Elam, and R. J. Narayan, "Atomic layer deposition: Medical and biological applications," *International Materials Reviews*, vol. 58, no. 2, pp. 113–129, Nov. 2013, doi: 10.1179/1743280412Y.0000000009.
- [11] S. M. George, "Atomic layer deposition: An overview," *Chem Rev*, vol. 110, no. 1, pp. 111–131, Nov. 2010, doi: 10.1021/cr900056b.
- [12] M. Li *et al.*, "Comparison of chemical stability and corrosion resistance of group IV metal oxide films formed by thermal and plasma-enhanced atomic layer deposition," *Sci Rep*, vol. 9, no. 1, pp. 1–12, Jul. 2019, doi: 10.1038/s41598-019-47049-z.
- [13] C. Li, M. Cauwe, Y. Yang, D. Schaubroeck, and L. Mader, "Ultra-Long-Term Reliable Encapsulation Using an Atomic Layer Deposited HfO<sub>2</sub>/Al<sub>2</sub>O<sub>3</sub>/HfO<sub>2</sub> Triple-Interlayer for Biomedical Implants," *Coatings*, vol. 9, no. 9, p. 579, Sep. 2019, doi: 10.3390/coatings9090579.
- [14] K. Nanbakhsh, R. Ritasalo, W. A. Serdijn, and V. Giagka, "Long-term Encapsulation of Platinum Metallization Using a HfO<sub>2</sub> ALD - PDMS Bilayer for Non-hermetic Active Implants," *Proceedings - Electronic Components and Technology Conference*, pp. 467–472, Jun. 2020, doi: 10.1109/ECTC32862.2020.00081.
- [15] K. Kim *et al.*, "Extended Barrier Lifetime of Partially Cracked Organic/Inorganic Multilayers for Compliant Implantable Electronics," *Small*, vol. 17, no. 40, p. 2103039, Sep. 2021, doi: 10.1002/smll.202103039.
- [16] G. L. Graff, R. E. Williford, and P. E. Burrows, "Mechanisms of vapor permeation through multilayer barrier films: Lag time versus equilibrium permeation," *J Appl Phys*, vol. 96, no. 4, pp. 1840–1849, Aug. 2004, doi: 10.1063/1.1768610.

- [17] A. Vanhoestenbergh and N. Donaldson, "Corrosion of silicon integrated circuits and lifetime predictions in implantable electronic devices," *J Neural Eng*, vol. 10, no. 3, May 2013, doi: 10.1088/1741-2560/10/3/031002.
- [18] K. Nanbakhsh *et al.*, "Effect of Signals on the Encapsulation Performance of Parylene Coated Platinum Tracks for Active Medical Implants," pp. 3840–3844, Oct. 2019, doi: 10.1109/EMBC.2019.8857702.
- [19] N. Donaldson, C. Lamont, A. S. Idil, M. Mentink, and T. Perkins, "Apparatus to investigate the insulation impedance and accelerated life-testing of neural interfaces," *J Neural Eng*, vol. 15, no. 6, Oct. 2018, doi: 10.1088/1741-2552/aadeac.
- [20] J. Jeong, S. H. Bae, J. Seo, H. Chung, and S. J. Kim, "Long-term evaluation of a liquid crystal polymer (LCP) -based retinal prosthesis," *J. Neural Eng.*, vol. 13, no. 2, p. 25004, Feb. 2016, doi: 10.1088/1741-2560/13/2/025004.
- [21] C. A. Lamont, "Non-Hermetic Protection of Thin-Film Metallisation Layers Intended for Implanted Electronic Medical Devices," 2020.
- [22] C. Lamont *et al.*, "Silicone encapsulation of thin-film SiO<sub>x</sub>, SiO<sub>x</sub>Ny and SiC for modern electronic medical implants: A comparative long-term ageing study," *J Neural Eng*, vol. 18, no. 5, p. 55003, Apr. 2021, doi: 10.1088/1741-2552/abf0d6.
- [23] D. W. L. Hukins, A. Mahomed, and S. N. Kukureka, "Accelerated aging for testing polymeric biomaterials and medical devices," *Med Eng Phys*, vol. 30, pp. 1270–1274, Dec. 2008, doi: 10.1016/j.medengphy.2008.06.001.
- [24] K. A. Potter-baker and R. Capadona, "Reducing the ' Stress ' : Antioxidative Therapeutic and Material Approaches May Prevent Intracortical Microelectrode Failure," *ACS Macro Lett*, vol. 4, no. 3, pp. 275–279, Feb. 2015, doi: 10.1021/mz500743a.
- [25] D. Schaubroeck, R. Verplancke, M. Cauwe, D. Cuypers, and K. Baumans, "Polyimide-ALD-polyimide layers as hermetic encapsulant for implants," *XXXI Int Conf on Surf Mod Tech*, pp. 1–6, Jul. 2017.
- [26] N. B. Babaroud, R. Dekker, W. Serdijn, and V. Giagka, "PDMS-Parylene Adhesion Improvement via Ceramic Interlayers to Strengthen the Encapsulation of Active Neural Implants," *Int Conf IEEE Eng Med Biol Soc*, pp. 3399–3402, Jul. 2020, doi: 10.1109/EMBC44109.2020.9175646.
- [27] N. B. Babaroud *et al.*, "Investigation of the long-term adhesion and barrier properties of a PDMS-Parylene stack with PECVD ceramic interlayers for the conformal encapsulation of neural implants," *23rd European*



*Microelectronics and Packaging Conference & Exhibition (EMPC)*, pp. 1–7, Nov. 2021.

- [28] J. M. Herrera Morales, J.-C. Souriau, and G. Simon, "Corrosion Protection of Silicon Micro Systems with Ultra-Thin Barrier Films for Miniaturized Medical Devices," *ECS Trans*, vol. 69, no. 26, pp. 9–26, Dec. 2015, doi: 10.1149/06926.0009ecst.
- [29] C. J. Lee, S. J. Oh, J. K. Song, and S. J. Kim, "Neural signal recording using microelectrode arrays fabricated on liquid crystal polymer material," *Materials Science and Engineering: C*, vol. 24, no. 1, pp. 265–268, Jan. 2004, doi: 10.1016/j.msec.2003.09.143.
- [30] K. S. Min *et al.*, "A Liquid Crystal Polymer-Based Neuromodulation System : An Application on Animal Model of Neuropathic Pain," vol. 2013, pp. 160–169, May 2014, doi: 10.1111/ner.12093.

# 4

## Thermoplastic polyurethane as a base material for soft neural interfaces

### 4.1 Introduction

Electrical stimulation of active cells by means of neural implantable devices is a powerful tool for treating various neural disorders [1]–[3]. Combined with electrical recording, it can provide a deeper understanding of the underlying neurophysiological processes [4], [5].

Neural interfaces can be made on rigid or soft/flexible substrates. Rigid substrates, commonly made of silicon (Si), are easy to combine with traditional lithography, leading to small feature sizes and high resolution [6]–[10]. However, they leave a more significant impact on the tissue and cause a stronger foreign body reaction (FBR) [11], [12]. Polymer-based neural interfaces, which provide a better match to the mechanical properties of the tissue, are thus often preferred. Polyimide, parylene, and silicone-based neural interfaces have demonstrated great tissue compatibility in various applications [13], [14]. Among these, silicone elastomers are very soft, such that can interact with soft tissue, i.e., the spinal cord or the brain, with minimal impact [15]. However, silicones are not easily compatible with microfabrication techniques; hence, silicone-based neural interfaces suffer from limited feature density and resolution. Further, most biocompatible polymers commonly used as neural implant substrates and coatings are deposited in a layer-to-layer fashion using chemical vapour deposition (CVD) or spin coating [14], [16]–[20]. Because of this layer-to-layer deposition, these polymers face the problem of poor adhesion and delamination at the polymer-polymer interface [21]–[25]. A number of strategies, such as plasma and corona discharge pre-treatment [26], annealing [23], use of adhesion

promoters [24] and interlayers [13], and partial curing [25] are used to improve the adhesion of these polymers to oneself. Nevertheless, the interface always remains present and is considered a critical point of failure, compromising the implant's continuous, long-term stable performance inside the aqueous body environment [21]. On the other hand, thermoplastic polymers, such as liquid crystal polymer (LCP), have demonstrated long-term stability in wet environments and an absence of delamination due to the complete merging of the polymer with itself after thermocompression bonding [27]–[29]. However, LCP is relatively rigid, opaque, unavailable in a medical grade form, and requires high temperatures for processing (over 300 °C), limiting its range of applications for neural interfaces.

In this work, we add polyurethane to the portfolio of biocompatible polymers as a substrate and coating material for soft neural interfaces. Section 2.2.4 provides further details on properties and applications of thermoplastic polyurethane. From Fig. 2.2 it can be also observed that TPUs are softer than Parylene C and Polyimide, but slightly stiffer than silicone elastomers [35], with Young's modulus closer to that of soft brain tissue. In contrast to the latter, TPUs are much more compatible with microfabrication processes such as lithography, supporting high-resolution features. Their transparent to translucent nature renders them compatible with optical imaging, while their thermoplastic nature allows for easy fabrication and strong inter-polymer adhesion. Although, it is important to acknowledge that the soft nature of TPU would also require consideration of the implantation strategy and end-product use application, particularly focusing on surface (non-penetrating) electrodes.

In this study, the thermoplastic properties of polyurethane are used to create a uniform, thin, soft, and flexible insulating environment, within which dense metallization and small, thin chips can be embedded. The developed platform technology enables the fabrication of high-density and high-resolution, soft, and, eventually, active, implantable neural interfaces. This is the first time that TPU is proposed as substrate and coating for neural interfaces. The material availability in a medical grade form, together with its long history in chronic implants, render the hereby proposed approach a prime candidate to develop translational neural implants.

We present a fabrication flow for neural interfaces based on TPU with gold (Au) tracks and electrodes. We employ a polymer-last approach, which, coupled with laser direct imaging (LDI)-based photolithography, enables the creation of dense, high-resolution Au patterns without using any photomasks, yielding an easily adjustable, cheap process. We use a flip-chip bonding step to demonstrate the integration of active components and illustrate the technology's versatility by creating two prototypes of neural implants with dummy chips, with form factors suitable for interfacing with the peripheral and the central nervous system.

## 4.2 Methods

### 4.2.1. Fabrication process

The fabrication process of embedding of the flexible metal tracks and the silicon chip into polyurethane is schematically illustrated in Fig. 4.1

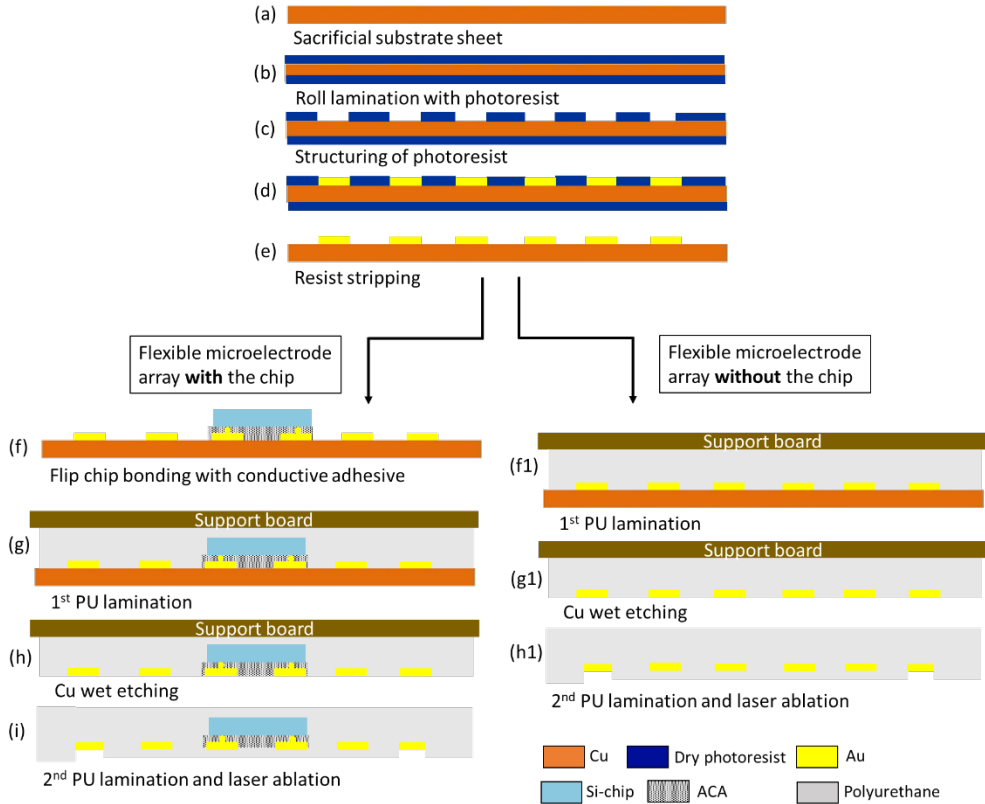


Fig. 4.1. Schematic step-by-step cross-section representation of the platform TPU-based embedding technology. For the active prototypes: after step (e), the process continues in the left column (f-h). For passive electrode arrays: after step (e), the process continues in the right column (f1-h1).

A 70  $\mu\text{m}$  thick roughened copper (Cu) sheet with up to 2  $\mu\text{m}$  roughness, used as a sacrificial substrate (Fig. 4.1(a)), is laminated on both sides with 25  $\mu\text{m}$  dry film photoresist (RD1225, Hitachi) (Fig. 4.1(b)). Subsequently, LDI lithography is used to pattern the resist (Fig. 4.1(c)). A 5  $\mu\text{m}$  gold (Au) layer is deposited by electroplating on the exposed Cu (Fig. 4.1(d)). After chemical removal of the resist (Fig. 4.1(e)), using a 2-aminoethanol ( $\text{C}_2\text{H}_7\text{NO}$ ) and potassium hydroxide (KOH) with a concentration of 10-12% mixture at 50  $^\circ\text{C}$ , a thin silicon chip can be connected to the pads via flip-chip bonding using an anisotropic conductive adhesive (ACA) Fig. 2(f). Next, the first TPU layer (Platilon 4201 AU, Covestro) is laminated on top, together with an FR4-TPU-PTFE-impregnated glass cloth (ACC-14 stiffener, Holders Technology) support stack Fig. 4.1(g). The lamination profile is shown in Appendix A (Fig.

A.1). In the following step, the Cu sacrificial layer is chemically etched in copper chloride ( $\text{CuCl}_2$ ), hydrogen chloride (HCl) and hydrogen peroxide ( $\text{H}_2\text{O}_2$ ) at 50 °C and then rinsed with deionized water (Fig. 4.1(h)). In the last step, the second TPU layer is laminated on the bottom side to electrically insulate the Au structures (the lamination profile is shown in Appendix A, Fig. A.2). Electrode openings were performed on picosecond laser (Schmoll Picodrill) [36]: initial ablation (z - height of the substrate, 1 W power, 200 kHz frequency, 7 repetitions) and post-processing cleaning (z+0.4 mm, 1 W, 400 kHz, 2 repetitions). Extra steps with the same parameters could be performed after z-axis adjustment (in steps of 0.1 mm, higher) until all the visible TPU particles are removed from the gold electrode surface. Due to the heat produced by the laser, TPU would melt and reflow from the edge of the laser opening, decreasing the actual exposed electrode diameter (Appendix A, Table A:1). The final electrode diameter was measured using optical microscopy, and it was the one used for calculations, yet for naming clarity, we will refer to the electrodes by their intended design opening size (700  $\mu\text{m}$  and 300  $\mu\text{m}$ ). An additional electroplating step may also be employed (described in more detail in Section 2.3) to microstructure the surface of the laser-patterned electrodes to increase their effective surface area, in what we call "Shark teeth" electrodes. Finally, the sample is released from the support board (Fig. 4.1(h)), by cutting it out with the scalpel or laser. For the passive electrode array fabrication, we repeat the steps (a-e) and then follow steps (f1-h1) in the right column of Fig.4.2, which are identical to the steps in right column, excluding the chip-bonding step (f).

#### 4.2.2. Accelerated ageing

The gold tracks embedded in polyurethane were fabricated as described in Section 4.2.1 (Fig. 4.1: for passive electrode array (f1-h1)). The gold lines had a thickness of 5  $\mu\text{m}$ , a length of 4 cm and different widths. Layout design shown in Appendix A, Fig. A.4(a). The samples were submerged in PBS (pH 7.4, Carl Roth) and placed in a humidity chamber at 37 °C, and at 67 °C for accelerated aging. Top and bottom view microscopic images of the soaked samples were taken at least every 24 days for 1000, 500, 50  $\mu\text{m}$  widths samples soaked at 37 °C and every 7 days for the for 1000, 500, 200, 50  $\mu\text{m}$  widths samples soaked at 67 °C to assess the long-term adhesion

performance of the gold tracks to TPU. Overall, the samples were soaked for 4.3 months (130 days) at 37 °C and 3.5 months (100 days) at 67 °C.

#### 4.2.3. Electrode fabrication

All gold metal tracks were electroplated (Fig. 4.1(d)) in an electrolytic cell, with a platinised titanium grid as anode and the sample itself as cathode, using a “Keithley 2400” source meter. The cathode and anode were immersed in a conventional soft gold electrolyte (P202, Shloetter) and electroplating was performed at standard conditions (60 °C; pH 6.8; 2.5 mA/cm<sup>2</sup>; 33 mins.), and resulted in a 5 µm thick electroplated gold layer. Electrical characterization of the passive structures was performed with the gold tracks embedded in TPU, fabricated as described in Section 4.2.1 (Fig. 4.1: for passive electrode array (f1-h1)), and creating 700 µm and 300 µm openings during the laser drilling step (Fig. 4.1(i)). Two types of electrodes were fabricated: “Base Au” electrodes (Fig. 4.4(a)), obtained directly after laser ablation, and nanostructured “Shark teeth Au” electrodes (Fig. 4.4(b)), obtained by adding an extra electroplating step after the laser ablation. This additional electroplating step was performed using gravitation-assisted plating without external convection (50 °C; pH 7.5; 2.5 mA/cm<sup>2</sup>, 11 mins.), described in more detail by [37]. The resulting 1 µm nanostructured “Shark teeth Au” layer increased the surface area of the electrode.

#### 4.2.4. Electrochemical characterization

To make contact between the prepared samples and the potentiostat, the interconnection pads of the samples were inserted into a ZIF connector (Molex 52271), and the connector with the soldered metal wires was connected to a Modulab XM potentiostat (AMETEK Solatron Analytical).

Electrochemical impedance spectrometry (EIS), cyclic voltammetry (CV), and voltage transient (VT) experiments were performed in a three-electrode configuration setup. Using a 2 cm x 2 cm x 0.015 cm size Pt sheet counter electrode (CE), a standard Ag/AgCl reference electrode (RE) and alternately used 700 µm diameter “Base Au”, 300 µm diameter “Base Au”, and 700 µm diameter “Shark teeth Au” TPU-embedded working electrodes (WE). All electrodes were immersed in PBS (pH 7.4, Carl Roth) at room temperature. For the EIS and CV tests, grounding was set internally through the AMETEK Solatron Analytical device. An impedance spectrum was obtained by

varying the frequency from 1 Hz to 300 kHz. A 10 mV excitation voltage was applied via the Modulab XM potentiostat. Cyclic voltammograms were recorded at 50 mV/s scan rate within the gold water window potential range of -0.8 to +0.6V. The experiment ran for 50 cycles, allowing the electrode to reach a steady state. Charge Storage Capacity (CSC) was calculated by taking the time integral of the cyclic voltammograms (second to last cycle of the experiment was used). For the cathodic charge storage capacitance (CSC<sub>cath</sub>), only the negative area of the curve was taken into account.

Voltage transient measurements were performed to estimate the charge injection capacity (CIC), particularly a maximum charge that can be injected from the working electrode without an irreversible chemical reaction. An asymmetric (1:4 ratio), cathodic-first biphasic current pulse was supplied between the WE and CE (200  $\mu$ s pulse width, 20  $\mu$ s interphase delay) from a custom built PCB working as a voltage-controlled, current source; coupled with an Arbitrary Function Generator (MDO34, Tektronix) delivering the voltage waveform. Voltage transients were recorded between the WE and RE on a 3-Series Mixed Domain Oscilloscope (MDO34, Tektronix). The current was increased gradually until the interface polarization reaches the water window. The maximum cathodic CIC of the electrode was calculated by multiplying the maximum current amplitude reached for a tested electrode multiplied with the pulse width and dividing by the electrode surface area.

#### 4.2.5. In-vivo implantation and statistical analysis

In-vivo implantation of the samples was done to evaluate the biostability, the biocompatibility and justify the suitability of the fabricated samples for long-term use. Since TPU used in the current paper - Platilon AU 4201 (Covestro) is not certified as a medical grade, medical grade samples prepared from Bionate 80A TPU (DSM Biomedical) used for chronic implantation were implanted, along with pure Platilon TPU samples, and Platilon TPU samples with embedded gold tracks and laser opened electrodes (Fig. 4.4(a)). Three samples of each: Bionate 80A, Platilon AU 4201, Platilon 4201 AU with gold tracks samples had the same dimensions (20 mm x 8 mm x 0.4 mm) and were implanted in female Wistar rats (14 weeks old) obtained from Toxi-Coop (Budapest, Hungary). All procedures were approved by the Institutional Animal Care and Use Committee of the Research Centre for Natural Sciences and by the Hungarian National Scientific Ethical Committee on



Animal Experimentation (permit number: PE/EA/1253-8/2019). The rats were anesthetized with isoflurane gas (2-42.5%), and the polyurethane samples were implanted subcutaneously through a dorsal incision. After 2, 4 and 9.5 months of implantation for pure Platilon and pure Bionate PU, and 5.5, 6, and 9.5 months of implantation for Platilon TPU with gold tracks, the rats were sacrificed for histology. The extracted tissue samples were fixed in a 4% paraformaldehyde solution, embedded in paraffin, Sectioned and stained with Hematoxylin and Eosin (H&E) and trichrome for histological analysis.

Thickness measurements of the encapsulating connective tissue were performed every 500  $\mu\text{m}$  along the track left from the implanted sample. As our data did not follow a normal distribution (verified with the Kolmogorov–Smirnov and Lilliefors test), we provide mean (average) values. The data were analyzed by the Mann-Whitney U test (when comparing two independent samples) or by the Kruskal-Wallis H-test (ANOVA) (when comparing more than two independent samples) with the Bonferroni adjustment. The significance level was set to  $p=0.05$ .

#### 4.2.6. Dummy and active implant prototypes

Two active TPU-based device prototypes (with functional daisy chain chips) and two dummy TPU-based device prototypes (with dummy chips) were fabricated using the process described in Section 4.2.1 (Fig.4.2: for active implants (f-h)).

A 950  $\mu\text{m}$  x 950  $\mu\text{m}$  x 75  $\mu\text{m}$  daisy chain chip with 105  $\mu\text{m}$  x 85  $\mu\text{m}$  x 5  $\mu\text{m}$  bumps (face-up daisy-chain chip (a), complementary substrate layout design (b), and resistance measurement points (c) are shown in Fig. 5.2) was flip-chip bonded to the gold pads using conductive adhesive (TOSHIBA, TAP0201C). Bonding profile is shown in Figure 5.5. Subsequently, the whole sample was embedded in TPU (Fig. 4.5(b)). Another TPU-based active device prototype (Fig. 4.5(e)) with 324 electrodes and metallization resolution up to 20  $\mu\text{m}$  was fabricated following the same process flow. The daisy chain chip was 3.5 mm x 3.5 mm x 300  $\mu\text{m}$  in size and had 60  $\mu\text{m}$  x 60  $\mu\text{m}$  x 10  $\mu\text{m}$  electroplated gold bumps, pitched 80  $\mu\text{m}$  apart.

Two dummy prototypes were prepared with the dummy chips of 1.4 mm x 1.4 mm x 50  $\mu\text{m}$  (Fig. 4.5(c)) (face-up RFID chip (a), corresponding layout of the antenna design (b) are shown in Fig.5.1) and 1.4 mm x 1.4 mm x 30  $\mu\text{m}$

(Fig. 4.5(d)) size, respectively, to demonstrate the possibility of embedding ultra-thin chips and, in the future, using this technology for wireless communication and peripheral nerve stimulation, accordingly.

## 4.3 Results

### 4.3.1. Fusion of polyurethane layers and conformal coverage of gold tracks

For illustration purposes, a cross-section of two non-merged TPU sheets (each 100  $\mu\text{m}$  thick) with the existing polymer-polymer interface laminated with non-optimized lamination parameters, is shown in Fig. 4.2(a) (the lamination profile is shown in Appendix A, Fig. A.3). To demonstrate the merging of the polyurethane layers, a pair of TPU sheets was laminated in vacuum with optimized process parameters (lamination profile shown in Appendix A, Fig. A.2). A cross-section of these layers is shown in Fig. 4.2(b). The long-term stability of such merged layers can be observed from the cross-section of the sample soaked in PBS at 37  $^{\circ}\text{C}$  for 100 days (Fig. 4.2(c)). The in-vivo biostability of the laminated TPU layers was proven by 6 months implantation, cross-section of the five TPU layers shown in Fig. 4.2(d).

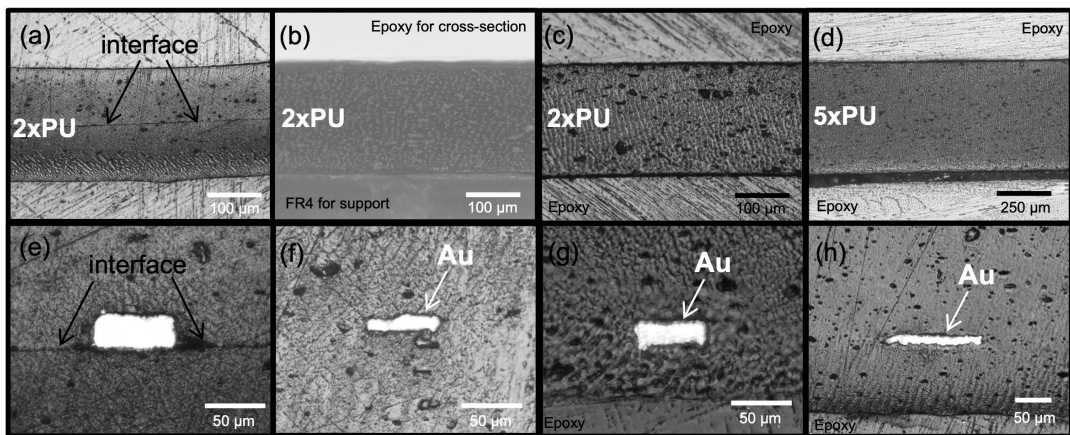


Fig. 4.2. Cross-section image of two non-merged TPU sheets with existing interface laminated under non-optimised parameters (a); cross-section of two completely merged TPU sheets directly after lamination (b) and after 100 days soak in PBS at 37  $^{\circ}\text{C}$  (c); cross-section of five completely merged TPU sheets after six months of implantation (d). 2xTPU and 5xTPU indicating two and five merged TPU layers. Cross-section of two non-merged TPU sheets

around the gold track with existing interface laminated under non-optimised parameters (e); cross-section of two completely merged TPU sheets with embedded gold track directly after lamination (f) and after 100 days soak in PBS at 37 °C (g); cross-section of five completely merged TPU sheets around the gold track after six months of implantation (h).

Two TPU layers laminated around the gold track with optimized parameters are shown in Fig.4.2(e). To demonstrate the conformal coating around the metal tracks, a cross-section of the two TPU layers (100 µm thick each) with the embedded gold interconnect is presented in Fig.4.2(f). To show the long-term stability of such stacks, a cross-section image of the embedded gold track was taken after 100 days in soak (Fig. 4.2(g)) and after 6 months of in-vivo implantation (Fig. 4.2(h)). To assess the effect of the aqueous environment in respect to the track width, soaking of the gold tracks embedded in TPU was conducted (details of the experiment described in Section 4.2.2). The gold tracks stayed without any delamination inside two polyurethane layers for 76 days for 1000 µm and 500 µm width lines, and 27 days for 50 µm width lines, all soaked at 37 °C (microscopy images of the first delamination is shown in Fig. A.4(b-d)). While for the lines soaked at 67 °C the gold tracks stayed without the delamination for 48 days for 1000 µm width lines, more than 98 days for 500 µm and 200 µm width lines, and for 55 days for 50 µm width lines.

#### 4.3.2. Electrode characterization

Scanning electron microscope (SEM) images of the resulting electroplated electrode surfaces of the “Base Au” and “Shark teeth Au” electrodes are shown in Fig. 4.3(a) and Fig. 4.3(b), respectively. The following results for electrochemical characterization are those of single electrodes, chosen as representative of their category. The corresponding electrical impedance spectrograms of the fabricated electrodes are presented in Fig. 4.3(c) (magnitude) and 4.4(d) (phase angle). As expected, the impedance varies with the size and type of the electrodes. The impedance magnitude for the “Base Au” at 1 kHz is 2.4 kΩ for 700 µm diameter electrode and 11.4 kΩ for 300 µm diameter electrode. While for the “Shark teeth Au” the impedance magnitude at 1 kHz is 1.7 kΩ for 700 µm diameter electrode. Both “Base Au” electrodes exhibited a predominantly capacitive behaviour with the impedance values within the typical range for gold thin-film electrodes [38],

[39] and for the 700  $\mu\text{m}$  "Shark teeth Au" electrodes even lower values [40], [41].

The cyclic voltammogram curves for three types of the representative electrodes are shown in Fig. 4.3(e). For the 700 $\mu\text{m}$  opening "Base Au" thin-film electrode, calculated CSC was 0.18  $\text{mC}/\text{cm}^2$ . While for the "Shark teeth Au" with a 700 $\mu\text{m}$  opening and "Base Au" with a 300  $\mu\text{m}$  electrodes these values were 0.39  $\text{mC}/\text{cm}^2$ .

Measured voltage transients (VT) of the electrodes are presented in Fig. 4.3(f-h). The charge injection capacity values amount to 68  $\mu\text{C}/\text{cm}^2$  and 24  $\mu\text{C}/\text{cm}^2$  for 700  $\mu\text{m}$  and 300  $\mu\text{m}$  diameter "Base Au" electrodes, respectively. While for the "Shark teeth Au" electrodes this value amounts to 137  $\mu\text{C}/\text{cm}^2$  for a 700  $\mu\text{m}$  diameter.

Electrode Category	$ Z $ @ 1kHz (k $\Omega$ )	CSC ( $\text{mC}/\text{cm}^2$ )	CSC <sub>cath</sub> ( $\text{mC}/\text{cm}^2$ )	CIC ( $\text{mC}/\text{cm}^2$ )
"Base Au" 700 $\mu\text{m}$ $\emptyset$	2.423	0.179	0.118	0.068
"Base Au" 300 $\mu\text{m}$ $\emptyset$	11.443	0.388	0.265	0.024
"Shark teeth Au 700 $\mu\text{m}$ $\emptyset$	1.667	0.388	0.236	0.137

Table 4.1. Comparative table of impedance magnitude at 1kHz  $|z|$ , total and cathodic charge storage capacities (CSC), and charge injection capacity (CIC) values for the three categories of electrodes: 700  $\mu\text{m}$  "Base Au", 300

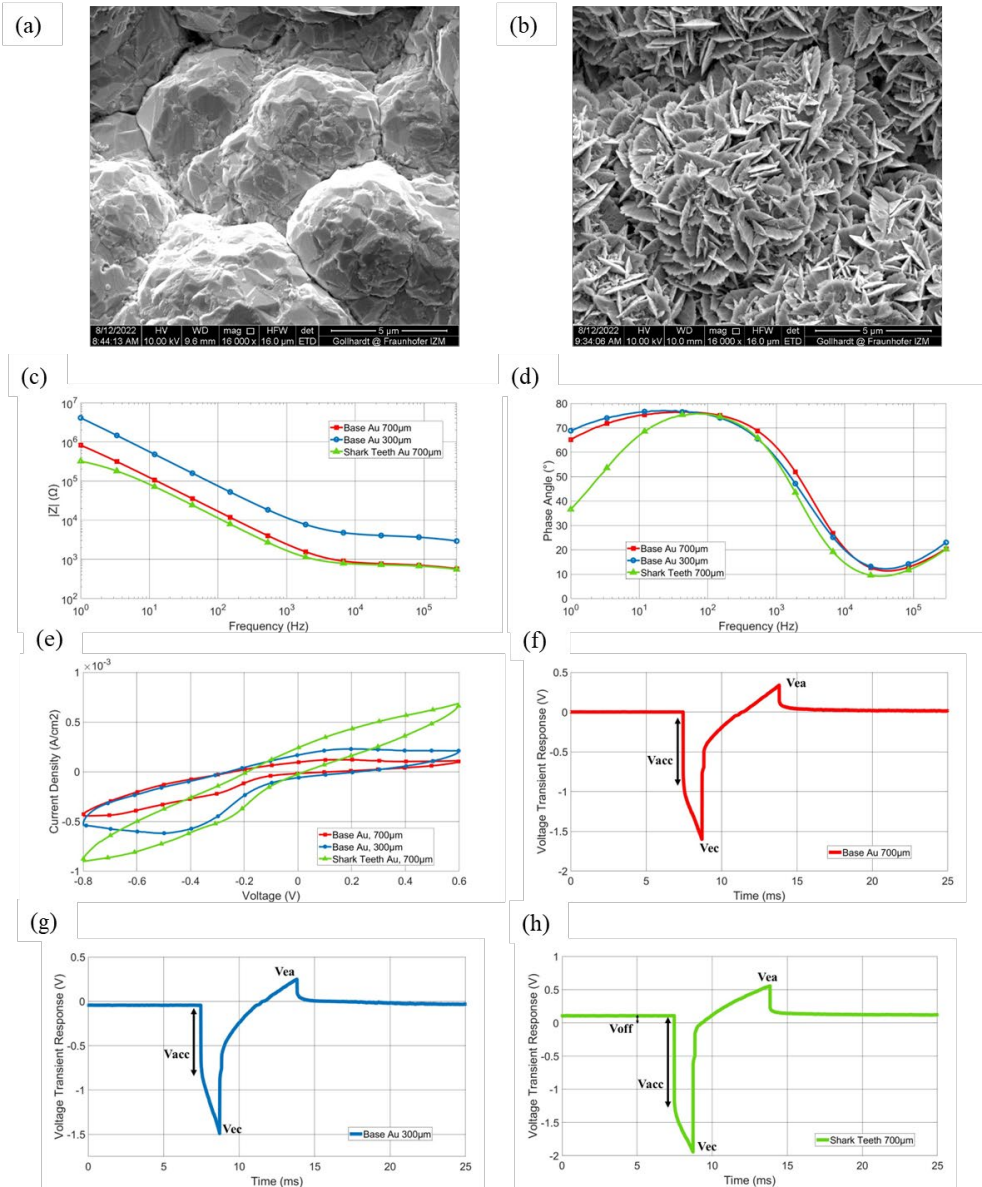


Fig. 4.3. SEM images of (a) “Base Au” and (b) nanostructured “Shark teeth Au” electroplated gold. (c) Impedance magnitude and (d) phase angle plots for 700  $\mu\text{m}$  “Base Au”, 300  $\mu\text{m}$  “Base Au”, and 700  $\mu\text{m}$  “Shark teeth Au” electrodes. (e) Cyclic voltammograms (50mV/s scan rate) and (f-h) voltage transient measurements for the same gold electrodes.

### 4.3.3. Biocompatibility and biostability of bioelectronic foils

#### 4.3.3.1 Biocompatibility

Pure polyurethane and polyurethane with gold metallization samples (bioelectronic foils, Figure 4.5(a-c)) were surgically implanted under a rat's skin (Fig. 4.4(f)). The thickness of the encapsulating connective tissue formed around the implant was visualized using H&E staining (Fig. 4.4(g)). Connective tissue thickness measurements were performed every 500  $\mu\text{m}$  along the track left from the implanted sample. The number of measurement points, as well as the median (1<sup>st</sup> – 3<sup>rd</sup> quartiles) values are given in Table A.2 of the Appendix A. The histological findings for pure TPU samples (Fig. 4.4(h)) show that after two months of implantation the mean (average) thickness of encapsulating tissue is 143  $\mu\text{m}$ , while for the sample implanted for four months the thickness has almost doubled to 227  $\mu\text{m}$ , although after 10 months of implantation this value decreased again to 185  $\mu\text{m}$ . As for the bioelectronic foils, the highest value of the average encapsulation tissue thickness was observed after 6 months of implantation and amounted to 295  $\mu\text{m}$ . The average fibrous capsule thickness value, after nine months of implantation was 216  $\mu\text{m}$  for Platilon (Fig. 4.4(h)) and 289  $\mu\text{m}$  for Bionate polyurethane (Fig. 4.4(i)), which is in the same order of magnitude as for other subcutaneous implants, reported in the literature [42]–[44]. After 9.5-month implantation no sign of inflammatory reaction was observed. Eosinophils and neutrophils were rarely visible indicating only mild inflammatory response on the implanted samples from the body. A mature fibrotic tissue with a low amount of fibroblasts is visible in case of 9.5 months survival.

Since the fabrication involves the use of copper sheets as sacrificial substrates that are later etched, an elemental analysis was performed to ensure the biocompatibility and safety of the fabricated samples for the human body. Copper concentrations were measured using a scanning electron microscope (Zeiss Supra 55 VP, 10 and 5 kV stimulation voltage, working distance of 8.5 mm). Four bioelectronic foils (TPU samples with embedded gold electrodes) were analyzed using Energy Dispersive X-ray analysis: non-implanted, 15 minutes ultrasonicated (Sample 1), non-implanted not ultrasonicated (Sample 2), 5 months implanted (Sample 3) and 9 months implanted (Sample 4) (Fig.4.5(j)). Ultrasonication is a common

technique for sample cleaning and sterilization, where high-frequency sound waves are used to clean the surface from organic contaminations. The values indicated in the table in Fig.4.5(j) indicate the average of the six measurements for each of the elements. The weight of samples 1-4 in our experiments varied from 92.1 to 121.3 mg. Assuming the copper redistributed evenly within each sample the overall weight of copper in each of the samples does not exceed 48.4  $\mu\text{g}$ , which is orders of magnitude lower than the 70-80 mg of copper that is present on average in humans [45]. Moreover, it is less than the Adequate Intake (AI) limit of 1.6 mg/day for men and 1.3 mg/day for women as proposed by the European Food Safety Authority [46]. Therefore, these results suggest that the amount of copper still present in the samples is insignificant for the human body.

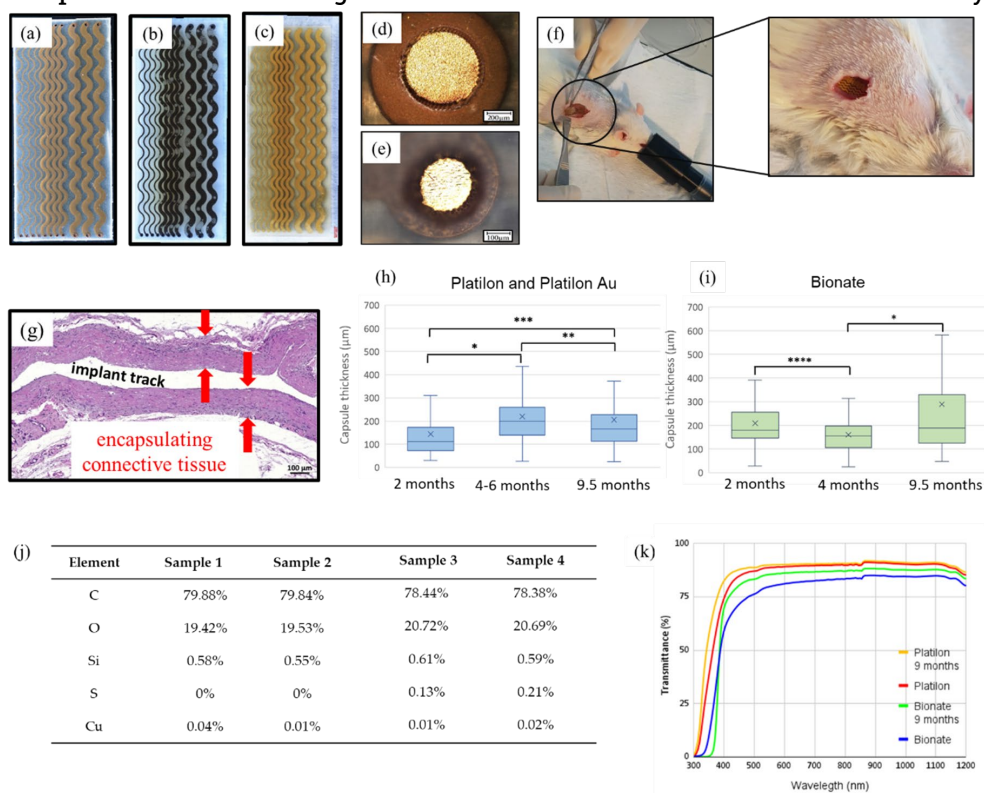


Fig. 4.4. Polyurethane sample with embedded gold electrodes before (a) and after 9 months of implantation, seen from the top (b) and bottom (c), together with the zoomed-in image of the electrodes of 700  $\mu\text{m}$  and 300  $\mu\text{m}$  diameter (d,e), showing no damage to the electrode after the implantation. Surgical implantation of the TPU samples underneath the skin at the back of the rat

(f). Histological H&E image of the encapsulating connective tissue formed around the implanted sample (g). Thicknesses of the encapsulating connective tissue for pure Platilon TPU and Platilon TPU with gold electrodes (h) (\* $p < 0.001$ , \*\* $p = 0.03$ , \*\*\* $p < 0.001$ ) vs. pure Bionate polyurethane (i) (\*\*\*\* $p = 0.007$ , \* $p < 0.001$ ) analysed with the Mann-Whitney U test (when comparing two independent samples) or the Kruskal-Wallis H test (when comparing more than two independent samples) with the Bonferroni adjustment. The box plots also indicate the mean (cross sign), and the median (horizontal line inside the box). Elemental analysis of the four TPU samples (j): non-implanted, 15 minutes ultrasonicated (Sample 1), non-implanted not ultrasonicated (Sample 2), 5 months implanted (Sample 3) and 9 months implanted (Sample 4). Optical transmittance of the Platilon and Bionate TPU samples, before and after nine months of implantation (k).

#### 4.3.3.2 Biostability

Microscopy images taken after explantation of the samples are shown in Fig. 4.4(b-e). These reveal no damage to the electrode. A local delamination of the gold from the TPU is sometimes observed within the bioelectronic foils, but no serious damage or interruption of the gold tracks (Figure 4.5(b,c)). Conductivity measurements after the explantation proved that the lines remained electrically functional ( $R$  lower than  $20 \Omega$ ). The optical transparency of the pure Platilon and medical-grade Bionate polyurethanes was measured before and after nine months of implantation (Fig.4.5(k)). A quantitative evaluation was conducted using a Perkin Elmer Lambda 950 UV/Vis (PerkinElmer, Waltham, Massachusetts). The transmittance of Platilon at 470 nm (a wavelength that is, commonly used for optogenetic stimulation) amounted to 88% before and 86% after implantation. At the same time, for Bionate these values were 82% and 74%, respectively. Both materials exhibited a high transparency that allows the fabricated TPU to be potentially used in optogenetics.

#### 4.3.4. Dummy active neural interface prototypes

We have fabricated active TPU-based devices (Fig. 4.5) by embedding silicon chips in the TPU layers using the process introduced in this work. We were capable of creating electrode arrays with a track width of  $20 \mu\text{m}$  and a pitch of  $30 \mu\text{m}$ , which is higher than the resolution that can be achieved with any



other reported fabrication process for such pliable and soft material (1 MPa range) [47]–[51]. We have successfully embedded large (3.5 mm x 3.5 mm) and thick (300  $\mu\text{m}$ ), but also small (950  $\mu\text{m}$  x 950  $\mu\text{m}$ ) and thin (75  $\mu\text{m}$ ) daisy chain chips within the bioelectronic foils, as shown in Fig. 4.5 (e) and (b), respectively. We could contact up to 324 electrodes with a metallization resolution down to 20  $\mu\text{m}$ .

A cross-section of the bonded chip is shown in Fig. 4.5(a), depicting 5  $\mu\text{m}$  thick electroplated bumps successfully connected to the gold tracks. This process can be used for the fabrication of active neural interfaces with form factors fitting the central (Fig. 4.5(e)) or peripheral (Fig. 4.5(d), dummy) nervous system. Depending on the silicon chip functionality, these implants could enable multichannel recording or stimulation from large (or multiple) neuronal areas or from small volumes at a high resolution.

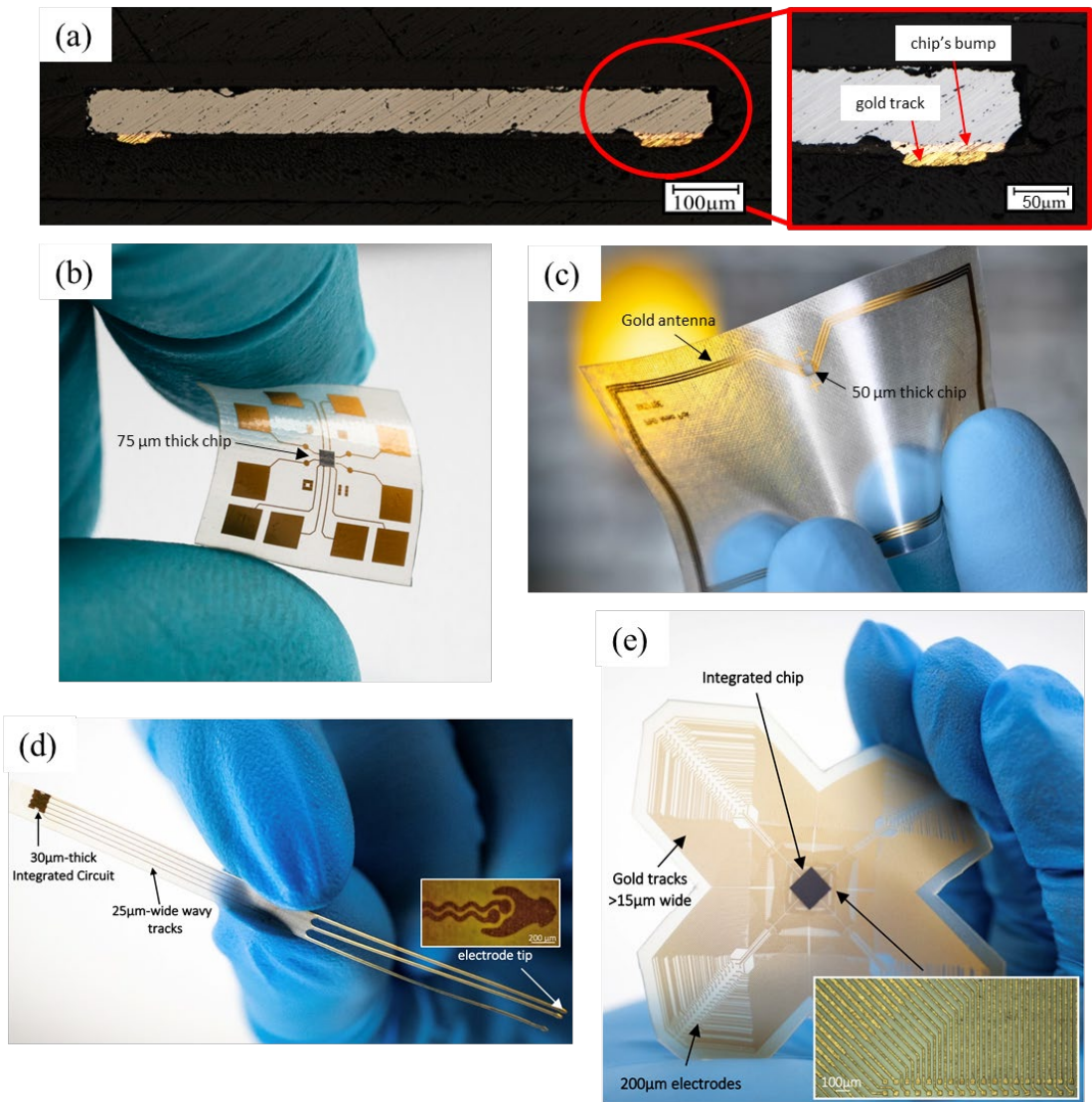


Fig. 4.5. TPU-based flexible neural implant's prototypes: (a) cross-section of the daisy chain chip connected to the gold tracks, (b) daisy-chain chip connected to corresponding gold tracks, (c) silicon chip embedded in bioelectronic foil with gold antenna, (d) thinned dummy chip embedded in bioelectronic foil intended for peripheral nervous system, (e) high-density implant prototype for central nervous system with 324 electrodes (e).

## 4.4 Discussion

Using the developed process, we were capable of achieving a 20  $\mu\text{m}$  line width and a 30  $\mu\text{m}$  pitch resolution for the first time in such pliable and soft material. This was because we were able to use lithography for gold tracks plating on a sacrificial substrate and later transfer them to the polyurethane substrate, while usually to get metal tracks on pliable substrates, such methods as inkjet printing, soft lithography or screen printing are used, which do not allow for such high resolutions. However, conventional lithography processing is a time-consuming and expensive process, requiring ordering a new photomask, for each new design. Here, we adapted an LDI process, used in PCB manufacturing to our process. LDI does not require any photomasks, since the laser beam is selectively exposing the digitally saved pattern to the photoresist. If implemented with polymer processing, it offers us an easily adjustable, cheap, fast process. We electrically characterized the created structures by impedance spectrometry, cyclic voltammetry, voltage recordings during pulsatile stimulation, and contact resistance measurements. The “Shark teeth Au” electrodes exhibit low impedance values at 1 kHz (1.7 k $\Omega$  for 700  $\mu\text{m}$  diameter electrodes) and high charge injection capacity (137  $\mu\text{C}/\text{cm}^2$  for 700  $\mu\text{m}$  diameter electrodes) that increases stimulation current transfer capability of the electrode. CSC values were one order of magnitude lower than other reported. This can be due to the fact that during laser ablation, tiny particles of vaporized material might be redeposited to the electrode surface. Initial mechanical characterization tests were performed and discussed in Appendix B. The long-term viability was demonstrated by soaking the samples for 130 days in PBS at 37  $^{\circ}\text{C}$ , and for 100 days at 67  $^{\circ}\text{C}$ , showing no tracks delamination for 500  $\mu\text{m}$  and 200  $\mu\text{m}$  lines widths. Finally, the samples were evaluated in-vivo to prove their biostability and biocompatibility. During the course of the study over 9.5 months, no degradation of the device by macrophages was observed. There was no tissue necrosis associated with the implant substrates. Optical transmittance measurements were performed to demonstrate the feasibility of the developed implants to be used in combination with optical stimulation. The results, collected from the cross-sectioning, long-term soaking, and in-vivo testing of the fabricated samples highlight the properties of TPU as a suitable material for chronic active

neural implants encapsulation. Having a low Young's modulus, combined with miniaturization of the device during its fabrication via the developed process, allows the implant to mimic the underlying tissue. This will ensure minimal foreign body reaction and thus reduce the potential rejection of the implant. In the future, such an implant can be powered wirelessly, by connecting the chip to the antenna/coil or by adding ultrasound transducers, therefore, eliminating the need for extra surgical procedures for battery replacement. We have shown that the current process technology allows for the fabrication of a flexible active implant. The developed process allows for a seamless fabrication, which results in a single polymer layer (no polymer-polymer interface) and conformal cover of the metallization. Further reduction of the interfaces within the implant is possible by using TPU as an underfill material. This will require optimization of the temperature and pressure profile for piercing through TPU film with the bumps. More details can be found in [52], [53]. Long-term experimental investigations are required to explore the efficacy of TPU in safeguarding Si chips. Additionally, strategies for enhancing the adhesion between polyurethane and gold need to be explored.

## 4.5 Conclusion

In this work, we developed a platform technology to enable the fabrication of a flexible active implant prototype which could interact with the neural tissue. We used the thermoplastic properties of polyurethane to create a uniform, thin, soft and flexible insulating environment within which gold metallization and thinned chips were embedded. A 75  $\mu\text{m}$  thin and 300  $\mu\text{m}$  thick chips were bonded to 5  $\mu\text{m}$  thick gold tracks to validate the process. The process allowed for a seamless fabrication, resulting in a single polymer layer avoiding the polymer-polymer interface. The resulting prototypes were characterized for electrical, long-term soak, *in-vivo* and optical performance.

## References

- [1] C. N. Heck *et al.*, "Two-year seizure reduction in adults with medically intractable partial onset epilepsy treated with responsive neurostimulation:

- Final results of the RNS System Pivotal trial," *Epilepsia*, vol. 55, no. 3, pp. 432–441, Feb. 2014, doi: 10.1111/epi.12534.
- [2] F. B. Wagner *et al.*, "Targeted neurotechnology restores walking in humans with spinal cord injury," *Nature*, vol. 563, pp. 65–71, Nov. 2018, doi: 10.1038/s41586-018-0649-2.
- [3] N. C. Swann *et al.*, "Adaptive deep brain stimulation for Parkinson's disease using motor cortex sensing," *J Neural Eng*, vol. 15, no. 4, pp. 1–10, May 2018, doi: 10.1088/1741-2552/aabc9b.
- [4] M. Meister, J. Pine, and D. A. Baylor, "Multi-neuronal signals from the retina: acquisition and analysis," *J Neurosci Methods*, vol. 51, pp. 95–106, 1994.
- [5] R. J. Vetter, J. C. Williams, J. F. Hetke, E. A. Nunamaker, and D. R. Kipke, "Chronic neural recording using silicon-substrate microelectrode arrays implanted in cerebral cortex," *IEEE Trans Biomed Eng*, vol. 51, no. 6, pp. 896–904, 2004, doi: 10.1109/TBME.2004.826680.
- [6] D. Kensall and B. James, "Integrated-Circuit Microelectrodes," no. 3, pp. 238–247, 1970.
- [7] P. K. Campbell *et al.*, "A Silicon-Based , Three-Dimensional Neural Interface : Manufacturing Processes for an Intracortical Electrode Array," vol. 38, no. 8, 1991.
- [8] E. M. Maynard, C. T. Nordhausen, and R. A. Normann, "The Utah Intracortical Electrode Array: A recording structure for potential brain-computer interfaces," *Electroencephalogr Clin Neurophysiol*, vol. 102, no. 3, pp. 228–239, 1997, doi: 10.1016/S0013-4694(96)95176-0.
- [9] J. Jeong *et al.*, "Conformal Hermetic Sealing of Wireless Microelectronic Implantable Chiplets by Multilayered Atomic Layer Deposition (ALD)," *Adv Funct Mater*, vol. 29, no. 5, pp. 1–10, 2019, doi: 10.1002/adfm.201806440.
- [10] R. Fiáth, D. Meszéna, Z. Somogyvári, M. Boda, and P. Barthó, "Recording site placement on planar silicon - based probes affects signal quality in acute neuronal recordings," *Sci Rep*, pp. 1–18, 2021, doi: 10.1038/s41598-021-81127-5.
- [11] M. Gulino, D. Kim, S. Pané, S. D. Santos, and A. P. Pêgo, "Tissue Response to Neural Implants : The Use of Model Systems Toward New Design Solutions

of Implantable Microelectrodes," vol. 13, no. July, pp. 1–24, 2019, doi: 10.3389/fnins.2019.00689.

- [12] J. C. Barrese *et al.*, "Failure mode analysis of silicon-based intracortical microelectrode arrays in non-human primates," *J Neural Eng*, vol. 10, no. 6, 2013, doi: 10.1088/1741-2560/10/6/066014.
- [13] J. S. Ordonez, C. Boehler, M. Schuettler, and T. Stieglitz, "Improved polyimide thin-film electrodes for neural implants," *2012 Annual International Conference of the IEEE Engineering in Medicine and Biology Society*, pp. 5134–5137, Sep. 2012, doi: 10.1109/EMBC.2012.6347149.
- [14] D. C. Rodger *et al.*, "Flexible parylene-based multielectrode array technology for high-density neural stimulation and recording," *Sens Actuators B Chem*, vol. 132, no. 2, pp. 449–460, Jun. 2008, doi: 10.1016/j.snb.2007.10.069.
- [15] Ivan R. Minev *et al.*, "Electronic dura mater for long-term multimodal neural interfaces," *Science*, vol. 347, no. 6218, pp. 154–159, Jan. 2015, doi: 10.1126/science.1260960.
- [16] P. J. Rousche, D. S. Pellinen, D. P. Pivin, J. C. Williams, R. J. Vetter, and D. R. Kipke, "Flexible polyimide-based intracortical electrode arrays with bioactive capability," *IEEE Trans Biomed Eng*, vol. 48, no. 3, pp. 361–370, 2001, doi: 10.1109/10.914800.
- [17] S. Myllymaa *et al.*, "Fabrication and testing of polyimide-based microelectrode arrays for cortical mapping of evoked potentials," *Biosens Bioelectron*, vol. 24, no. 10, pp. 3067–3072, 2009, doi: 10.1016/j.bios.2009.03.028.
- [18] B. Rubehn, C. Bosman, R. Oostenveld, P. Fries, and T. Stieglitz, "A MEMS-based flexible multichannel ECoG-electrode array," *J Neural Eng*, vol. 6, no. 3, 2009, doi: 10.1088/1741-2560/6/3/036003.
- [19] B. J. Kim and E. Meng, "Review of polymer MEMS micromachining," *Journal of Micromechanics and Microengineering*, vol. 26, no. 1, p. 13001, 2015, doi: 10.1088/0960-1317/26/1/013001.
- [20] L. Guo, G. S. Guvanasen, X. Liu, C. Tuthill, T. R. Nichols, and S. P. Deweerth, "A PDMS-based integrated stretchable microelectrode array (isMEA) for

neural and muscular surface interfacing," *IEEE Trans Biomed Circuits Syst*, vol. 7, no. 1, pp. 1–10, 2013, doi: 10.1109/TBCAS.2012.2192932.

- [21] J. Ortigoza-diaz *et al.*, "Techniques and Considerations in the Microfabrication of Parylene C Microelectromechanical Systems," 2018, doi: 10.3390/mi9090422.
- [22] M. Tintelott and A. Schander, "Understanding Electrical Failure of Polyimide-Based Flexible Neural Implants : The Role of Thin Film Adhesion," *Polymers (Basel)*, vol. 14, no. 18, pp. 1–11, Sep. 2022, doi: 10.3390/polym14183702.
- [23] R. P. Von Metzen and T. Stieglitz, "The effects of annealing on mechanical , chemical , and physical properties and structural stability of Parylene C," *Biomed Microdevices*, vol. 15, pp. 727–735, Mar. 2013, doi: 10.1007/s10544-013-9758-8.
- [24] K. Koh, J. Chin, J. Chia, and C. Chiang, "Quantitative Studies on PDMS-PDMS Interface Bonding with Piranha Solution and its Swelling Effect," *Micromachines (Basel)*, vol. 3, no. 2, pp. 427–441, May 2012, doi: 10.3390/mi3020427.
- [25] M. A. Eddings, M. A. Johnson, and B. K. Gale, "Determining the optimal PDMS-PDMS bonding technique for microfluidic devices," *Journal of Micromechanics and Microengineering*, vol. 18, no. 6, pp. 1–4, Apr. 2008, doi: 10.1088/0960-1317/18/6/067001.
- [26] C. Yang, W. Wang, and Z. Li, "Optimization of Corona-triggered PDMS-PDMS Bonding Method," pp. 319–322, Jan. 2009, doi: 10.1109/NEMS.2009.5068586.
- [27] S. W. Lee, K. S. Min, J. Jeong, J. Kim, and S. J. Kim, "Monolithic encapsulation of implantable neuroprosthetic devices using liquid crystal polymers," *IEEE Trans Biomed Eng*, vol. 58, no. 8, pp. 2255–2263, Aug. 2011, doi: 10.1109/TBME.2011.2136341.
- [28] J. Jeong, K. Sik, and S. June, "Microfabrication process for long-term reliable neural electrode arrays using liquid crystal polymer ( LCP )," *Microelectron Eng*, vol. 216, no. January, p. 111096, 2019, doi: 10.1016/j.mee.2019.111096.

- [29] A. Pak *et al.*, "Thin Film Encapsulation for LCP-Based Flexible Bioelectronic Implants : Comparison of Different Coating Materials Using Test Methodologies for Life-Time Estimation," 2022.
- [30] T. Hentschel and H. Münstedl, "Thermoplastic polyurethane - The material used for the Erlanger silver catheter," *Infection*, vol. 27, no. SUPPL. 1, pp. 43–45, 1999, doi: 10.1007/BF02561617.
- [31] P. Volkow *et al.*, "Polyurethane II catheter as long-indwelling intravenous catheter in patients with cancer," *Am J Infect Control*, vol. 31, no. 7, pp. 392–396, 2003, doi: 10.1067/mic.2003.39.
- [32] M. Wildgruber *et al.*, "Polyurethane versus silicone catheters for central venous port devices implanted at the forearm," *Eur J Cancer*, vol. 59, pp. 113–124, 2016, doi: 10.1016/j.ejca.2016.02.011.
- [33] J. P. Theron *et al.*, "Modification, crosslinking and reactive electrospinning of a thermoplastic medical polyurethane for vascular graft applications," *Acta Biomater*, vol. 6, no. 7, pp. 2434–2447, 2010, doi: 10.1016/j.actbio.2010.01.013.
- [34] Y. S. Choi *et al.*, "Stretchable, dynamic covalent polymers for soft, long-lived bioresorbable electronic stimulators designed to facilitate neuromuscular regeneration," *Nat Commun*, vol. 11, no. 1, pp. 1–14, Nov. 2020, doi: 10.1038/s41467-020-19660-6.
- [35] C. Kallmayer, J. Haberland, F. Schaller, F. Kayatz, T. Löher, and A. Schult, "Optimized Thermoforming Process for Conformable Electronics."
- [36] A. I. Velea *et al.*, "UV and IR Laser-Patterning for High-Density Thin-Film Neural Interfaces," *2021 23rd European Microelectronics and Packaging Conference and Exhibition, EMPC 2021*, pp. 1–8, 2021, doi: 10.23919/empc53418.2021.9584962.
- [37] D. R. Schmidt, D. M. Zwanzig, F. I. Z. M. Berlin, D. H. Moritz, and H. Lohfelden, "Gravitationsgestützte Galvanik zur Erzeugung 3- dimensional kristallin strukturierter Oberflächen," pp. 2–7.
- [38] N. B. Babaroud *et al.*, "Multilayer CVD Graphene electrodes using a transfer-free process for the next generation of optically transparent and MRI-compatible neural interfaces," 2021.



- [39] B. Fan, B. Wolfrum, and J. T. Robinson, "Impedance scaling for gold and platinum microelectrodes," *J Neural Eng*, vol. 18, no. 5, Oct. 2021, doi: 10.1088/1741-2552/ac20e5.
- [40] M. Gryszel, M. Jakešová, T. Lednický, and E. D. Głowacki, "High-Capacitance Nanoporous Noble Metal Thin Films via Reduction of Sputtered Metal Oxides," *Adv Mater Interfaces*, vol. 9, no. 5, Feb. 2022, doi: 10.1002/admi.202101973.
- [41] M. Schweigmann, F. Kirchhoff, and K. P. Koch, "Comparative study of platinum electroplating to improve micro gold electrode arrays with LCP laminate," *Biomedizinische Technik*, vol. 67, no. 1, pp. 33–42, 2022, doi: 10.1515/bmt-2021-0020.
- [42] A. Carnicer-Lombarte *et al.*, "Mechanical matching of implant to host minimises foreign body reaction," *Bioarxiv*, pp. 1–41, Nov. 2019, doi: 10.1101/829648.
- [43] D. Li *et al.*, "Thickness of fibrous capsule after implantation of hydroxyapatite in subcutaneous tissue in rats \*," pp. 2–6, 1998.
- [44] A. W. Bridges *et al.*, "CHRONIC INFLAMMATORY RESPONSES TO MICROGEL-BASED IMPLANT COATINGS," vol. 94, no. 1, pp. 252–258, 2011, doi: 10.1002/jbm.a.32669.CHRONIC.
- [45] M. Angelova, S. Asenova, and V. Nedkova, "Copper in the human organism," *Trakia Journal of Sciences*, vol. 9, no. 1, pp. 88–98, 2011.
- [46] European Food Safety Authority, "Scientific Opinion on Dietary Reference Values for copper 1," *EFSA*, vol. 13, no. 10, pp. 1–51, 2015, doi: 10.2903/j.efsa.2015.4253.
- [47] Lin *et al.*, "High-resolution and large-size stretchable electrodes based on patterned silver nanowires composites," vol. 15, no. 5, pp. 4590–4598, 2022.
- [48] Y. Khan *et al.*, "Inkjet-Printed Flexible Gold Electrode Arrays for Bioelectronic Interfaces," *Adv Funct Mater*, vol. 26, no. 7, pp. 1004–1013, 2016, doi: 10.1002/adfm.201503316.

- [49] Z. Ye, Q. Li, R. Zhang, and L. Gui, "Fabrication of a thin PDMS film with complex liquid metal electrodes embedded and its application as skin sensors," pp. 8290–8299, 2022, doi: 10.1039/d1ra09394k.
- [50] N. Adly *et al.*, "Printed microelectrode arrays on soft materials : from PDMS to hydrogels," *npj Flexible Electronics*, no. April, pp. 1–9, 2018, doi: 10.1038/s41528-018-0027-z.
- [51] S. Kang, B. Lee, S. Lee, and S. Lee, "High Resolution Micro-patterning of Stretchable Polymer Electrodes through Directed Wetting Localization," *Sci Rep*, no. August, pp. 1–8, 2019, doi: 10.1038/s41598-019-49322-7.
- [52] T. Linz, M. von Krshiwoblozki, H. Walter, and P. Foerster, "Contacting electronics to fabric circuits with nonconductive adhesive bonding," *Journal of the Textile Institute*, vol. 103, no. 10, pp. 1139–1150, 2012, doi: 10.1080/00405000.2012.664867.
- [53] P. Foerster, T. Linz, M. Von Krshiwoblozki, H. Walter, C. Kallmayer, and R. Aschenbrenner, "NCA Flip-Chip Bonding with Thermoplastic Elastomer Adhesives - Fundamental Failure Mechanisms and Opportunities of Polyurethane Bonded NCA-Interconnects," *2011 IEEE 13th Electronics Packaging Technology Conference*, pp. 223–230, Dec. 2011, doi: 10.1109/EPTC.2011.6184421.

# 5

## Integration of ASICs into TPU-based neural interfaces

### 5.1 Introduction

This chapter demonstrates the integration of thin ASICs into a TPU-based flexible electrode array. The microfabrication technology utilized for chip embedding is presented in Section 5.2. Information regarding the RFID and daisy-chain chips and their thicknesses, layouts of the substrates as well as bump size, material and height are given in Section 5.3. Section 5.4 outlines the parameters that impact the feasibility and quality of flip-chip bonding. These parameters include adhesive type, bonding time, bonding temperature, and pressure profile. The drawn conclusions and resulting demonstrators are presented in Section 5.5.

### 5.2 Fabrication process

Flip-chip bonding was utilized to integrate active electronics into the existing flexible polyurethane-based gold metallization tracks (fabricated as shown in Chapter 4, Fig. 4.1 (a-e)). Thin RFID and daisy-chain chips with a thickness of 35  $\mu\text{m}$  and 75  $\mu\text{m}$ , respectively, were flip-chip bonded to the gold tracks using an anisotropic conductive adhesive (Chapter 4, Fig. 4.1(f)). After the flip-chip bonding step, the whole structure was laminated with a 100- $\mu\text{m}$  thick PU sheet (Chapter 4, Fig. 4.1(g)), followed by the processes of copper etching (Chapter 4, Fig. 4.1(h)), second PU lamination, and PU laser patterning to expose the electrodes (Chapter 4, Figure Fig. 4.1 (i)). The used parameters for lamination and laser ablation are described in Chapter 4, Section 4.2.1).

### 5.3 RFID and daisy-chain chips and substrate layouts.

Two types of chips were used for the ASIC integration process: radio-frequency identification (RFID) and daisy-chain chips. Daisy-chain chips were chosen in order to check the validity and quality of the connection by measuring the resistance of each of the connections after bonding. At the same time, RFID chips were chosen for bonding validation and the ability to establish wireless communication with an external device (viz., an RFID reader).

A high-frequency 1.4mm x 1.4mm x 30 $\mu$ m RFID chip (ICODE, NXP Semiconductors, Eindhoven, The Netherlands) (Fig. 5.1(a)) was flip-chip bonded to the 5- $\mu$ m thick gold antenna that was electroplated on the 70- $\mu$ m thick copper substrate (layout shown in Fig. 5.1(b)). The RFID chip had electroplated copper with tin (Sn) finish bumps with 138 $\mu$ m diameter and 15 $\mu$ m thickness each. The validation of the bonding was checked by reading the signal from the bonded chip via an RFID reader.

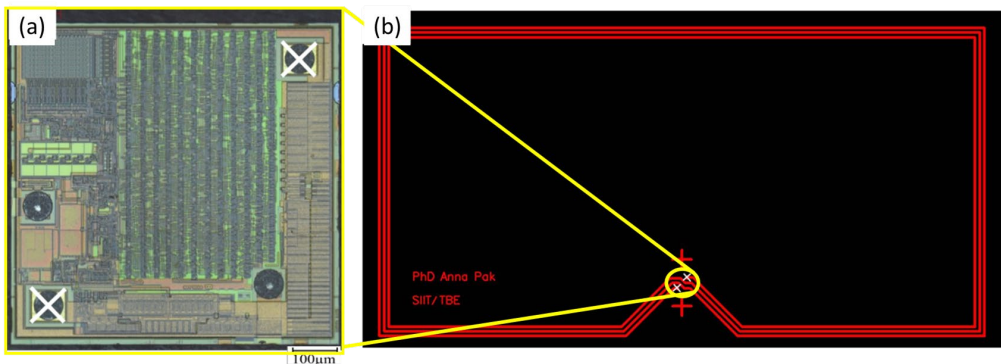


Fig. 5.1. Face-up RFID chip (a) and corresponding layout of the antenna design (b). The white crosses on the chip (a) indicate the bumps, which were bonded to antenna pads, which are also marked on the antenna with the white crosses (b).

As for the daisy-chain chip, a  $950\mu\text{m} \times 950\mu\text{m} \times 75\mu\text{m}$  chip (Fraunhofer IZM, Berlin) (Fig. 5.2(a)) was flip-chip bonded to the  $5\mu\text{m}$  thick gold complementary daisy-chain-circuitry layer electroplated on the  $70\mu\text{m}$  thick copper substrate (layout in Fig. 5.2(b)). The daisy-chain chips had electroplated copper bumps with  $85\mu\text{m} \times 105\mu\text{m} \times 5\mu\text{m}$  dimensions each. The validation of the bonding was checked by measuring the resistance between the pads, as shown in Fig. 5.2(c).

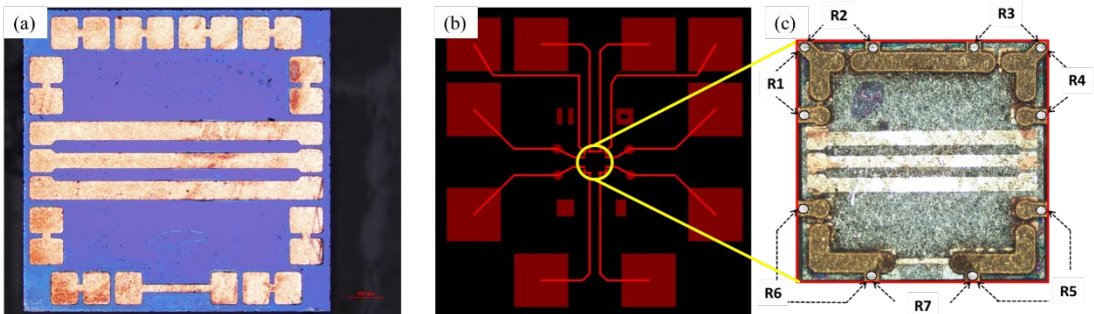


Fig. 5.2. Face-up daisy-chain chip (a), complementary substrate layout design (b), and resistance measurement points (c).

## 5.4 Bonding profiles and adhesives

An anisotropic conductive adhesive (ACA) with  $3\mu\text{m}$  gold-coated polymer sphere particles (TOSHIBA, TAP0201C) was manually applied to the substrate in the area shown with a yellow circle in Figure 5.1(b) (for the RFID chip) and a yellow circle in Figure 5.2(b) (for the daisy-chain chip). The substrate, with the adhesive, was attached to the substrate holder stage using PI tape. Before attaching the substrate with the adhesive, an additional metal plate was placed on the substrate-holder stage to flatten the surface. After that, the chip bonding was carried out on a SET FC 150 FAV flip-chip bonder (Fig. 5.3) using a  $1.5\text{ mm} \times 1.5\text{ mm}$  bonding tool head. The bonding parameters are shown in Figures 5.4 and 5.5. The temperature profile was chosen based on the data from the data sheet of the adhesive, stating that the adhesive needs about 15 s at  $180\text{ }^\circ\text{C}$  curing time. A drop in the force seen in Fig.5.4 between 25 and 40s might be due to the break of the RFID chip, as there is no record of the only functional chip (details described in Section 5.5).

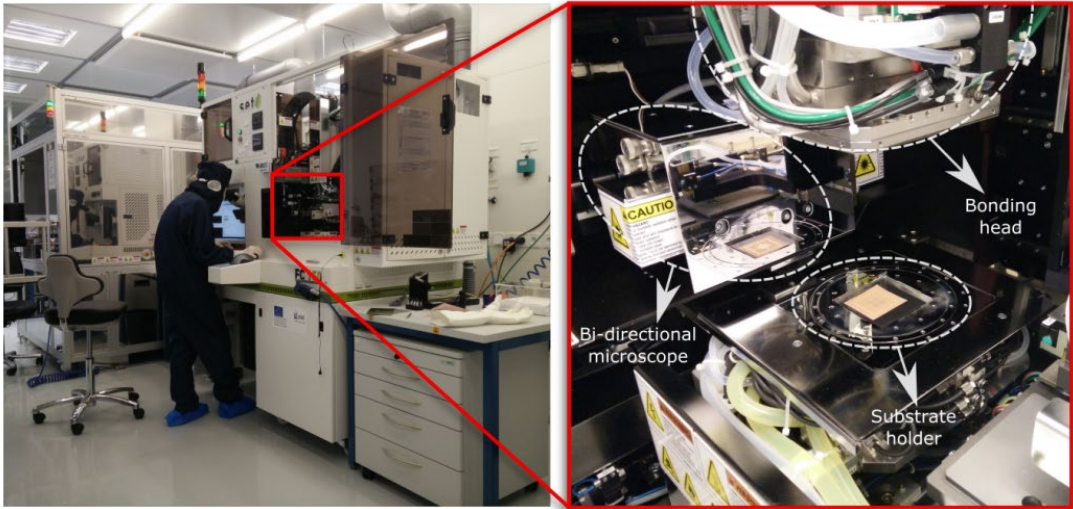


Fig. 5.3. SET FC 150 FAV flip-chip bonder. On the inset: zoomed-in image of the bonding area consisting of the bi-directional microscope for chip alignment with the substrate, bonding head for holding the chip by means of a special tool, and substrate-holder stage. Reproduced from [1].

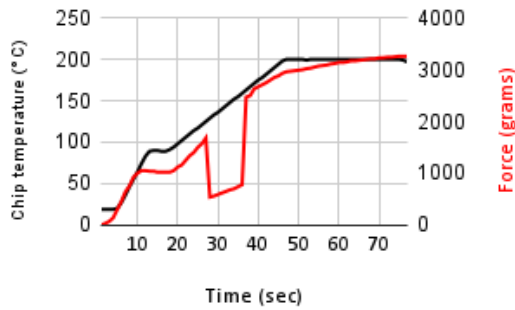


Fig. 5.4. Thermocompression bonding profile for the RFID chip flip-chip bonded to the substrate using conductive adhesive.

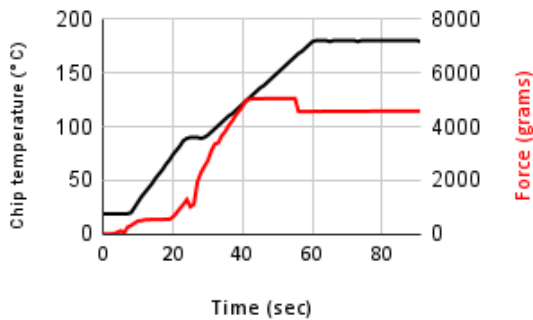


Fig. 5.5. Thermocompression bonding profile for the daisy-chain chip flip-chip bonded to the substrate using conductive adhesive.

Cross-section images of the chip bumps connected to the gold tracks are shown in Fig. 5.6 (a),(b).

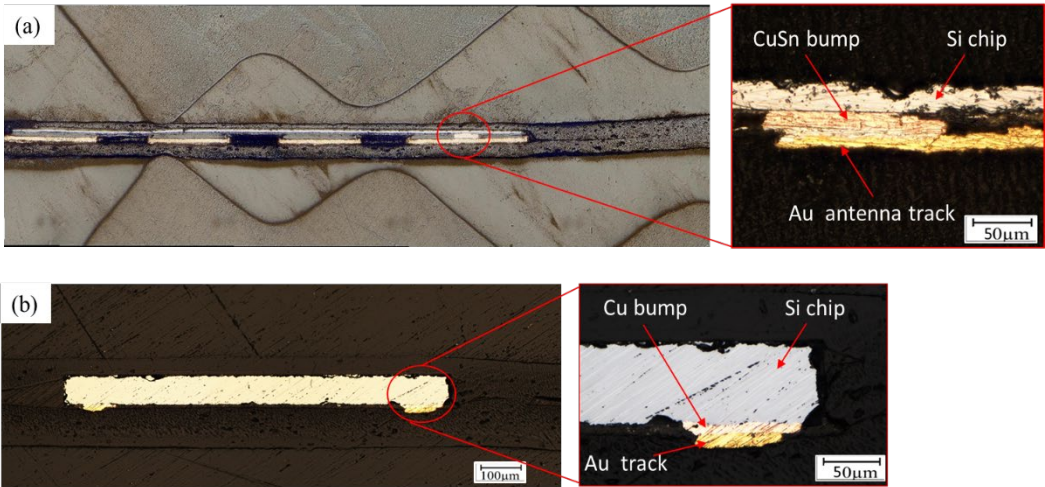


Fig. 5.6. Cross-section images of the RFID (a) and daisy-chain (b) chips with zoomed-in images of the bumps connected to the gold tracks.

## 5.5 Results and Conclusions

The demonstrators of the implemented RFID chip and the daisy chain chip are shown in Fig. 5.7(a),(b). The signal from the RFID demonstrator was successfully read during one of the first trials but unfortunately this could not be reproduced for subsequent samples. This might be due to the ageing of the chips (they were more than 10 years old) or due to a bad connection of either one or both of the bumps to the antenna. In the case of the daisy-chain demonstrator, two chips were connected successfully with 86% and 100% yield. These yields were calculated as the ratio of the number of working contacts (i.e., with a sufficiently low resistance) and the number of all contacts. Contact resistance measured between the pad points (Fig. 5.2(c)) reached the following values  $R_1 \approx 10 \Omega$ ,  $R_2 \approx 10 \Omega$ ,  $R_3 \approx 9 \Omega$ ,  $R_4 \approx 20 \Omega$ ,  $R_5 \approx \infty \Omega$ ,  $R_6 \approx 20 \Omega$ ,  $R_7 \approx 113 \Omega$ , for Chip 1, and  $R_1 \approx 17 \Omega$ ,  $R_2 \approx 7 \Omega$ ,  $R_3 \approx 7 \Omega$ ,  $R_4 \approx 93 \Omega$ ,  $R_5 \approx 40 \Omega$ ,  $R_6 \approx 135 \Omega$ ,  $R_7 \approx 640 \Omega$  for Chip 2.

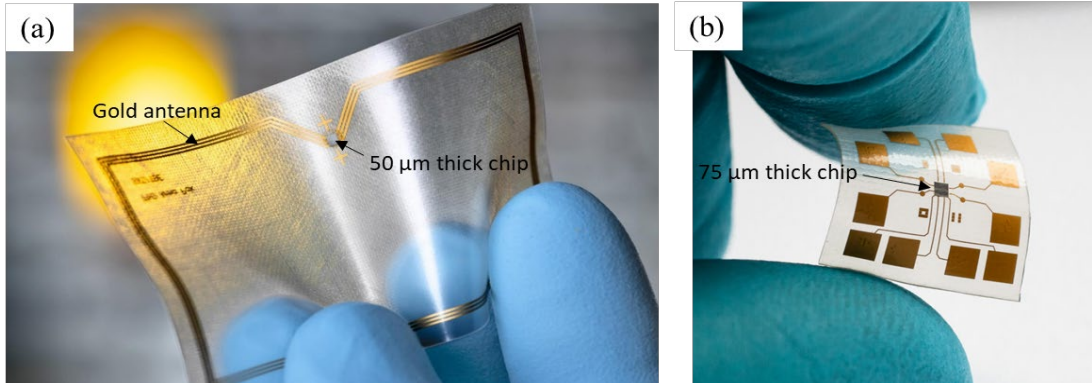


Fig. 5.7. Photos of the RFID (a) and daisy-chain chip (b) demonstrators embedded into thermoplastic polyurethane.

To conclude, chip integration into a soft, flexible neural implant prototype is a challenging task in which many parameters should be considered. A suitable flip-chip bonding technology was chosen. Since the developed process allowed for bonding using a biocompatible adhesive, it also allowed for connecting the chip to the metal tracks, which are subsequently embedded into a soft polymer substrate.

This chapter introduced the process that allows for the integration of a thin chip into a soft, flexible polyurethane medium. Using flip-chip bonding technology and a conductive adhesive, we created contacts between the 75μm thick daisy-chain chip (with 5μm thick copper electroplated bumps) and the 5μm thick gold complimentary tracks. All are embedded into a 200μm thick polyurethane layer.

In the future, the process can be improved by using TPU as an underfill material. Unsuccessful trials of using TPU as underfill (Appendix C) can be due to the fact that the bumps of the chip were too flat to pierce through the 25 μm thick polyurethane sheet and create a proper contact. Therefore, a few modifications, like using liquid PU as an adhesive and a sharper geometry of the bumps, could improve the process.

## References

- [1] T. B. Hosman, "High-density interconnect technology optimised for flexible implants [Master thesis]," Delft University of Technology, 2020. [Online]. Available: <https://repository.tudelft.nl/>.



# 6

## Conclusions

### 6.1 Conclusions

This PhD thesis presents a set of developed fabrication and encapsulation technologies in the field of neural implantable devices by utilising thermoplastic polymers. A literature overview of different polymers commonly utilised as substrate and encapsulation materials for neural implants, and outlining their main properties is given in Chapter 2. Additionally, a literature overview of various chip bonding methods and the requirements for their implementation is also presented. Furthermore, different examples of polymer-based passive and active neural implantable electrode arrays and devices with their main fabrication steps are presented in this Chapter.

Chapter 3 illustrates the encapsulation performance of thin films on an LCP substrate, namely, a  $\text{HfO}_2$ -based atomic-layer-deposition (ALD) multilayer with PDMS finish, a hybrid ParC-ALD multilayer with PDMS finish, and an LCP coating layer. The investigation of the long-term performance of these encapsulation layers revealed that thermoplastic LCP-on-LCP encapsulation is the most promising and leading to the longest lifetimes. This LCP-on-LCP encapsulation process is based on the fusion of LCP layers during lamination, preventing water ingress and water vapor condensation at the LCP-LCP interface, which is a common cause of delamination and further failure for polymer-based encapsulated devices.

Therefore, in Chapter 4, the same concept of thermoplasticity was implemented, this time on thermoplastic polyurethane (TPU), to develop a unilayer environment around the electrodes. TPU was chosen as a substrate and encapsulation material since, in comparison to LCP previously used, it is optically translucent, mechanically better matching to the host neural-tissue material, and opens up the possibility of 3D component encapsulation. The developed platform technology allows for the fabrication of TPU-embedded gold electrode arrays with tracks down to 20- $\mu\text{m}$  line-width, as

well as the implementation of nanostructured (“Shark teeth Au”) electrode surfaces. Preliminary in-vivo compatibility results are presented in Chapter 4 as well.

Chapter 5 investigates and describes the possibility of ASIC integration into the developed passive electrode-array technology by means of flip-chip bonding. Embedding of RFID and daisy chain chips demonstrates that the developed technology could enable the creation of highly integrated active microsystems tailored to specific applications.

## 6.2 Contributions

This thesis contributes to the field of implantable neural devices by providing new insights into the use of thermoplastic materials for implant development.

- The fabrication process based on merging substrate and encapsulation layers in a unibody, single-polymer layer (without a polymer-polymer interface), on the example of LCP layers, was proved to provide with long-lasting stability in wet ionic environments (Chapter 3). LCP encapsulated IDC structures were shown to remain functional for up to 28 months at 60 °C in PBS solution with a 14 V continuous DC bias, making it attractive solution for long-term encapsulation (Section 3.3.4).
- The same concept of creating a unilayer environment around the electrodes was implemented to TPU. The advantage of TPU, is its availability in a medical grade form and a long history of being utilised for chronic implants. For the first time, TPU is proposed as substrate and coating for neural interfaces.
- Integrity of the TPU merged layers stays intact after 6 month in-vivo implantation (Chapter 4, Section 4.3.1).
- A novel platform technology for the fabrication of TPU-embedded gold electrode arrays was developed (Chapter 4, Section 4.2.1). The process allows for the fabrication of high-resolution tracks on a polymer substrate, with a track width of 20  $\mu\text{m}$  and a pitch of 30  $\mu\text{m}$ , which is smaller than the resolution that can be achieved with any other reported fabrication process for such pliable and soft material (1MPa range).

- A novel process that allows a nanostructured, so-called “Shark teeth Au” electrodes surface was developed. The process is based on electroplating and does not require any costly sputtering machines or masks. The resulting polyurethane-based microelectrodes has exhibited low impedance (1.67 k $\Omega$  at 1kHz) and high charge injection capacity (0.137 mC/cm<sup>2</sup>) (Chapter 4, Section 4.3.2).
- The integration of thin electronics into the soft and flexible polyurethane environment was demonstrated by flip-chip bonding of a 75- $\mu$ m thick daisy-chain chip (with 5- $\mu$ m thick copper electroplated bumps) to a 5- $\mu$ m thick gold complimentary tracks, all embedded into 200- $\mu$ m thick polyurethane layer. Functionality of such an active prototype was proven by contact resistance measurements.

Overall, this thesis is adding TPU to a portfolio of biocompatible polymers used as substrate and encapsulation materials for soft neural interfaces. This approach has also all the prerequisites to prolong the lifetime of the implant by mitigating the issues related to water ingress and condensation at the polymer-polymer interface. The findings of this work have the potential to improve the performance and reliability of biomedical implants, ultimately leading to better patient outcomes and quality of life.

### 6.3 Recommendations

Thermoplastic polymers, such as LCP and TPU, have a high potential for being used as substrate and encapsulation materials for neural implantable devices. This thesis brings them one step closer to adding them to the portfolio of biocompatible polymers used for commercial neural implants. Thus, the following steps can be further taken to improve their long-term stability and biocompatibility.

1. Pre-treatment of the TPU to improve TPU-gold adhesion. Long-term soak tests (described in Sections 4.2.2 and 4.3.1) showed that with time gold starts to delaminate from TPU. Although this might not completely damage the track, it will still be able to conduct, and complete merging of the surrounding TPU layers will keep it in place, in the long term, it might lead to corrosion and track damage. Plasma treatment is known to improve metal adhesion to polymers [1].

Ionised species and free radicals present in plasma remove organic contamination from the polymer surface. Plasma treatment modifies the polymers' surface, making it oxidised and activated by the formation of polar functional groups such as hydroxyl, carbonyl or carboxylic acid, and improves the wetting properties, which results in better coating spreading to fill the voids on the polymer surface for better bonding. Argon bombardment leads to roughening of the surface, which in turn increases the contact area of the coating to polymer and results in better interlocking between the two. Therefore, initial trials of oxygen-plasma pre-treatment of TPU to improve gold adhesion to it were performed. Unfortunately, the results were inconclusive, and further optimisation of the pre-treatment materials and methods is required.

2. Chip-TPU adhesion testing. Adhesion between the TPU and the passivation layer of the chip must be evaluated. Long-term soak and cross-hatch tests could be performed for that. If required, plasma or chemical etching of the TPU and/or chip could be tested to improve the adhesion.
3. Utilising curved, instead of straight, lines to improve the mechanical properties of the electrode array. Increased curvature and line thickness contribute to the higher stretchability of the array. An optimised geometry shall be selected and tailored depending on the final aim and location of the device. Buckled, coiled spring [2], and non-coplanar serpentine bridge configurations [3] can be considered for achieving higher stretchability.
4. Eliminating the copper sacrificial substrate. Although the amount of copper found on the surface of the fabricated prototype is minimal, and successive in-vivo evaluation of these prototypes did not reveal any harmful reactions for the body (Section 4.3.3.1), copper remains a toxic and unwanted material in implantable devices. Future research could involve testing titanium or other biocompatible metal seed layers as a substrate for gold electroplating.
5. Chips with higher (not flat) bumps. Bonding with TPU as a non-conductive adhesive requires piercing with the chip bumps through the TPU film. Results obtained during experiments (presented in Appendix C) showed that chips with bumps of the following

dimensions, viz. 138  $\mu\text{m}$  diameter and 15  $\mu\text{m}$  thick (for the RFID chip) and 85  $\mu\text{m}$  x 105  $\mu\text{m}$  x 5  $\mu\text{m}$  size (for the daisy chain chip), were not able to pierce through 100- $\mu\text{m}$  thick TPU and to establish proper electrical contact to the substrate tracks, although a high temperature, which is able to melt the TPU, was applied. This can be attributed to the lack of optimal pressure necessary to establish electrical contact and at the same time not breaking the chip. This can be seen from the cross-section image and the existing gap between the gold track and the bump (Appendix C, Fig. C.1. and Fig.C.2.). Therefore, chips with higher, non-flat bumps that will be able to pierce through TPU more easily. Also, the use of liquid-form (not film-form) TPU is recommended.

6. Replacing the currently used TPU for a medical-grade one. Despite the promising biocompatibility results obtained from the in-vivo tests (Section 4.3.3.1), the TPU Platilon AU 4201 (Covestro) is not classified as medical-grade. But Bionate 80A (DSM Biomedical) used in in-vivo experiments (Section 4.2.5) is a medical-grade version of TPU used in long-term implants. Bionate 80A comes in the form of pellets and therefore requires extra process steps to obtain it in sheet form. This process will require the dissolution of pellets in organic solvent (DMAc, DMF, or THF), followed by spin coating of the solution to the desired thickness and solvent evaporation.
7. Use of TPU as underfill material. Generally, an active implant would consist of the following parts depicted in Figure 6.1. Overall, it has about six different interfaces. In the case of non-hermetic implants, all these interfaces can be critical points, leading to water condensation and further propagation of the water and future failure of the device. One can and should work on improving adhesion between these surfaces, and the other solution can be decreasing the number of these interfaces. When choosing TPU as a polymer for such an implant prototype, as was proposed in Chapter 4 of this thesis, due to its thermoplastic nature, one can reduce the number of interfaces within the implant from six to five by getting rid of the polymer-polymer interface (interface number 6 in Fig.6.2). Furthermore, it is possible to reduce the number of interfaces from five to two by introducing PU as an underfill material (Fig.6.3). This

would allow us to focus and need to optimise only the polymer-metal and polymer-chip interface. Some successful examples of using TPU as underfill for chip bonding are presented in the following works [4], [5]. Using TPU as an adhesive will drastically reduce the amount of work that has to be done on adhesion improvement, significantly simplifying the design of robust active neural interfaces. The challenges of using PU as underfill material are as follows: 1) it is a non-conductive material; therefore, the direct electrical contact between the pad and the bump must be established 2) it has a relatively low softening temperature, starting from 155 °C, making it vulnerable to further steps with high-temperature processing.

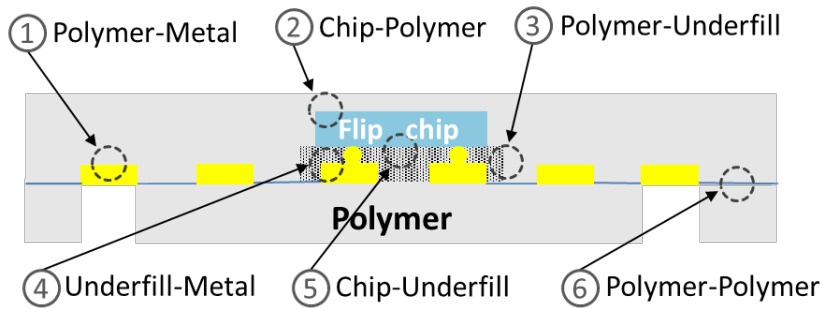


Fig. 6.1. Schematic cross-section illustration of the active implant prototype with the major components (6 interfaces).

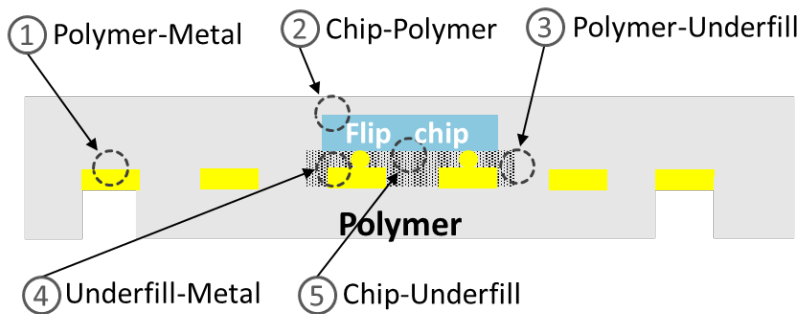


Fig. 6.2. Schematic cross-section illustration of the active implant prototype with the PU used as substrate and encapsulation material (5 interfaces).

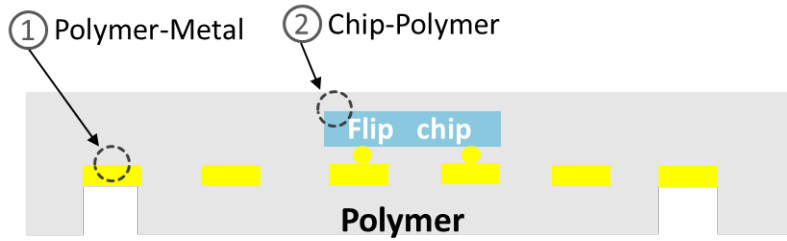


Fig. 6.3. Schematic cross-section illustration of the active implant prototype with the PU used as substrate, encapsulation, and underfill material (2 interfaces).

## References

- [1] C. Lambaré, P. Y. Tessier, F. Poncin-Epaillard, and D. Debarnot, "Plasma functionalization and etching for enhancing metal adhesion onto polymeric substrates," *RSC Adv*, vol. 5, no. 77, pp. 62348–62357, Jul. 2015, doi: 10.1039/c5ra08844e.
- [2] W. L. Sung, C. C. Chen, K. Huang, and W. Fang, "Development of a large-area chip network with multidevice integration using a stretchable electroplated copper spring," *Journal of Micromechanics and Microengineering*, vol. 26, no. 2, pp. 25003–25018, Dec. 2015, doi: 10.1088/0960-1317/26/2/025003.
- [3] D.-H. Kim *et al.*, "Materials and noncoplanar mesh designs for integrated circuits with linear elastic responses to extreme mechanical deformations," *PNAS December*, vol. 105, no. 48, pp. 18675–18680, Sep. 2008, doi: 10.1073/pnas.0807476105.
- [4] P. Foerster, T. Linz, M. Von Krshiwoblozki, H. Walter, C. Kallmayer, and R. Aschenbrenner, "NCA Flip-Chip Bonding with Thermoplastic Elastomer Adhesives - Fundamental Failure Mechanisms and Opportunities of Polyurethane Bonded NCA-Interconnects," *2011 IEEE 13th Electronics Packaging Technology Conference*, pp. 223–230, Dec. 2011, doi: 10.1109/EPTC.2011.6184421.
- [5] T. B. Hosman, "High-density interconnect technology optimised for flexible implants [Master thesis]," Delft University of Technology, 2020. [Online]. Available: <https://repository.tudelft.nl/>.

# Appendix A

## Experimental Materials for Chapter 4.

Lamination of the patterned gold electroplated on copper substrate to the TPU with the FR4-TPU-PTFE-impregnated glass cloth stack, as shown in Fig. 4.1 (g) for the array with the chip, and in Fig. 4.1 (h1) for the array without the chip. Lamination via thermocompression bonding was performed in the lamination press (MP30-VK-S, HML Haseneder Maschinenbau e.K.). Lamination profile is depicted below.

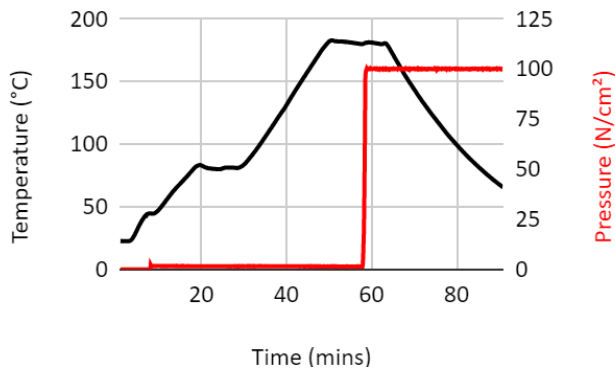


Fig. A.1. Lamination bonding profile for the 1<sup>st</sup> lamination step (Fig. 4.2 (g,f1)) at 180 °C.

Next lamination step was performed to cover exposed gold structures (Fig.4.3(h1)), as well as the chip (Fig.4.3(i)),

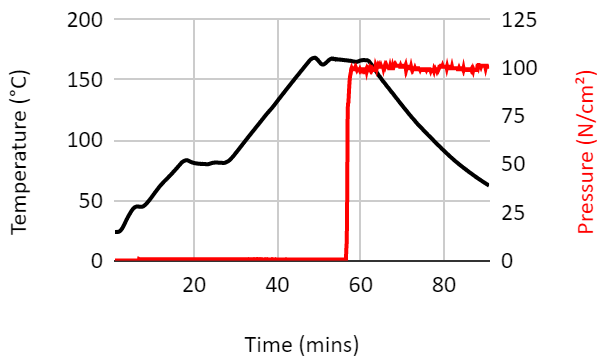




Fig. A.2. Lamination bonding profile for the 2<sup>nd</sup> lamination step (Fig. 4.2 (i,h1)) at 165 °C, The same lamination profile was used for bonding two or five TPU sheets shown in figure 4.3(b-d; f-h).

Lamination profile that does not allow TPU sheets merge is depicted in Fig. A.3, Cross-sectional images of existing TPU-TPU interface is illustrated in Fig. 4.2(a,e) and

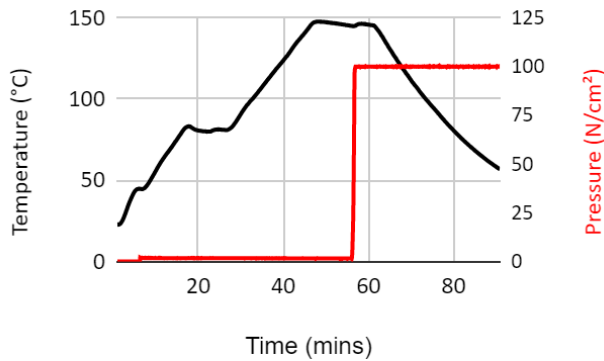


Fig. A.3. 2<sup>nd</sup> lamination step, profile for two non-merged TPU sheets laminated at 145 °C, cross-sections shown in Fig. 4.2(a,e).

Following the 2<sup>nd</sup> lamination step, electrode openings were performed on a picosecond laser (more details are given in Section 4.2.1). During laser ablation, due to the heat produced by the laser, TPU located on the borders of the opened circumference would melt and reflow, decreasing the actual exposed electrode diameter. The actual electrode diameter was calculated using optical microscopy images of the openings and compared to the diameter set on the laser. Results of the measurements are presented below:

Electrode	Set diameter	Actual diameter
Base Au 700 μm	700 μm	620 μm
Base Au 300 μm	300 μm	250 μm
Shark teeth Au 700 μm	700 μm	653 μm

Table A.1. Comparison table depicting the difference between the diameter set on the laser and the actual electrode opening diameter due to TPU melting and reflowing on the edges of the circumference during the laser ablation step.

Layout sketch of the gold tracks embedded in polyurethane and submerged in PBS and placed in a humidity chamber set to 37 °C is shown in Fig. A.4. Microscopy images of the delamination initiation for the different lines widths are presented below in Fig. A.4(b-d)..

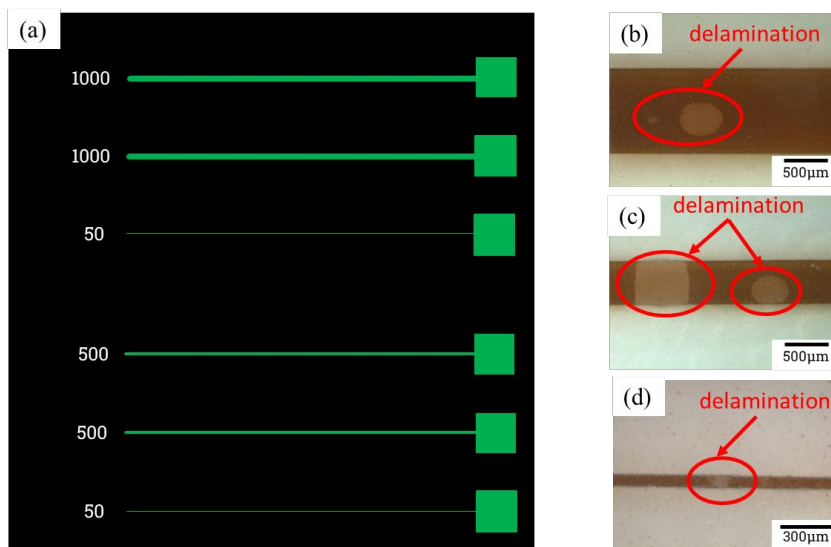


Fig. A.4. Layout sketch of the gold tracks of 1000, 500, 50  $\mu\text{m}$  lines widths used for accelerated ageing tests embedded in polyurethane soaked at 37 °C (a). Examples of the first delamination started at day 100 (b), 100 (c), 37 (d) for line's widths 1000, 500, 50  $\mu\text{m}$ , respectively.

Details of the in-vivo implantation aimed to evaluate biocompatibility of the fabricated bioelectronic foils is presented below.

Animal code	Rat P1		Rat P2		Rat P4	Rat P5	Rat P3		Rat P6
Implant code	Sample 1	Sample 2	Sample 5	Sample 6	Sample 4	Sample 8	Sample 9	Sample 10	Sample 12
Side	left	right	left	right	right	right	left	right	right
Material	Bionate	Platilon	Bionate	Platilon	Platilon Au	Platilon Au	Bionate	Platilon	Platilon Au
Surviving	2 months		4 months		5.5 months	6 months	9.5 months		9.5 months
Number of animals	1	1	1	1	1	1	1	1	1
Number of implants	1	1	1	1	1	1	1	1	1
Number of measuring points (n)	74	85	136	93	56	60	103	61	110
Thickness of the encapsulating tissue ( $\mu\text{m}$ )	181 [147 – 252]	111 [73 – 171]	155 [106 – 195]	214 [170 – 257]	123 [101 – 147]	263 [218 – 371]	188 [126 – 318]	162 [112 – 228]	168 [116 – 228]
Implantation	Easily implanted	A bit more difficult	Easily implanted	Easily implanted	Big wound, easily implanted.	Easily implanted	Bit bigger wound, easily implanted.	Easily implanted	Easily implanted

Table A.2. Implantation data for pure Platilon PU, Platilon PU with gold tracks and for medical grade Bionate 80A PU. Thickness values are given in median [1<sup>st</sup> – 3<sup>rd</sup> quartiles].

# Appendix B

## Mechanical characterization of the TPU-Au structures with different line geometries

Mechanical characterization of the TPU-Au structures was performed to ascertain their tolerance to stretching and evaluate how different line geometries could influence the stretching ability. Gold tracks embedded in TPU were fabricated as described in Section 4.2.1 (Fig.4.2(a-h1)), except that in step (g1) instead of PTFE-impregnated glass cloth, Teflon sheet was used. The lines design is shown in Fig.B.1(a). Three different line widths: 100, 200, and 300  $\mu\text{m}$ , and four different line geometries: straight (Fig.B.1(b)), slightly wavy (Fig.A.1(c)), curvy (Fig.A.1(d)), and meander shape lines (Fig.B.1(e)) were used for the tests. The experiments were performed by stretching the fabricated samples fixed in the tensile stretcher (Fig.B.1(f)) and measuring their resistance with the connected multimeter. The samples were crimped, as shown in the zoomed-in insert of the Fig.B.1(f), in order to establish contact between the multimeter measuring probes and the sample.

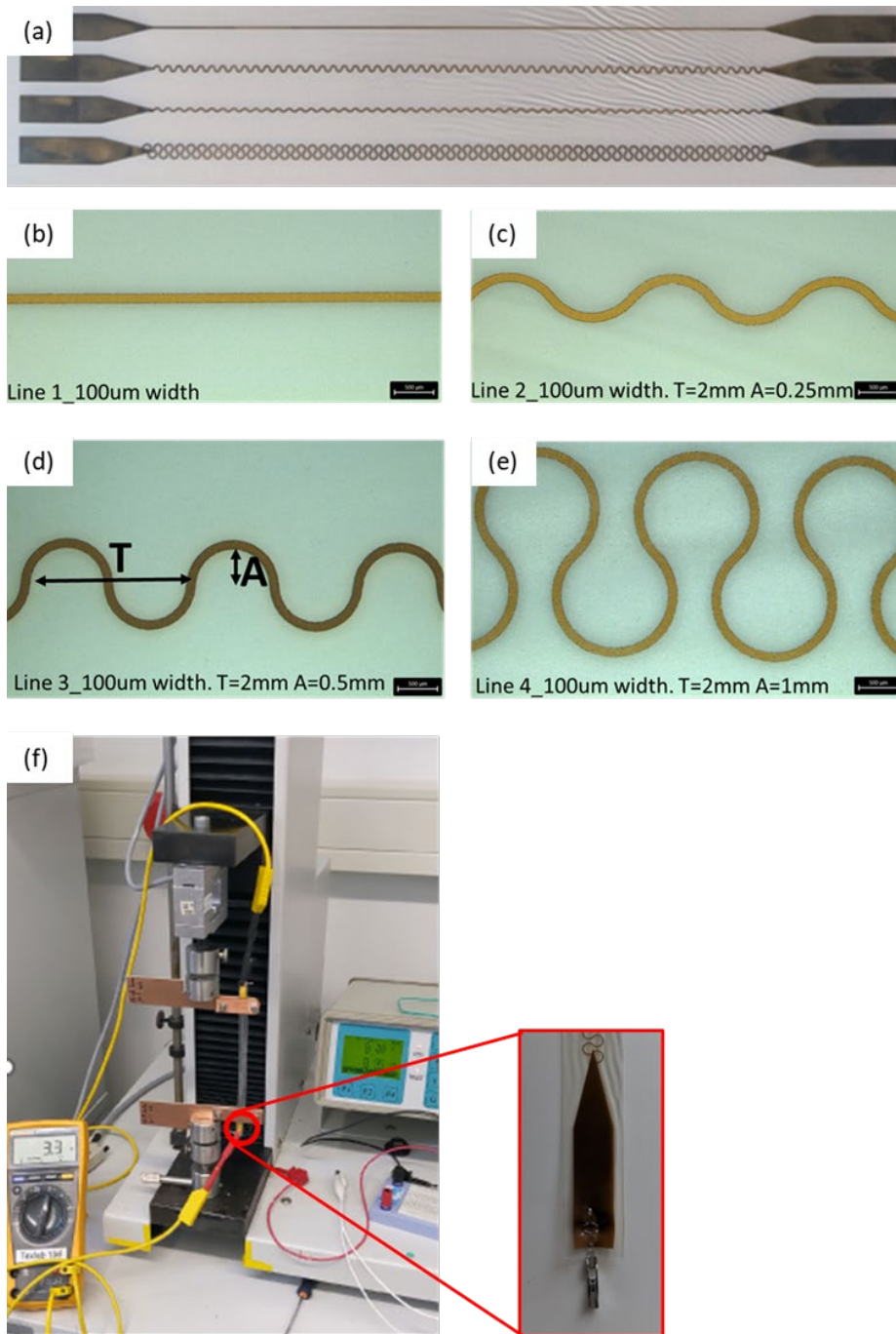


Fig. B.1. (a) design of four different gold track lines used for tensile stretching test: (b) straight line, (c) slightly wavy line, (d) curvy line, (e)

meander shape line. (f) Tensile stretching test setup with the fixed testing sample connected to the multimeter. On the inset: crimping of the sample. The measured results of the tensile stretching tests are presented below in Table B.1.

Line width	Line shape	Resistance	Initial + max. stretching length
100 $\mu\text{m}$	straight	4.8 $\Omega$	not known
100 $\mu\text{m}$	slightly wavy	$\infty$	broke while clamping
100 $\mu\text{m}$	curvy	7 $\Omega$	10 cm + 5 mm
100 $\mu\text{m}$	meander	$\infty$ , due to wrinkling of TPU	-
200 $\mu\text{m}$	straight	2.6 $\Omega$	10 cm + 5 mm
200 $\mu\text{m}$	slightly wavy	3.5 $\Omega$	broke while clamping
200 $\mu\text{m}$	curvy	$\infty$ , due to wrinkling of TPU	-
200 $\mu\text{m}$	meander	$\infty$ , due to wrinkling of TPU	-
300 $\mu\text{m}$	straight	4.6 $\Omega$	10 cm + 3.17 mm
300 $\mu\text{m}$	slightly wavy	2.5 $\Omega$	10 cm + 6.5 mm
300 $\mu\text{m}$	curvy	$\infty$ , due to wrinkling of TPU	-
300 $\mu\text{m}$	meander	11.4 $\Omega$	10 cm + 7.5 mm

Table B.1. Results of the tensile stretching tests performed with different gold tracks widths and geometries embedded in TPU.

Due to the use of a Teflon sheet instead PTFE-impregnated glass cloth in the support stack, the TPU got wrinkled, as seen on the Fig B.1 (a). This also caused some implications to the gold lines (Table B.1: 100  $\mu\text{m}$  width meander shape gold track, 200  $\mu\text{m}$  width curvy and meander shape gold track, 300  $\mu\text{m}$  width curvy shape gold track), where no resistance was measured. In result, we could stretch 100  $\mu\text{m}$  width curvy line to up to 5%, 200  $\mu\text{m}$  width straight line to up to 5%. While, 300  $\mu\text{m}$  straight line was stretched to up to 3.17%, 300  $\mu\text{m}$  slightly wavy line was stretched to up to 6.5% and 300  $\mu\text{m}$  meander line

was stretched to up to 7.5% showing an increasing stretching trend in relation to the curviness of the lines. Overall, more tests are required to get more conclusive results.

# Appendix C

## Flip-chip bonding using TPU as a non-conductive adhesive

A number of attempts were made to embed thin chips into flexible gold-microelectrode arrays using TPU as non-conductive adhesive. Such kind of bonding requires piercing with the chip bumps through the TPU film in order to establish physical contact between the gold track and the chip's bump. All the samples were fabricated as described in Section 4.2.1 and schematically illustrated in Fig.4.2 (a-i), except for the fact that instead of anisotropic conductive adhesive (ACA) (Fig.4.2(f)) a 25- $\mu\text{m}$  thick TPU film, cut in a square with the side length equal to the side length of the chip + 50 to 300  $\mu\text{m}$  was used as an adhesive. The TPU film pieces were cleaned with isopropanol (IPA) and then dried for about 30 mins, to allow the moisture evaporate from it.

1.4 mm x 1.4 mm x 30  $\mu\text{m}$  RFID chips with four 105  $\mu\text{m}$  x 85  $\mu\text{m}$  x 5  $\mu\text{m}$  bumps each, were flip-chip bonded using 200, 250, 300, 735, 1470, 2940 grams force and the temperatures of 180 and 200 °C. Since there is very limited amount of literature available on the use of TPU as a conductive adhesive, and no literature review of using TPU with such thin chips, pressure and temperature parameters were selected and tested by trial and failure. Few available literature sources [1], [2] were used as a guidance, although the parameters found in those reference did not include into consideration very thin thickness of the chips, as in our case.

Results obtained during the experiment are presented below. It was not possible to establish proper electrical contact between the chip's bumps and the substrate track. This can be seen from the cross-section image and the existing gap between the gold track and the bump (Fig. C.1 and Fig.C.2). As the used temperature that is able to melt PU was applied, the inability to establish the contact can be attributed to the lack of optimal pressure



necessary to establish electrical contact and at the same time not breaking the chip (Fig.C.3).

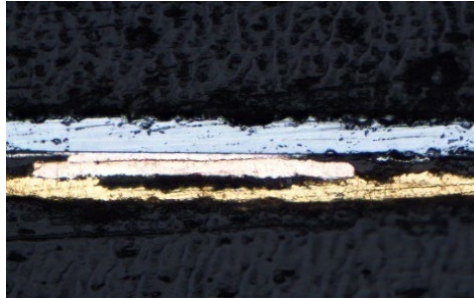


Fig. C.1. Zoomed-in cross-section image of the bump of the RFID chip connected to the gold track using TPU as adhesive – no contact achieved (200g. force).



Fig. C.2. Cross-section image of the bump of the RFID chip connected to the gold track using TPU as adhesive – no contact achieved (735 g.).

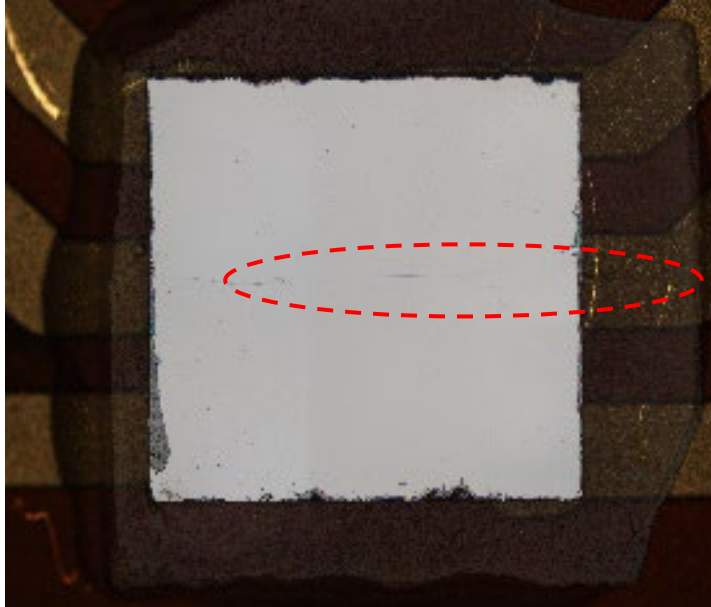


Fig. C.3. RFID chip with the single crack (a) (1470 g.)

Further experiments required to enable bonding of thin chips using TPU as adhesive. In the future, chips with higher, non-flat bumps that will be able to pierce through TPU more easily are recommended. Also, the use of liquid-form (not film-form) TPU could facilitate the bonding.

## References

- [1] T. B. Hosman, "High-density interconnect technology optimised for flexible implants [Master thesis]," Delft University of Technology, 2020. [Online]. Available: <https://repository.tudelft.nl/>.
- [2] P. Foerster, T. Linz, M. Von Krshiwoblozki, H. Walter, C. Kallmayer, and R. Aschenbrenner, "NCA Flip-Chip Bonding with Thermoplastic Elastomer Adhesives - Fundamental Failure Mechanisms and Opportunities of Polyurethane Bonded NCA-Interconnects," *2011 IEEE 13th Electronics Packaging Technology Conference*, pp. 223–230, Dec. 2011, doi: 10.1109/EPTC.2011.6184421.

# List of Figures

1.1 Schematic cross-section illustration of an active implant prototype with its major components and indicated polymer-polymer interface. ....	2
1.2 Schematic illustration of the change in the intermolecular structure of a thermoset polymer happening at high temperatures Comparative table of the different types of bumps with their properties .....	3
1.3 Schematic illustration of the change in the intermolecular structure of a thermoplastic polymer happening at high temperatures .....	4
2.1 The phases of the Foreign Body Reaction to the implant .....	10
2.2 Graphical and tabular representation of the elastic modulus matching of various biological tissues to different materials used as substrate materials for neural implants.....	12
2.3 PDMS chemical structure .....	13
2.4 Chemical structure of PI 2616.....	14
2.5 ParC chemical structure.....	14
2.6 Chemical structure of PU (Ether) .....	15
2.7 Chemical structure of LCP.....	16
2.8 SU-8 chemical structure .....	17
2.9 Water ingress mechanisms: (a) contamination or (b) void formation due to loss of adhesion happening at the polymer-polymer interface .....	20
2.10 Polymer-polymer interface of thermoset polymers treated with different techniques aimed to improve adhesion: PDMS-PDMS interface after (a) corona discharge and (b) piranha solution treatment, and (c), (d) PI-PI interfaces after plasma treatment,. In the red dotted circles, the PDMS-PDMS (a,b) and PI-PI interfaces (c,d) are highlighted. ....	21
2.11 ParC-ParC delamination after annealing.....	22
2.12 Schematic illustration of the self-bonding and merging of bioresorbable dynamic covalent polyurethane (b-DCPU) layers induced by heat without the use of any adhesives. A cross-sectional SEM image of the thinned LCP electrode array after thermocompression bonding .....	23

2.13 Examples of passive electrode arrays on flexible thin-film substrates. Polymer materials and implantation times of the given examples are as follows: (a) Par C, 6 months, (b) PI, 4.5 months, (c) PI, 4 weeks, (d) SU-8, PI, 15 weeks, (e) PDMS, 5 weeks, (f) PDMS, 3 months, (g) LCP, 158 days at 87 °C PBS.....	27
2.14 Sketches of ball-wedge (a) and wedge-wedge (b) wire-bonding techniques .....	29
2.15 Various bonding techniques used for chip interconnection: (a) wire bonding, (b) tape automated bonding, (c) flip-chip interconnection. ....	31
2.16 Schematic illustration of the stud bumping process fabricated using thermosonic bonding. Reproduced from .....	32
2.17 Schematic illustration of the electroplated under-bump-metallisation and solder-bump process. Reproduced from .....	33
2.18 Schematic illustration of the electroless-nickel-immersion-gold (ENIG) bumping process.....	34
2.19 Schematic illustration of different adhesive types: isotropic conductive adhesive (a), anisotropic conductive adhesive (b), and non-conductive adhesive (c).....	36
2.20 Examples of active electrode arrays with the schematics on the left side and the photo illustration on the right: (a) PI-based epiretinal visual prosthesis, (b) ParC embedded flexible antenna with a rectifier chip for wireless power transmission, (c) PDMS-based optogenetic system for wireless optogenetics, (d) Neuralink's brain-machine interface for wireless recording and streaming of action potentials, (e) Wirelessly-controlled neural stimulator .....	40
3.1 Generic sketch of a wirelessly-powered, fully-implantable active device based on a polymer substrate: electronic components in the form of a capacitor and ASIC constituting the functional circuit; metal electrodes for delivering or receiving signals to/from the tissue; coil for wireless communication and power transmission. All are implemented into a flexible biocompatible polymer covered with a thin film encapsulation (TFE) layer .....	49
3.2 Schematic cross-section illustration of the tested samples: (a) LCP-TFE1/2 samples used for the pre-screening test, (b) LCP-LCP laminate, and	

(c) LCP-TFE1/2 with silicone finish samples used for sorption tests, LCP-LCP (d) and LCP-TFE1/2 (e) with silicone finish samples used for adhesion T-Peel test. Adapted ASTM D1876 T-Peel test setup with the sample (f). Schematic representation of the IDC tested samples: LCP-Au-LCP (g) and LCP-Au-TFE1/2 with silicone finish (h). Exposed Au IDC test structure on LCP (i). ..... 53

3.3 SEM images of bare LCP (a) and LCP coated with a 100 nm thick HfO<sub>2</sub> - based ALD ML (TFE1) (b). Cross-sectional TEM images of 100 nm HfO<sub>2</sub> - based ALD ML on LCP: (c) before soak; (d) after two months soaking in PBS at 67 °C..... 58

3.4 Fig. 3.4. SEM images of LCP (a,c) and PDMS (b,d) surfaces after T-Peel test before and after soaking..... 60

3.5 The lifetime of different coatings on LCP substrates with Au IDCs in PBS at 60 °C. The end of a sample's lifetime was indicated by a >10% deviation of the impedance magnitude at 0.1 Hz, compared to the original value at the beginning of the ageing study. Red asterisks (\*) represent failed samples in the corresponding months..... 61

4.1 Schematic step-by-step cross-section representation of the platform TPU-based embedding technology. For the active prototypes: after step (e), the process continues in the left column (f-h). For passive electrode arrays: after step (e), the process continues in the right column (f1-h1) ..... 74

4.2 Cross-section image of two non-merged TPU sheets with existing interface laminated under non-optimised parameters (a); cross-section of two completely merged TPU sheets directly after lamination (b) and after 100 days soak in PBS at 37 °C (c); cross-section of five completely merged TPU sheets after six months of implantation (d). 2xTPU and 4xTPU indicating two and four merged TPU layers. Cross-section of two non-merged TPU sheets around the gold track with existing interface laminated under non-optimised parameters (e); cross-section of two completely merged TPU sheets with embedded gold track directly after lamination (f) and after 100 days soak in PBS at 37 °C (g); cross-section of five completely merged TPU sheets around the gold track after six months of implantation (h)..... 79

4.3 SEM images of (a) “Base Au” and (b) nanostructured “Shark teeth Au” electroplated gold. (c) Impedance magnitude and (d) phase angle plots for 700  $\mu\text{m}$  “Base Au”, 300  $\mu\text{m}$  “Base Au”, and 700  $\mu\text{m}$  “Shark teeth Au” electrodes. (e) Cyclic voltammograms (50mV/s scan rate) and (f-h) voltage transient measurements for the same gold electrodes.....82

4.4 Polyurethane sample with embedded gold electrodes before (a) and after 9 months of implantation, seen from the top (b) and bottom (c), together with the zoomed-in image of the electrodes of 700  $\mu\text{m}$  and 300  $\mu\text{m}$  diameter (d,e), showing no damage to the electrode after the implantation. Surgical implantation of the TPU samples underneath the skin at the back of the rat (f). Histological H&E image of the encapsulating connective tissue formed around the implanted sample (g). Thicknesses of the encapsulating connective tissue for pure Plaitlon TPU and Plaitlon TPU with gold electrodes (h) (\* $p$ <0.001, \*\* $p$ =0.03, \*\*\* $p$ <0.001) vs. pure Bionate polyurethane (i) ( \* $p$ =0.007, \*\* $p$ <0.001) analysed with the Mann-Whitney U test (when comparing two independent samples) or the Kruskal-Wallis H test (when comparing more than two independent samples) with the Bonferroni adjustment. The box plots also indicate the mean (cross sign), and the median (horizontal line inside the box). Elemental analysis of the four TPU samples (j): non-implanted, 15 minutes ultrasonicated (Sample 1), non-implanted not ultrasonicated (Sample 2), 5 months implanted (Sample 3) and 9 months implanted (Sample 4). Optical transmittance of the Plaitlon and Bionate TPU samples, before and after nine months of implantation (k). .....84

4.5 TPU-based flexible neural implant’s prototypes: (a) cross-section of the daisy chain chip connected to the gold tracks, (b) daisy-chain chip connected to corresponding gold tracks, (c) silicon chip embedded in bioelectronic foil with gold antenna, (d) thinned dummy chip embedded in bioelectronic foil intended for peripheral nervous system, (e) high-density implant prototype for central nervous system with 324 electrodes (e).....87

5.1 Face-up RFID chip (a) and corresponding layout of the antenna design (b). The white crosses on the chip (a) indicate the bumps, which were bonded to antenna pads, which are also marked on the antenna with the white crosses (b).....97

5.2 Face-up daisy-chain chip (a), complementary substrate layout design (b), and resistance measurement points (c) .....	98
5.3 SET FC 150 FAV flip-chip bonder. On the inset: zoomed-in image of the bonding area consisting of the bi-directional microscope for chip alignment with the substrate, bonding head for holding the chip by means of a special tool, and substrate-holder stage .....	99
5.4 Thermocompression bonding profile for the RFID chip flip-chip bonded to the substrate using conductive adhesive.....	99
5.5 Thermocompression bonding profile for the daisy-chain chip flip-chip bonded to the substrate using conductive adhesive .....	99
5.6 Cross-section images of the RFID (a) and daisy-chain (b) chips with zoomed-in images of the bumps connected to the gold tracks .....	100
5.7 Photos of the RFID (a) and daisy-chain chip (b) demonstrators embedded into thermoplastic polyurethane .....	101
6.1 Schematic cross-section illustration of the active implant prototype with the major components (6 interfaces) .....	107
6.2 Schematic cross-section illustration of the active implant prototype with the PU used as substrate and encapsulation material (5 interfaces) .....	107
6.3 Schematic cross-section illustration of the active implant prototype with the PU used as substrate, encapsulation, and underfill material (2 interfaces).....	108
A.1 Lamination bonding profile for the 1 <sup>st</sup> lamination step (Fig. 4.2 (g,f1)) at 180 °C .....	109
A.2 Lamination bonding profile for the 2 <sup>nd</sup> lamination step (Fig. 4.2 (i,h1)) at 165 °C, The same lamination profile was used for bonding two or five TPU sheets shown in figure 4.3(b-d; f-h) .....	109
A.3 2 <sup>nd</sup> lamination step, profile for two non-merged TPU sheets laminated at 145 °C, cross-sections shown in Fig. 4.2(a,e) .....	110
A.4 Layout sketch of the gold tracks of 1000, 500, 50 µm lines widths used for accelerated ageing tests embedded in polyurethane soaked at 37 °C (a). Examples of the first delamination started at day 100 (b), 100 (c), 37 (d) for line's widths 1000, 500, 50 µm, respectively .....	111

B.1 (a) design of four different gold track lines used for tensile stretching test: (b) straight line, (c) slightly wavy line, (d) curvy line, (e) meander shape line. (f) Tensile stretching test setup with the fixed testing sample connected to the multimeter. On the inset: crimping of the sample .....	114
C.1 Zoomed-in cross-section image of the bump of the RFID chip connected to the gold track using TPU as adhesive – no contact achieved (200g. force) .....	118
C.2 Cross-section image of the bump of the RFID chip connected to the gold track using TPU as adhesive – no contact achieved (735 g.) .....	118
C.3. RFID chip with the single crack (a) (1470 g.) .....	119



# List of Tables

2.1 Comparison of the material properties of polymers used for fabrication of neural implants.....	18
2.2 Comparative table of the different types of bumps with their properties.....	35
3.1 WVTR of the coatings measured with a Sorption Analyser at 60 °C and 60 % relative humidity .....	58
3.2 Peel force required to compromise the adhesion inside each material stack under test .....	58
3.3. Elemental analysis of the LCP and silicone (PDMS) surfaces after T-Peel test using EDX.....	59
4.1 Comparative table of impedance magnitude at 1kHz $ z $ , total and cathodic charge storage capacities (CSC), and charge injection capacity (CIC) values for the three categories of electrodes: 700 $\mu\text{m}$ "Base Au", 300 $\mu\text{m}$ "Base Au", and 700 $\mu\text{m}$ "Shark teeth Au" .....	81
A.1 Comparison table depicting the difference between the diameter set on the laser and the actual electrode opening diameter due to TPU melting and reflowing on the edges of the circumference during the laser ablation step .....	110
A.2 Implantation data for pure Platilon PU, Platilon PU with gold tracks and for medical grade Bionate 80A PU. Thickness values are given in median [1 <sup>st</sup> – 3 <sup>rd</sup> quartiles] .....	112
B.1. Results of the tensile stretching tests performed with different gold tracks widths and geometries embedded in TPU.....	115

# Summary

Currently, neurostimulation holds the capability of treating symptoms associated with epilepsy, essential tremor, depression, migraine, incontinence, Parkinson's, Tourette's, and other diseases and disorders. Given the constant evolution in the field of biomedical technology and the increasing demand for advanced solutions in neural interface technology, addressing challenges associated with conventional neural electronic implant packaging becomes crucial. Conventional packaging often results in bulkiness, limited proximity to the target tissue, and potential complications, prompting an emerging need to miniaturize and soften the packaging. While flexible substrates like polyimide, parylene C, polyurethane, and silicone elastomers have been explored by the neural implants industry, the ongoing shift towards fully implantable, biocompatible, and flexible active implants calls for a more tailored packaging approach.

This Ph.D. research aims to provide a comprehensive investigation and overview of utilizing polymers as substrate and encapsulation materials for neural implants, examining both the advantages and challenges associated with their use. In particular, the study will look into the latent potential offered by thermoplastic polymers, with a specific focus on thermoplastic polyurethane (TPU) and liquid crystal polymer (LCP), as these polymers offer a unique blend of properties that make them promising candidates to significantly impact neural interface technology.

In Chapter 2, a thorough literature review investigates polymers commonly used in neural implants. This chapter not only explains the reactions happening when implants are put into the body but also emphasizes the basic requirements for implantation. The chapter focuses on the main properties and advantages of various polymers, distinguishing between thermoset and thermoplastic polymers. Some examples of using these polymers as substrate and coating materials for passive neural interfaces, together with the insights into the associated processing steps, are presented in this chapter. Furthermore, the chapter looks into the ways of integrating electronic chips into passive implants, presenting a detailed review of bonding techniques, bumping technologies, and adhesive types, as well as showing examples of existing active neural implants.

Chapter 3 continues the exploration by focusing on thin film encapsulation materials on flexible LCP substrates. Using HfO<sub>2</sub>-based atomic-layer-deposition multilayers, a hybrid ParC-ALD multilayer, and an LCP coating layer, this chapter systematically evaluates how well these coatings work through various testing methods. T-peel, water-vapor-transmission-rate (WVTR), and long-term electrochemical-impedance-spectrometry tests give valuable insights into the effectiveness of these coatings, emphasizing the advantage that can be offered by thermoplastic LCP-LCP coating-substrate interfaces.

Chapter 4 presents the fabrication method for a thermoplastic polyurethane-based electrode array with high-resolution gold interconnects employing the following techniques: thermocompression bonding, electroplating, laser direct imaging-based lithography, and laser ablation. The integrity of this electrode array is evaluated under conditions simulating the human body environment, involving soak tests at different temperatures and in-vivo tests. The extended evaluation includes electrochemical and optical transparency tests to further enhance our understanding of how well the electrode array performs in different situations.

Chapter 5 shows the integration of ASICs into the previously described polyurethane-based electrode array. Using flip-chip bonding technology, this integration involves connecting ultra-thin chips to gold metallization tracks using an anisotropic conductive adhesive. The successful combination of these components represents a significant step toward creating polymer-based active neural interfaces.

The concluding Chapter 6 summarizes the key findings and contributions of the thesis. It not only highlights the scientific progress made in using thermoplastic polymers for neural interfaces but also emphasizes the successful integration of ASICs into a polyurethane-based electrode array. The chapter ends with suggestions for future research directions and improvements.

In essence, this thesis provides an exploration of polymer-based flexible neural interfaces, particularly focusing on the unique properties of LCP and TPU thermoplastics. This work introduces polyurethane as a novel addition to the portfolio of biocompatible polymers used as both substrate and coating material for neural interfaces. The combination of biocompatibility, flexibility, microfabrication compatibility, and optical transparency, together

with the developed fabrication process technology for high-density and high-resolution soft neural implants, contributes to and expands the toolkit available for developing fully implantable soft neural active implants.

# Samenvatting

Momenteel kan neurostimulatie al symptomen behandelen die geassocieerd worden met epilepsie, essentiële tremor, depressie, migraine, incontinentie, Parkinson, Gilles de la Tourette en andere ziekten en aandoeningen. Gezien de constante evolutie op het gebied van biomedische technologie en de toenemende vraag naar geavanceerde oplossingen in neurale interfacetechnologie, is het van cruciaal belang om de uitdagingen aan te pakken die gepaard gaan met de conventionele behuizing van neurale elektronische implantaten. Conventionele behuizingen resulteren vaak in forse afmetingen, een beperkte nabijheid tot het doelweefsel en potentiële complicaties, waardoor de behoefte ontstaat om de behuizing te verkleinen en zachter te maken. De industrie voor neurale implantaten heeft flexibele substraten zoals polyimide, parylene C, polyurethaan en siliconenelastomeren onderzocht, maar de voortdurende verschuiving naar volledig implanteerbare, biocompatibele en flexibele actieve implantaten vraagt om een meer op maat gemaakte behuizingsaanpak.

Dit promotie-onderzoek wil een uitgebreid onderzoek en overzicht bieden van het gebruik van polymeren als substraat en inkapselingsmateriaal voor neurale implantaten, waarbij zowel de voordelen als de uitdagingen van het gebruik ervan worden onderzocht. In het bijzonder zal het onderzoek zich richten op het latente potentieel van thermoplastische polymeren, met een specifieke focus op thermoplastisch polyurethaan (TPU) en vloeibaar kristalpolymeer (LCP), aangezien deze polymeren een unieke mix van eigenschappen bieden die hen veelbelovende kandidaten maken om de neurale interfacetechnologie aanzienlijk te beïnvloeden.

In hoofdstuk 2 wordt een grondig literatuuronderzoek gedaan naar polymeren die vaak worden gebruikt in neurale implantaten. Dit hoofdstuk legt niet alleen de reacties uit die optreden wanneer implantaten in het lichaam worden geplaatst, maar benadrukt ook de basisvereisten voor implantatie. Het hoofdstuk richt zich op de belangrijkste eigenschappen en voordelen van verschillende polymeren, waarbij onderscheid wordt gemaakt tussen thermohardende en thermoplastische polymeren. Enkele voorbeelden van het gebruik van deze polymeren als substraat- en coatingmateriaal voor passieve neurale interfaces, samen met de inzichten in de bijbehorende verwerkingsstappen, worden in dit hoofdstuk gepresenteerd.

Verder gaat het hoofdstuk in op de manieren om elektronische chips te integreren in passieve implantaten, waarbij een gedetailleerd overzicht wordt gegeven van afmonteertechnieken en soorten verbindingsmaterialen, en voorbeelden worden getoond van bestaande actieve neurale implantaten. Hoofdstuk 3 zet de verkenning voort door zich te richten op dunne film inkapselingsmaterialen op flexibele LCP substraten. Met behulp van HfO<sub>2</sub>-gebaseerde, middels atomaire laag-afzetting (ALD) vervaardigde, multilagen, namelijk een hybride ParC-ALD multilaag en een LCP coatinglaag, evalueert dit hoofdstuk systematisch hoe goed deze coatings werken door middel van verschillende testmethoden. T-afpel, waterdamp-transmissie-snelheid (WVTR) en lange-termijn elektrochemische impedantie-spectrometrietesten geven waardevolle inzichten in de effectiviteit van deze coatings en benadrukken het voordeel dat thermoplastische LCP-LCP coating-substraat interfaces kunnen bieden.

Hoofdstuk 4 presenteert de fabricagemethode voor een op thermoplastisch polyurethaan gebaseerde elektrode-array met gouden interconnecties met hoge resolutie, waarbij de volgende technieken worden gebruikt: thermocompressiehechting, galvaniseren, lithografie op basis van directe laserbeeldvorming en laserablatie. De integriteit van deze elektrode-array wordt geëvalueerd onder omstandigheden die de omgeving van het menselijk lichaam simuleren, met inweekttests bij verschillende temperaturen en in-vivotests. De uitgebreide evaluatie omvat elektrochemische tests en optische transparantietests om nog beter te begrijpen hoe goed de elektrode-array presteert in verschillende situaties.

Hoofdstuk 5 toont de integratie van ASIC's in de eerder beschreven op polyurethaan gebaseerde elektrode-array. Met behulp van flip-chip hechttechnologie worden ultradunne chips verbonden met gouden metallisatiesporen met behulp van een anisotrope geleidende lijm. De succesvolle combinatie van deze componenten betekent een belangrijke stap in de richting van het creëren van op polymeren gebaseerde actieve neurale interfaces.

Het afsluitende hoofdstuk 6 vat de belangrijkste bevindingen en bijdragen van het proefschrift samen. Het belicht niet alleen de wetenschappelijke vooruitgang die is geboekt in het gebruik van thermoplastische polymeren voor neurale interfaces, maar benadrukt ook de succesvolle integratie van ASIC's in een op polyurethaan gebaseerde elektrode-array. Het hoofdstuk

eindigt met suggesties voor toekomstige onderzoeksrichtingen en verbeteringen.

In essentie biedt dit proefschrift een verkenning van op polymeren gebaseerde flexibele neurale interfaces, waarbij de nadruk ligt op de unieke eigenschappen van LCP en TPU thermoplasten. Dit werk introduceert polyurethaan als een nieuwe toevoeging aan de portfolio van biocompatibele polymeren die worden gebruikt als substraat en coatingmateriaal voor neurale interfaces. De combinatie van biocompatibiliteit, flexibiliteit, compatibiliteit met microfabricage en optische transparantie, samen met de ontwikkelde fabricagetechnologie voor zachte neurale implantaten met hoge dichtheid en hoge resolutie, draagt bij aan en breidt de gereedschapskist uit die beschikbaar is voor de ontwikkeling van volledig implanteerbare zachte neurale actieve implantaten.

# Acknowledgments

Completing this Ph.D. has been an enriching journey, and I couldn't have done it without the support and guidance from many people. I want to express my heartfelt thanks to those who played a crucial role in this achievement.

First and foremost, I would like to express my gratitude to my supervisors, Vasiliki Giagka and Wouter Serdijn, for the invaluable chance to start my Ph.D. at Delft University of Technology. Vasso, your support throughout the whole journey has extended beyond science and you exemplified as a role model for me during these years. Wouter, your open-hearted mentorship has been a guiding force for me. I hope the profound quote, "Children are born with wings, teachers help them to fly" still graces your office door, as it perfectly describes the essence of the academic journey under your guidance.

Being part of the Bioelectronics group and spending my initial months in the inspiring TU Delft environment was a privilege. I extend my thanks to the colleagues I met there for their warm welcome. My time in the Netherlands remains a cherished memory.

Embarking on Fraunhofer IZM Berlin brought a new chapter, new faces, and enhanced support. I am deeply thankful to colleagues: Manuel Seckel, Ralf Schmidt and Christine Kallmayer for introducing me to the topic of my future PhD, sharing their extensive knowledge on the topic and their solid support during my journey. My special appreciation goes to the whole Galvanic team, who were so helpful at times. I extend my sincere thanks to my fellow PhD peers from the Fraunhofer IZM institute for their invaluable contributions and collaborative spirit during our PhD meetings. Also, I would like to thank my teammates for our discussions, for their support with different experiments and our meetings outside work. Further thanks to Joao Marques for his kindness and expertise and to Astrid Gerholdt for the SEM and AFM analysis.

Joining the POSITION II project under the dedicated guidance of Vasso was a truly transformative experience for me and deserves special recognition. The knowledge and network opportunities gained during this period were not only valuable for my research but also played a significant role in shaping my professional journey after academia.



I would also like to thank my PhD thesis committee for accepting the invitation, for the time and effort in reading my Ph.D. thesis and for the valuable feedback.

My deepest appreciation goes to my parents for their unwavering support and faith, the cornerstone of my life achievements. Simultaneously, my best friend and a special group of friends from my Master's program acted as pillars of strength and joy throughout my Ph.D. journey. Finally, heartfelt thanks to my husband for being editor, coach, and cheerleader to me, giving support and motivation during the demanding process of thesis writing.

To all those mentioned above and countless others who have contributed in various ways to my Ph.D. project, I express my sincerest thanks. Your support has left an unforgettable imprint on this journey, and I am grateful for the shared experiences and fellowship that have enriched this chapter of my life.

# List of Publications

## Journal Publications

1. In preparation:  
**Anna Pak**, Joshua Wilson, Manuel Seckel, Pablo De Anta Dardagan, Ralf Schmidt, Domonkos Horvath, Kinga Toth, Raphael Pankus, Astrid Gollhardt, Michael Gerberich, Andreas Grünschneder, Tim Hosman, Nasim Bakhshae Babaroud, Punal Surani, Michael Zwanzig, Istvan Ulbert, Vasiliki Giagka, Thermoplastic polyurethane as a base material for soft neural interfaces, 2024
2. **A. Pak**, K. Nanbakhsh, O. Hölck, R. Ritasalo, M. Sousa, M. van Gompel, B. Pahl, J. Wilson, C. Kallmayer, V. Giagka, Thin Film Encapsulation for LCP-Based Flexible Bioelectronic Implants: Comparison of Different Coating Materials Using Test Methodologies for Life-Time Estimation, *Micromachines*, Volume 13, Issue 4, pp. 544, March 2022.
3. M. Athanasiadis, **A. Pak**, D. Afanassenkau, I. R. Minev, Direct writing of elastic fibers with optical, electrical, and microfluidic functionality, *Advanced Material Technologies*, March 2019.

## Conference Publications

1. Andrada Velea, Joshua Wilson, **Anna Pak**, Manuel Seckel, Sven Schmidt, Stefan Kosmider, Nasim Bakhshae, Wouter Serdijn, Vasiliki Giagka, UV and IR laser-patterning for high-density thin-film neural interfaces, *IEEE European Microelectronics and Packaging Conference (EMPC) 2021*, September 2021.
2. A.I. Velea, S. Vollebregt, T. Hosman, **A. Pak**, V. Giagka, Towards a Microfabricated Flexible Graphene-Based Active Implant for Tissue Monitoring During Optogenetic Spinal Cord Stimulation, *Proceedings IEEE Nanotechnology Materials and Devices Conference (NMDC) 2019*, October 2019.

## Posters and Presentations

1. A. Pak, W.A. Serdijn, V. Giagka, Embedding small and thin electronics into flexible implants, *Book of Abstracts, SAFE 2019*, July 2019.
2. Anna Pak, Wouter A. Serdijn, Vasiliki Giagka, Embedding Small Electronic Components into Tiny Flexible Implants, *Book of Abstracts, 2019 International Winterschool on Bioelectronics Conference (BioEl 2019)*, March 2019.
3. Anna Pak, Wouter A. Serdijn, Vasiliki Giagka, EMBEDDING SMALL ELECTRONIC COMPONENTS INTO TINY FLEXIBLE IMPLANTS, *Book of Abstracts, 7th Dutch Biomedical Engineering Conf. (BME) 2019*, January 2019.

# Biography

Anna Pak was born in Karaganda, Kazakhstan, in 1994. She received a B.Sc. degree in Nanotechnology from Novosibirsk State Technical University, Russia, in 2015. Subsequently, she was awarded the DAAD STIBET III scholarship for the international Master Program in Nanobiophysics, where she obtained an M.Sc degree from Technische Universität Dresden, Germany, in 2017. Anna is one of the inventors of the patent “Method for producing an elastic and flexible fiber with optical, electrical or microfluidic functionality” (US Patent No. 17433046 – May 19, 2022, EU Patent No. 2020706746 – Jan 5, 2022.).

In July 2018, she started as a Ph.D. candidate at Delft University of Technology. Her research was conducted as part of the EU ECSEL JU project POSITION II European project on Smart Catheters and Implants. Her research interests include soft bioelectronics, with the main focus on packaging reliability, material and technology development for integration in neuroprosthetics.

Since August 2023, Anna has been a Jr. Project Leader at Osypka AG, contributing to projects involving active implantable medical devices.

Anna appreciates new connections, do not hesitate to reach her via [annapakphd@gmail.com](mailto:annapakphd@gmail.com) if you have any questions, ideas, or recommendations.